



YEARS OF
AGH UST

KNOWLEDGE TECHNOLOGY AND SOCIETY

Scientific Editor
Katarzyna Styszko

AGH ISC 2018



AGH ISC



WYDAWNICTWA AGH

KRAKOW 2019



THE FACULTY OF
ELECTRICAL
AND COMPUTER ENGINEERING
RZESZÓW UNIVERSITY OF TECHNOLOGY



KNOWLEDGE TECHNOLOGY AND SOCIETY

Scientific Editor
Katarzyna Styszko

AGH ISC 2018



WYDAWNICTWA AGH

KRAKÓW 2019

Published by AGH University of Science and Technology Press

© Wydawnictwa AGH, Krakow 2019
ISBN 978-83-66364-10-3

Editor-in-Chief: *Jan Sas*

Editorial Committee:

Andrzej Pach (Charmain)

Jan Chłopek

Barbara Gąciarz

Bogdan Sapiński

Stanisław Stryczek

Tadeusz Telejko

Scientific Editor: *Katarzyna Styszko*

Editorial support:

Justyna Durak

Alicja Skiba

Przemysław Furman

Katarzyna Szramowiat-Sala

Krzysztof Sornek

Reviewers:

*Anita Lewandowska, Bogusław Podhalański, Andrei Ausiyevich, Marek Vagaš,
Dariusz Wideł, Robert Mazur, Tomas Salkus, Nikolay Makisha, Tomasz Mirowski*

Technical editor: *Agnieszka Rusinek*

Desktop publishing: *Munda*

AGH University of Science and Technology Press (Wydawnictwa AGH)

al. A. Mickiewicza 30, 30-059 Kraków

tel. 12 617 32 28, 12 636 40 38

e-mail: redakcja@wydawnictwoagh.pl

<http://www.wydawnictwa.agh.edu.pl>

CONTENTS

INTRODUCTION	5
Artur Wyrwa, Patrycja Ostasz, Beata Sularz MODELLING THE DEVELOPMENT OF ELECTRIC VEHICLES IN POLAND.	7
Halyna Petryshyn, Halyna Lukashchuk, Adriana Kryvoruchko, Vladyslav Kryvoruchko PROPOSAL OF THE REVITALIZATION OF THE LANDSCAPE AROUND THE POTOCKI FAMILY PALACE IN LVIV	17
Justyna Durak, Anna Miernik, Agnieszka Jaworska, Alicja Skiba, Przemysław Furman, Katarzyna Styszko REMOVAL OF PHARMACEUTICALS RESIDUES AND PERSONAL CARE PRODUCTS BY ADVANCED OXIDATION TECHNIQUES	33
Alicja Skiba, Przemysław Furman, Justyna Durak, Natasza Dobrowolska, Natalia Guzik, Damian Zięba, Magdalena Kistler, Anne Kasper-Giebl, Katarzyna Styszko CHEMICAL COMPOSITION OF ATMOSPHERIC AEROSOLS COLLECTED IN KRAKOW AGGLOMERATION	43
Justyna Sokołowska, Jarosław Zubrzycki, Magdalena Marchewka THE NUMERICAL METHODS FOR IDENTIFICATION AND ANALYSIS OF ELECTROENCEPHALOGRAPHIC SIGNALS	53
Magdalena Kopernik, Paweł Tokarczyk DEVELOPMENT OF MESOSCALE MODEL OF BLOOD THROMBOSIS	65
Henryk Wachta, Michał Wroński, Katarzyna Józwiak, Gracjan Kudra FLOODLIGHT SIMULATION OF REAL ARCHITECTONIC OBJECT USING 3D MODEL.	77
Łukasz Magda, Katarzyna Wilkosz, Władysław W. Kubiak APPLICATION OF GLASSY CARBON ELECTRODE MODIFIED BY PEDOT-TiO ₂ COMPOSITE IN METOL DETECTION	93

INTRODUCTION

The rapid technological changes, characterizing the nowadays society require a shift towards development of new ways to protect environment and to improve the industry sector.

The monograph “Knowledge, Technology and Society” is the result of the first edition of AGH International Student Conference: Knowledge, Technology and Society (AGH ISC). It consists of works based on scientific activity of students and young scientist, as well as scholars from different research areas.

The conference took place on 10–12 October, 2018 in Kraków, at the AGH University of Science and Technology.

AGH ISC Conference is conceived as a forum for the presentation of scientific activities of students. It is a place to share the effects of their scientific work, to explore new possibilities between research fields, to create new friendships and to account the very first successes in their future career.

Prof. Anna Siwik

Chairman of the Organizing Committee

The Organizing Committee:

Ph.D. Leszek Kurecz

Ph.D. Paweł Bogacz

Prof. Katarzyna Styszko

Ph.D. Katarzyna Szramowiat-Sala

Ph.D. Paweł Drożdż

M.Sc. Krzysztof Sornek

M.Sc. Marta Marczak

Artur Wyrwa*, Patrycja Ostasz*, Beata Sularz*

MODELLING THE DEVELOPMENT OF ELECTRIC VEHICLES IN POLAND

Abstract

The subject of this study was to analyze the development of the road transport sector in Poland with emphasis on the role of battery electric vehicles. The main analytical tool used in the study was the TIMES-PL model. Two scenarios were analyzed i.e. a “Baseline” scenario that assumed that the future vehicle fleet would maintain the similar structure as today and the EV scenario which assumed full implementation of the Polish e-mobility plan. If the charging process is left uncontrolled and if it takes place in the evening peaks instead of off-peak periods during nights this may increase the risk of power shortage. In some moments the electrical load may be increased due to EVs charging by ca. 2 GW. The results show that with assumed technological progress electric vehicles in the mid-term will win the competition with fossil fuel-based cars, in particular to cover short distances inside cities.

Keywords

transport, electric vehicles, modelling, energy system

1. INTRODUCTION

The transition of energy system towards more sustainable one requires, among others, substitution of fossil fuels with renewable energy sources. From the energy end-use sectors point of view large amount of fossil fuels, notably gasoline, diesel and LPG are used for transportation. The aim of the paper was to analyze selected implications of the development of electric vehicles in Poland. The study was limited to cars so buses and trucks were out of the study scope. The main motivation for conducting the study was the announcement by the Polish Prime Minister in 2016 of the ambitious Electro-mobility Development Plan with the main objective of reaching 1 million electric vehicles in Poland in 2025. The main analytical tool used in the study was the TIMES-PL model [1, 2]. This model belongs to the family of national models build with the use of the TIMES generator. The model minimizes the total

* AGH University of Science and Technology, Faculty of Energy and Fuels, Krakow, Poland;
corresponding author: awyrwa@agh.edu.pl

costs of delivery of energy services – what for our study means transportation of passengers for demanded distances. Two main scenarios were elaborated. The first one assumed, that in general, the future vehicle fleet will maintain the similar structure as today. The second one assumed full implementation of the Polish e-mobility plan. The impact of development of EVs in Poland on change of the electric load profile due to battery charging as well as on pollutants emissions was analyzed.

2. DESCRIPTION OF THE METHODOLOGY

2.1. TRANSPORT SECTOR INSIDE TIMES-PL

In this study we made use of the existing transport module, which is available in the TIMES-PL energy-economic model. This module considers transportation of goods and passengers by road, rail, air and sea. Our goal was to propose a new approach for modelling the battery electric vehicles (BEV) inside TIMES-PL. TIMES-PL uses a bottom-up approach and therefore cars were represented in the most possible disaggregated way (according to the availability of the statistical data) i.e. by fuel and technology type. In methodological context, TIMES-family models solve the constraint optimization problems, typically of Linear Programming or Mixed Integer type. In our case, goal function represented the total system costs of delivering transportation services [3]. A part of the TIMES-PL model topology representing the transport sector is depicted in Figure 1.

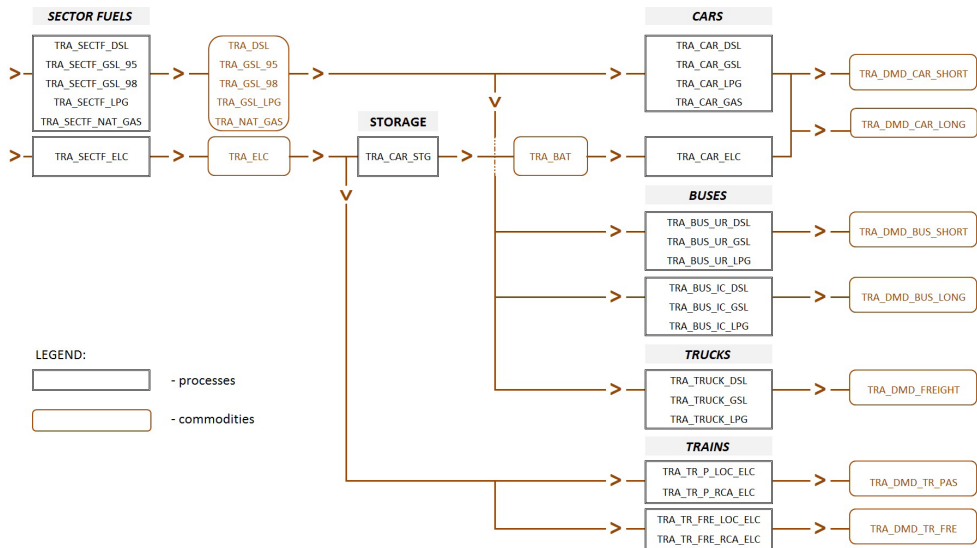


Fig. 1. Part of the TIMES-PL model topology representing the transport sector

As one can see this module is interrelated with other TIMES-PL modules, mainly via secondary fuels (i.e. output from refineries) and electricity (i.e. output from power plants and CHPs).

Once they enter into the transport module, these commodities are labelled with the “TRA_ prefix” to facilitate monitoring of their flow and imposition of constraints. Commodities are subsequently processed by different technologies to deliver, at the end, the demanded transportation services for passengers and freight. In case of BEV, electricity first goes to the vehicle’s battery, and then it is passed on to the vehicle while driving. As one can see two categories of transportation demand are defined for cars i.e. short and long distances. The presented system approach makes it possible to consider feedbacks among individual TIMES-PL modules e.g. the increase in the number of EVs will have an impact on power generation units as well as on refineries and crude oil imports.

2.2. REPRESENTATION OF THE ELECTRIC VEHICLES IN THE MODEL

An electric car was modelled as two technologies i.e. a battery and a vehicle– linked together to form a Battery Electric Vehicle (BEV). Thanks to this, it was possible to control the battery charging and operation. At the same time electric vehicle was characterized with the use of a standard set of TIMES parameters similar to these used for characterize other vehicle types. An electric car, like all vehicles in the transport model, belongs to the set of demand (DMD) processes. This process represents the end-use technology which output is used to cover final demand for transport services. Cars in TIMES-PL were defined at the DAYNITE time slice level – what means that they operate at the most disaggregated temporal resolution. The capacity unit describing the technology is simply a number of cars, and the unit of output represented by the F_{out} variable is the number of passenger kilometers (Pkm) calculated according to the following equation:

$$F_{out}(EV) = CAP(EV) \cdot CAP2ACT(EV) \cdot AF(EV) \cdot ACTFLO(EV) \quad (1)$$

where:

- CAP – the number of cars,
- $CAP2ACT$ – capacity to activity conversion factor,
- AF – maximum distance a car can travel annually,
- $ACTFLO$ – the average number of passengers transported by a car.

The energy input stream (F_{in}) to the EV process is related to the output stream by the formula:

$$F_{in}(EV) = \frac{F_{out}(EV)}{EFF(EV) \cdot ACTFLO(EV)} \quad (2)$$

where EFF is the number of kilometers driven by EV using a unit of energy (e.g. gigajoule [GJ]).

Energy input stream to electric vehicle $F_{in}(EV)$ becomes equal to the energy output stream from the battery $F_{out}(BAT)$. The battery that accumulates energy for electric vehicle has been

defined in the model as an energy storage process (STG – general storage process). The basic unit describing the battery capacity (or rather specific power in this case) is kilowatt (kW) and the unit of the output stream is gigajoule (GJ).

The most important parameter describing the battery operation is the energy storage efficiency $EFF(BAT)$ in the loading and unloading operation. The energy stream that flows out from the battery is determined by the electric car usage. It was assumed that each BEV is equipped with the battery with the average electric specific power of ca. 21 kW, which can be fully charged within one time slice (3 hours). The assumed energy consumption of BEV equaled to 10 kWh per 100 km resulting in the maximum distance that can be travelled of ca. 250 km.

2.3. FUTURE PRICES OF EVS

The TIMES-PL model enables constrained optimization within specified transport segments based on minimization of costs of transporting services. The existing cars fleet can be only gradually replaced by new technologies such as electric cars (constraints were imposed on the technology replacement rates). Therefore, the price of electric cars is one of the most important decisive factors in determining their the future market share. In this study we made use of the battery electric vehicle forecast presented in [4]. Unfortunately, this forecast is available only for the time period until 2025, whereas our modelling time horizon covers the years up to 2030. Therefore, we made own estimates as regards to the BEV prices for the lacking years. The costs of a technology or a product are not constant over time. For a majority of goods it was empirically proven that as the number of manufactured goods are increasing, the cost is decreasing [5]. This phenomenon is called technology-learning and includes mechanisms such as: R&D, learning-by-doing, effects of upscaling. In case of BEVs the technology-learning process will particularly influence the battery cost improvements.

If X_0 denotes a cumulative number of units produced for the price C_0 , then the progress ratio parameter pr can be defined as a ratio of final to initial costs associated with a doubling of cumulative output:

$$pr = \frac{C_f}{C_0} = \left(\frac{2X_0}{X_0} \right)^b = 2^b \quad (3)$$

where:

- C_f – unit investment costs of the technology after doubling its production,
- b – elasticity of the progress ratio representing the speed of learning.

The value of investment costs is often replaced by the price of a technology or product.

The Equation (3) can be referred to any time interval. Unit investment cost for a given technology in time t after a cumulative number of units have been produced can be calculated from Equation (4).

$$C_t(x_t) = C_0 \left(\frac{X_t}{X_0} \right)^b \quad (4)$$

where:

- C_t – unit investment costs of the technology subjected to process improvement in time t ,
- C_0 – the initial unit investment costs of the technology,
- X_t – cumulative number of units produced till time t ,
- b – elasticity of the progress ratio representing the speed of learning.

Finally, it is worth to introduce the learning rate lr , which represents the proportional cost savings made for a doubling of cumulative output can be linked with pr through the following equation:

$$lr = 1 - pr \quad (5)$$

At a learning rate lr of 15% (pr of 85%), the cost of a technology decreases by 15% for every doubling of its cumulative production.

In order to determine the future price of electric cars in Poland, it was necessary to take into account their global development contributing to the learning process. Therefore, the first step was to determine the learning rate (and progress ratio) based on global historical data and available forecasts. The progress ratio was calculated based on: (i) the data presented in [4] providing information on the battery electric cars prices in 2017 and 2025 (i.e. 37 kUSD and 27.2 kUSD, respectively) and (ii) the evolution in number of BEVs in that period (i.e. 2.4 million in 2017 and 15 million in 2025 [6] – assuming 60% share of BEV in the overall electric car market). Applying these data in Equations (3)–(5) gave the results presented in Table 1.

Table 1. Values of progress ratio, progress ratio elasticity and learning rate for BEVs estimated in this study

Elasticity of the progress ratio b [–]	Progress ratio pr [–]	Learning rate lr [%]
0.17	0.89	11

Subsequently, based on the forecasted number of BEV in 2030 [6] (i.e. ca. 33 million BEVs) it was calculated using Equation (5) that the price of the BEVs will drop from 37 kUSD reported in 2017 to 23.8 kUSD in 2030.

3. DESCRIPTION OF SCENARIOS

In the “Baseline” scenario the development of the transport sector and individual technologies followed the historical trends. New technologies such as EVs could obviously been introduced, however, there was no support system to promote them. The demand forecast

was based on [7] – the demand for transport of goods and passengers continued to grow till 2030. The Baseline scenario assumed that the relative shares of fuels consumed in future would be in line with [8].

In the second scenario called EV the demand for transport services was kept at the same level as before. Additionally, this scenario assumed that the number of electric vehicles in Poland would reach 1 million in 2025 as announced in the Electro-mobility Development Plan. The EVs development pathway from the base year till 2025 is based on [9]. Since in our study the analysis of the development of the transport sector is conducted till 2030 we have extrapolated the EVs development trend till then, what results in more than 2 million electric cars in 2030.

4. RESULTS AND DISCUSSION

According to the Baseline scenario the largest increase in the coming years is observed in the number of gasoline cars, while the number of LPGs fueled cars remains at a similar level as today. Gasoline cars especially cover the growing demand for short distance transportation in urban areas. In the EV scenario (Fig. 2), the situation is much different.

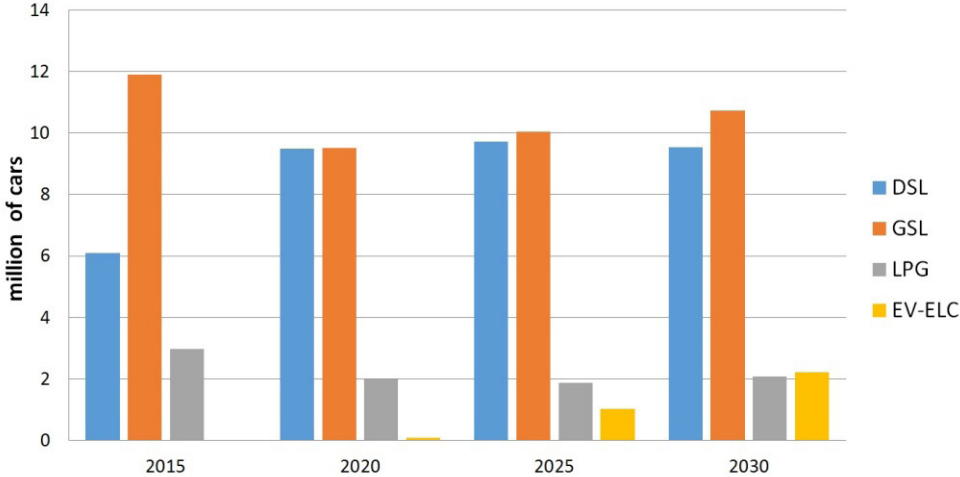


Fig. 2. Number of cars according to the fuel type in the EV scenario

Besides rapid grow in the number of EVs as required to meet the e-mobility target there are also more diesel-fueled vehicles. Diesel cars are chosen by the model due to the cheaper costs of using this type of vehicle especially for long distances. This also reduces the total number of passenger cars in 2030, because electric cars and diesel cars have a high average annual mileage. Batteries are discharged every day on the almost constant level, slight differences exist only between the seasons. This is because the same daily usage profile was assumed for EVs. EVs deliver transportation services during the day and are left for charging during the

night. Battery charging is, however, carried out at different times and at different levels due to electricity price signals. The influence of battery charging on the system load for working and non-working days is presented in Figures 3 and 4.

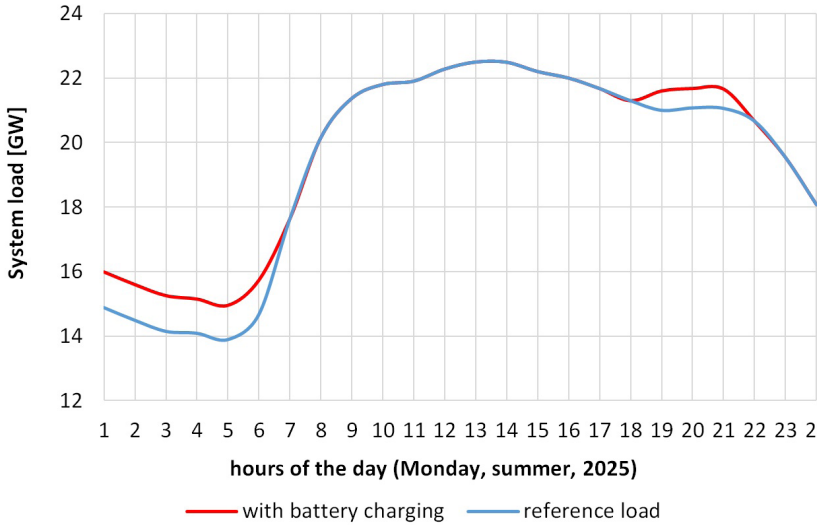


Fig. 3. The change of system load due to EV charging

Figures 3 and 4 show the influence of intelligent charging on the hourly load profile estimated for Monday and Sunday in summer 2025, respectively.

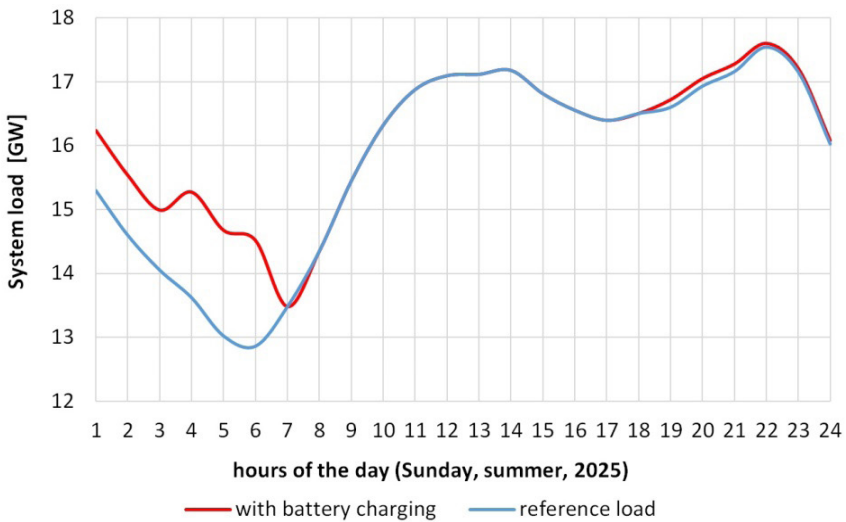


Fig. 4. The change of system load due to EV charging

As Sundays are assumed to be non-working days the morning and the evening peaks are postponed as compared to working days. In total ca. 220 GWh of electricity is supplied to EVs in 2020 while this number increases to ca. 3 TWh and ca. 6.5 TWh in 2025 and 2030, respectively. For comparison, [9] forecasts electricity consumption of EVs at the level of 2.3 TWh in 2025. Although the increase of annual electricity demand caused by EVs can be regarded as insignificant it can, however, have a significant impact on the system load. The latter may happen if charging process is left uncontrolled and instead of off-peak periods during nights it takes place in the evening peaks once adding additional ca. 2 GW to the system load may increase the risk of power shortage. On the other hand intelligent charging of cars during the nights' valleys will smooth the residual load and consequently improve the operation of the total power generators (see Figures 3 and 4). The electricity prices are determined by the model according to the varying overall load made-up by all end-use sectors and consequent dispatching of electricity generation units.

Pollutants emissions (including air pollutants and CO₂) from fuel combustion by vehicles were calculated on the basis of fuel consumption rates and emission factors [10]. They may vary according to the emission intensity of power generation (e.g. the electricity generation mix with higher share of renewables will have lower emission as compared to the fossil-fuel based one [2]). Analysis of possible power supply scenarios was, however, out of the scope of this study. According to [11], the total CO₂ emissions from cars in 2011 amounted to 23.5 million tons. As one can see in Figure 5, the results from the model are slightly underestimated. Nevertheless, in 2030 according to the Baseline scenario, CO₂ emissions will more than double as compared to 2011. EVs scenario reflects the alternative pathway as due to electrification of the transport sector CO₂ emissions are significantly reduced. In 2030 with the assumed grow in demand for transportation services the total CO₂ emissions are only slightly higher as compared to 2011).

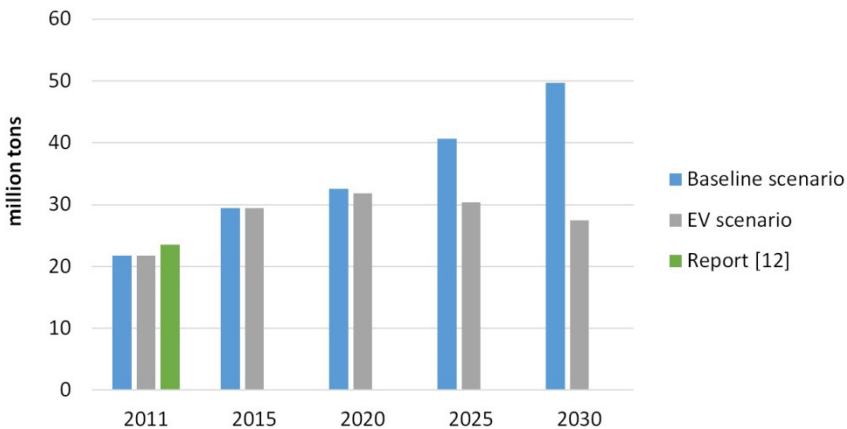


Fig. 5. CO₂ emissions from cars in different scenarios

One should bear in mind, however, that the overall reduction of CO₂ emissions can only be achieved if also the electricity generation mix will become less carbon intensive (if electricity used in EVs was generated only in coal-fired plants the overall CO₂ emissions would be higher compared to using LPG, DSL or GSL cars).

5. CONCLUSIONS

The TIMES-PL energy model was used to analyze the development of the transport sector in Poland until 2030. Two main scenarios were considered i.e. the “Baseline” scenario that assumed that the future vehicle fleet would maintain the similar structure as today and the EV scenario which assumed full implementation of the Polish e-mobility development plan aimed at achieving 1 million EVs in 2025. After analyzing the results, two key conclusions can be drawn. The additional amount of electricity that needs to be supplied to EVs is insignificant compared to the present electricity demand of the country. Even if the e-mobility development plan was fully achieved it would lead to ca. 4 TWh of electricity that need to be generated and supplied to EVs per year i.e. 3% of the current final electric demand. However, from the system hourly load point of view a large number of electric cars can have a strong effect either a negative or positive. The positive impact will be achieved when the charging processes will be controlled and will take place in time of power demand valleys e.g. during off-peak periods and especially at night. To achieve this delayed charging a special energy tariffs may be introduced for EVs to differentiate the electricity price accordingly. However, if EVs charging will be left uncontrolled and would take place in the evening peaks it may increase the risk of power shortage or need to invest in more peak power station development. The results show that, in the medium term, electric vehicles will win competition with fossil fuel cars, especially in the group of people using cars for short distances inside cities. Switch to EVs will eliminate direct emissions of air pollutants thus helping to reduce smog. The study confirms that the development of electric vehicles is necessary to decrease emissions of CO₂ from the transport sector. However, one cannot forget that the overall CO₂ emission will be achieved only when the electricity mix will include increasing number of less carbon-intensive power generation technologies.

ACKNOWLEDGEMENTS

This work received financial support from the statutory funding of AGH UST (no. 11.11.210.217).

REFERENCES

- [1] Wyrwa A., Szurlej A., Gawlik L., Suwala W. Energy scenarios for Poland – a comparison of PRIMES and TIMES-PL modeling results. *Journal of Power Technologies*, 2015, 95, pp. 100–106.
- [2] Wyrwa A. An optimization platform for Poland’s power sector considering air pollution and health effects. *Environmental Modelling & Software*, 2015, 74, pp. 227–237.
- [3] Loulou R., Remne U., Kanudia A., Lehtila A., Goldstein G. Documentation for the TIMES Model PART I [on-line]. 2005. Available from: <http://iea-etsap.org/docs/TIMESDoc-Intro.pdf> [accessed: 2018.03.01].
- [4] Slowik P., Lutsey N. Evolution of incentives to sustain the transition to a global electric vehicle fleet, White Paper. International Council on Clean Transportation, 2016.

- [5] Alberth S. Forecasting technology costs via experience curve – Myth or magic? *Technological Forecasting & Social Change*, 2008, 75, pp. 952–963.
- [6] International Energy Agency. *Global EV Outlook 2017* [on-line]. 2017. Available from: <https://www.iea.org/publications/freepublications/publication/GlobalEVOutlook2017.pdf> [accessed: 2017.10.15].
- [7] European Energy and Transport Trends 2050 [on-line]. 2013. Available from: <http://ec.europa.eu/transport/media/publications/doc/trends-to-2050-update-2013.pdf> [accessed: 2018.03.01].
- [8] Waśkiewicz J., Pawlak P. Prognozy eksperckie zmian aktywności sektora transportu drogowego (w kontekście ustawy o systemie zarządzania emisjami gazów cieplarnianych i innych substancji). Instytut Transportu Samochodowego, Zakład Badań Ekonomicznych. Warszawa 2017.
- [9] Ministerstwo Energii. *Krajowe ramy polityki rozwoju infrastruktury paliw alternatywnych*. Warszawa 2017.
- [10] The National Centre for Emissions Management. *Poland's Informative Inventory Report 2016*. Warsaw 2016.
- [11] Główny Urząd Statystyczny i Urząd Statystyczny w Szczecinie. *Transport drogowy w Polsce w latach 2010 i 2011*. Warszawa 2013.

**Halyna Petryshyn*, Halyna Lukashchuk*, Adriana Kryvoruchko*,
Vladyslav Kryvoruchko***

PROPOSAL OF THE REVITALIZATION OF THE LANDSCAPE AROUND THE POTOCKI FAMILY PALACE IN LVIV

Abstract

The Potocki Family's estate occupied a compact plot in Lviv near Breit/Szeroka Street (now Copernicus Str.), outside the city's fortifications, on the left bank of the Poltva Valley. The palace was rebuilt many times, its final variant appeared in 1889–1890 in the form of French classicism, designed by the architect Louis Dauvergne. Today, the palace is a state-owned monument of architecture. During its existence, it was remodelled and changed its purpose according to the needs of the times. Since 2000, the palace has belonged to the Lviv National Gallery of Art and is one of the largest art museums in Ukraine. The purpose of the project is to reconstruct the existing landscape around the palace (with the remains of the historic park) and adapt the site to the actual needs of the city. A system of lanes and a network of pedestrian paths was proposed, with the intent to activate the space around the palace and link it with tangent streets and public spaces. The revitalized landscape is considered a continuation of the artistic function of the palace.

Keywords

palace, historical landscape, revalorisation, art gallery, garden

1. RESEARCH

1.1. HISTORICAL EXCURSION

Outside of its fortified walls, Lviv was surrounded by manor houses, monastery gardens and, in the eighteenth century, yards of well-off burghers were located in its suburbs. From the nineteenth century, Lviv was rapidly developing and transforming into a large city, the presentable capital of an Austrian province – the Kingdom of Galicia and Lodomeria. In the former suburbs, large parks were established and the central part of the city was rearranged [1].

* Lviv Polytechnic National University, Department of City Planning, Lviv, Ukraine;
corresponding author: hala.petr@polynet.lviv.ua

There was also a substantial amount of greenery around manor-type residences and palaces, built according to the Baroque French principle of “entre cour et jardin” (between courtyard and a garden). The owners of the palaces often changed, the palaces moved from private property to that of the state and were subjected to lease and division. The Potocki family, having sold its estate, which included a palace and a park, at Halytska Square (now known as the Biesiadecki palace), acquired real estate near Breite/Szeroka Street (now Copernicus Str.) in 1822. On the plans of Lviv from the eighteenth to the first half of the nineteenth century one can see a planned regular garden and a few small buildings on this part of the plan (Fig. 1).



Fig. 1. The site of the future Potocki Family palace, located on historical map of Lviv (beneath) [2]

The first palace was built in the style of classicism according to a design by the Czech architect Ignác Chambrez. According to the design of 1822, it was a two-storey rectangular form, while in terms of massing, it was a residential building with a tall mansard roof. The facade was symmetrical with a central risalite, crowned with an attic and a balustrade. The first tier of the facade is rustic, the second tier of risalite is decorated with six pairs of Ionic pilasters (Fig. 2) [3]. The garden was later replanned into an English-style landscape garden as well (Fig. 3).

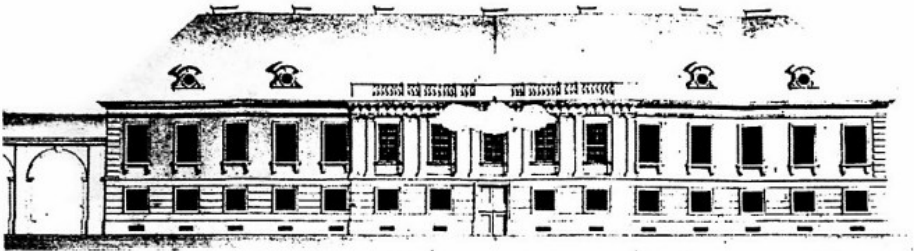


Fig. 2. Design of the Potocki Family Palace by architect Ignác Chambrez, 1822 [3]

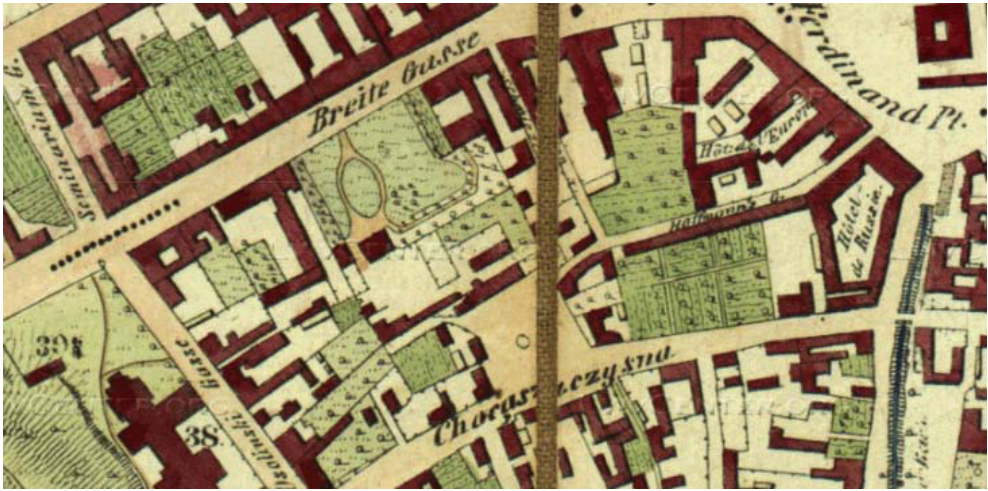


Fig. 3. Excerpts from historical maps of Lviv, which show the layout of the Potocki estate before its remodelling [4]

In the plans of the city of Lviv of 1844, 1863, 1873 and 1878, it is shown that in the interior of the estate there were two houses next to the front and side house, and the lush Kurderner had a circular parterre, traditional for the landscape style. The creator of the garden was probably the city gardener Carl Bauer. On the subsequent plans of Lviv from 1887 and 1892 only the side building was left, where the orthopaedic remedial institution of mgr Edward Madejski was placed, as the advertisement of 1876 testifies (Fig. 4). The classical palace was dismantled in 1860–1861 with the aim of reorganizing the entire complex into a more modern and presentable one.



Fig. 4. The appearance of the side building of the Potocki estate, 1876 [5]

On the map of 1892 a modern palace appeared, which was built in the style of French classicism in 1889–1890 according to the adapted design of the architect Louis Dauvergne (Fig. 5).

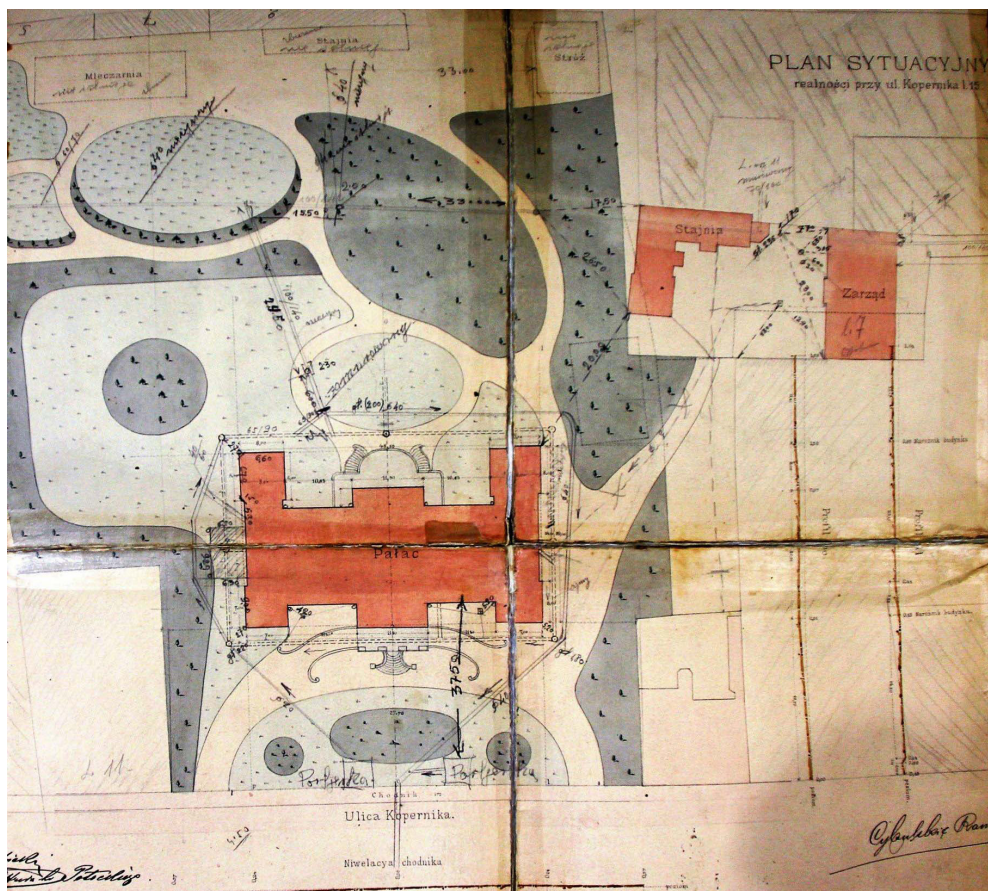


Fig. 5. Situational plan of landscape design on the site at Copernicus Street 15 in Lviv, 1880 [6]

The construction of the new residence was delayed for three decades. The construction was updated by the well-known philanthropist and passionate connoisseur of French architecture Alfred Potocki, who ordered the construction of a residence to Parisian architect Louis Dauvergne. The Earl Alfred II Józef Potocki (1817–1889) was a famous Polish and Austrian politician, the Head of the Galician Sejm, governor of the Kingdom of Galicia and Lodomeria (1875–1883).

His son Roman Potocki completed his palace building. The palace itself, built in 1880, is a monumental residence in the historicist style, representing the French Baroque classicism of the Louis XIV era [7]. Dauvergne’s design was modified by Lviv architects Julian Cybulski and Ludwik Baldwin-Ramult and implemented under their leadership [8]. In 1892 the design was exhibited at the construction exhibition in Lviv [9]. Behind the palace building, green plantations continued to have an irregular landscape character.

The construction boom in Lviv at the end of the nineteenth century provoked the ever-denser build-up of the former suburbs. Owners of the Potocki estate sold plots around the perimeter

for the commercial building. As a result, the palace remained open only from the main entrance i.e. from Copernicus Street. The area of the gardens was significantly reduced, the old plantations surrounding the estate's perimeter, inside the lawns were planted with vascular decorative plants.

1.2. TRANSFORMATION AFTER THE SECOND WORLD WAR

Today, the palace is a state-owned landmark of architecture. During its existence, it was remodelled and changed its purpose according to period-specific needs. Since 2000, the palace has belonged to the Lviv National Gallery of Art and is one of the largest art museums in Ukraine (Fig. 6). Next to it, on the palace's former utility zone, the Lviv Palace of Arts, designed by Vasyl Kamenshchik in 1987, was erected. The building is compositionally and stylistically subordinate to the Potocki Family Palace. It started to function in 1996 and since that time the number of artistic events and the flow of tourists is constantly increasing.



Fig. 6. The general view of the main facade of the Potocki Family Palace – today the Lviv Art Gallery [10]

In the photo of 1960–1964 one can see that the character of the landscape park is preserved in the yard (Fig. 7). In the 1980's, the territory of Potocki Family Palace was one of the still areas where construction work was carried out to tunnel the Lviv underground tram. As a result of deep drilling, changes in the structure of soils took place, the palace and the surrounding building began to settle and crack. The construction of tunnels was forcedly ceased, the idea of an underground tram was abandoned, and damaged structures required thorough reconstruction. Also, during the construction work, the surface of the garden and tall plantations, except for perimeter ones, were destroyed. During the reconstruction of the courtyard in the 1980s, the garden was recomposed by the director of the Lviv Art Gallery Boris Voznyckyj and the so-called French parterre was incorporated behind the palace which

should be stylistically close to the palace building (Fig. 8). The area at the front has been modernized with concrete slabs. Later, thuja and scarlet plants were planted, as well as flowerbeds with a different set of plants, which are poorly interconnected, especially with palace architecture. Recently, on the square in front of the palace, a rounded, symmetrically-shaped flowerbed has appeared, where junipers have been planted along with boxwood and freeform compositions of trees and bushes have also planted around.



Fig. 7. Rear facade of the Potocki Family Palace, 1960–1964 [11]



Fig. 8. General view of the gardens, 2018 [12]

1.3. CURRENT STATE

Today, the Potocki Family Palace belongs to the complex of the Lviv art gallery, which is formed by: directly by the Potocki Family Palace, restored back in 1974, the Art Gallery, auxiliary rooms, remnants of the parterre with existing green plantations, a mine for laying underground trams, an unsightly building for the maintenance of the construction of an underground

tram (where the Museum of ancient Ukrainian books is now located). At the initiative of Boris Voznyckyj in 2010, a park of castles and defensive structures of ancient Ukraine was established at the estate, where models of defensive structures in M 1:50 are displayed.

2. REVITALIZATION PROJECT

2.1. PRE-DESIGN STUDIES

Urbanization tendencies of Lviv in recent years, especially the controversial methods of sealing the territory, have a negative impact on the state of the complex of the Potocki Family Palace. Analysis of the current state of the site around the palace revealed two main problems. The first problem is of a natural and ecological character. It is that small, unconnected green areas – squares, manor houses, plantations along the streets – are subject to the greatest urban pressure. They rapidly degrade or physically cease to exist, as they are considered a potential reserve for development (Fig. 9).



Fig. 9. The current situation of the gardens of the Potocki Family Palace (photo by A. Kryvoruchko, 2017)

The second problem is the functioning of Lviv as the centre of a metropolitan area with a population of more than 1 million people. The city belongs to the five cities of Ukraine, which are dynamically developing. With the loss of an industrial character after the collapse of the USSR, Lviv develops as a tourist centre. Accordingly, it requires the development of services and culture. To this end, the functioning of every structure of the city that is important for increasing creativity is corrected, programmes of its development, reconstruction, revitalization, etc. are being effected [13, 14].

Pre-design studies of the complex of the Potocki Family Palace include:

- determining theoretical foundations, provisions and regulatory requirements necessary for the design of a given structure [15],
- generalization of Ukrainian and foreign practical experience in the design of similar objects,
- analysis of the current state (urban and natural conditions) of the project territory [16].

2.2. ESTIMATION OF THE PLANNING STRUCTURE

The layout of the territory of the palace, which was formed under the influence of several period and has suffered multiple instances of being damaged, has a rather chaotic structure. The landscaped park, which was originally established after an unsuccessful attempt to build an underground tram, was transformed into a modernist parterre, which is currently quite damaged and decayed. The system of connections between the territory and the city is poorly expressed as well. Today, the palace can only be reached from Copernicus Street, the entrance from Tykha Street is a utility entrance and is closed to pedestrians. It would be logical to restore the connection with the Yevhen Malanyuk Square, which is central to this city district, and which was built during the Baroque expansion stage of the city. The absence of an open entrance from Tykha Street does not allow the structure to be considered “a palace in the park”. The territory near the main facade of the palace is completely paved with concrete pavement, which is in good condition. Asphalt surfaces around the building of the Museum of the book and Tykha Street are partly in an unsatisfactory condition.

2.3. THE ANALYSIS OF THE DENDROFLORA AROUND THE POTOCKI FAMILY PALACE

The Research Programme was intended to investigate the contemporary species and age structure of the dendroflora. A survey of the territory of the Potocki Family Palace territory was carried out during on-site inspections, in accordance with the “Instruction” [17]. The nomenclature of taxa and their systematic position were adopted from Takhtadjan, 1987 [18].

The taxonomic analysis allowed us to establish that the contemporary dendroflora on the territory of the Potocki Family Palace was represented by 27 species and forms belonging to 20 families [19] (Tab. 1, Fig. 10). The number of species in families varied from one to two. The predominant species of woody plants were the very old *Fraxinus exelsior* L., *Quercus robur* L., *Acer platanoides* L., *Tilia platyphyllos* Scop.

Table 1. Distribution of trees and shrubs at the Pototcki Family Palace according to families

№ on the scheme	Species name (Lat.)	Natural habitat	Total number of plants
<i>Pinophyta</i>			
<i>Pinaceae</i> Lindl.			
13	<i>Piceapungens</i> Engelm	Northern America	1
<i>Cupressaceae</i> F. W. Neger.			
6	<i>Thuja occidentalis</i> ‘Columna’	–	37
5	<i>Thuja occidentalis</i> ‘Globosa’	–	4
10	<i>Juniperus sabina</i> L.	Europe, Crimea, Caucasus, Southern Siberia, Mongolia	15

Table 1 cont.

<i>Taxodiaceae</i> F. W. Neger			
27	<i>Metasequoia glyptostroboides</i> Hu et Cheng	China	1
Total gymnosperms			58
<i>Magnoliophyta</i>			
<i>Berberidaceae</i> TORR. et GRAY			
28	<i>Berberis thunbergii</i> DC	Japan, China	1
<i>Cercidiphyllaceae</i> VAN TIEGH.			
25	<i>Cercidiphyllum japonicum</i> Sieb. et Zucc.	East Asia, Japan	11
<i>Buxaceae</i> DUMORT			
8	<i>Buxus sempervirens</i> L.	Southern Europe, West Asia, Northern Africa	41
<i>Fagaceae</i> A. BR			
15	<i>Quercus robur</i> L.	Europe, Caucasus	6
3	<i>Quercus rubra</i> DU Roi	Northern America	8 (seedlings)
<i>Ulmaceae</i> MIRB.			
21	<i>Ulmus scabra</i> Mill.	Europe, Asia Minor, Caucasus	2
<i>Salicaceae</i> LINDL.			
14	<i>Salix alba</i> L.	Southern, Middle Europe, Siberia, Central Asia, Caucasus	3
<i>Tiliaceae</i> JUSS.			
4	<i>Tilia platyphyllos</i> Scop	Southern and Middle Europe, Caucasus	1
<i>Rosaceae</i> JUSS.			
17	<i>Prunus cerasifera</i> EHRH.	West Asia, the Balkans	5
24	<i>Malus domestica</i> Borkh	–	2
<i>Fabaceae</i> LINDL.			
2	<i>Gymnocladus dioicus</i> (L.) C. Koch	Northern America	2
1	<i>Laburnum anagyroides</i> Medik	Southern Europe	5
<i>Aceraceae</i> LINDL.			
9	<i>Acer platanoides</i> L.	Europe	10
7	<i>Acer pseudoplatanus</i> L.	Middle Europe, Caucasus	3

Table 1 cont.

№ on the scheme	Species name (Lat.)	Natural habitat	Total number of plants
<i>Hippocastanaceae</i> ET GRAY			
26	<i>Aesculus hippocastanum</i> L.	Southern Balkans	2
<i>Simarubaceae</i> LINDL.			
11	<i>Ailanthus altissima</i> (Mill.) Swingle	North China	1
<i>Anacardiaceae</i> LINDL.			
23	<i>Rhus typhina</i> L.	Northern America	1
<i>Vitaceae</i> LINDL.			
22	<i>Parthenocissus quinquefolia</i> (L.) Planch	Northern America	1
<i>Viburnaceae</i> L.			
19	<i>Viburnum opulus</i> L.	Eastern Europe, North Africa, Small Central Asia, Siberia	5
<i>Sambucaceae</i> LINK.			
20	<i>Sambucus nigra</i> L.	Western, Eastern Europe, Caucasus	1
<i>Oleaceae</i> LINDL.			
16	<i>Fraxinus exelsior</i> L.	Europe, West Asia, Caucasus	8
18	<i>Ligustrum vulgare</i> L.	Southern and Eastern Europe	41
Total angiosperms			160
Total			218

More than 218 species of trees and shrubs (including bushes in hedges) were found to grow on the grounds of the Potocki Family Palace. The total number of conifers consists of 58 individuals, deciduous – 160. Among the conifers in the regular plantings of the parter report, *Thuja occidentalis* ‘Columna’ and *Juniperus sabina* were dominant.

The analysis of dendroflora shows that the planting of introduced species of tree plants was not carried out systematically. Aboriginal species practically remained in the form of old-fashioned species of trees along the perimeter of the plot. They needed care and protection. The assessment of the qualitative state showed that the majority of plantations were in satisfactory condition, there was a decrease in their biological stability. This was due to inappropriate care and complex action of natural and man-made factors. Today, the palace and park complex needs to be restored to aesthetic attractiveness and requires a complementation of its composition in accordance with the overall spatial development of the city.

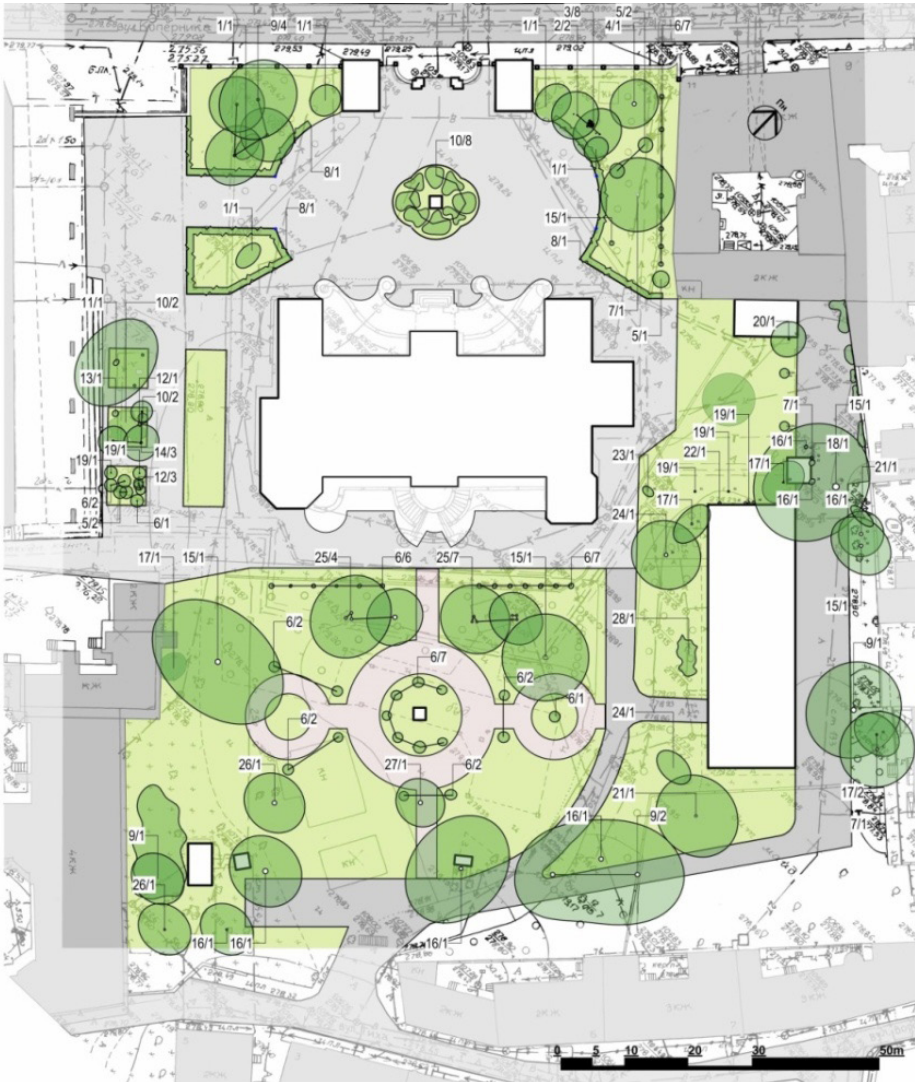


Fig. 10. The current situation of green plantations of the complex of the Potocki Family Palace, compare with Table 1 (survey and drawing by A. Kryvoruchko and V. Kryvoruchko, 2017)

2.4. FORMATION OF THE CONCEPTUAL PROPOSAL OF THE FUNCTIONAL, PLANNING AND SPATIAL SOLUTIONS OF THE OBJECT

A typical structure of a landscape design was used, along with a conceptual design-specific level of detail – featuring a plant survey, a reference plan with a combined dendroplan, working drawings of new plantings, the scheme of the general plan for the organization of landscaping and improvement of the project site.

In the planning and building of the site, one must take into account the boundaries and forms of use of the territories of cultural heritage monuments, cultural heritage protection areas, as well as UNESCO World Heritage Sites and their protected areas (buffer zones). This will help to preserve the traditional nature of the environment, as well as the context of the environment around individual systems. According to the legal provisions of Ukraine, around buildings and structures – during designing it is necessary to preserve valuable historical planning and settlement development, valuable natural landscape and objects of the nature reserve fund, observation points and areas from where one can observe panorama of sights and monuments as well as their complexes within a distance of not less than 50 m from cultural heritage monuments [20].

The purpose of the design is to reconstruct the existing landscape around the palace (with the remains of the historical park) with the preservation of its freeform plan and landscape character. The urgency of creating a natural oasis in a densely populated city is particularly important. The project provides for a partial replacement of tree plants and an adaptation of the site to the current needs of the city. The initial idea was to recreate the landscape park as featured in the early design of the site. However, growing urban functions impose many limitations. Therefore, an idea to revive the most iconic elements of the landscape park was accepted. Within the framework of the project, trees and shrubs that are self-sown and also do not correspond to the style of the complex, are to be eliminated. The boundaries of economic zones, the entrance to the palace and the system of tracks were also changed. A system of pedestrian connections that activate the space behind the palace and combine tangent streets and public spaces was proposed. Revitalized landscape is considered as a continuation of the artistic function of the palace. Various mobile and static artefacts have been designed for this purpose, which can create an arrangement of exhibition events and action games.

3. DESCRIPTION OF THE CONCEPTUAL DESIGN PROPOSAL

The main idea behind the conceptual proposal was the creation of “landscapes” of the park. Whereas the original layout of the site was basically destroyed, it is now a very topical task to recreate the ideas of the English garden that belongs to the palace. The proposed functional and planning model around the palace landscape divides it into four zones:

- a representative zone,
- a landscape and recreational zone with possible cultural functions,
- a transport zone (circulation and parking),
- a utilitarian and technical zone.

All zones have been laid out so as to ensure maximum functionality and comfort in the area. In the design, existing tracks have been transformed into smoother landscape elements, their coverage varies into small granite gravel, which is typical for parks and squares in the region. For the best expressiveness of the place, Moorish flowering lawns were arranged in front of the palace.

On other lawns, earthen embankments were placed to make the site more attractive. Some of the available plants were eliminated because they did not have landscape and historical value or were in poor condition. The passage of Tykha Street to the house of the Museum of the Old Books was planned to increase the area's integrity.

Also, the Museum of the Old Books is planned to be enclosed with a grid and Virginia creeper vines (*Parthenocissus quinquefolia* (L.) Planch.) are to be planted on the main and side facades and the rear with common ivy (*Hedera helix* L.). In this way, we will achieve a harmonization of the building with the environment and it will not escape from the context of the palace complex. We also carry out vertical landscaping of technical buildings. In the park behind the palace, a number of walking lanes was arranged, with an open lawn placed in the centre, which will be used for sitting and holding various events (Figs. 11 and 12).

In order to better express the system of connections between the site and the city, we made the entrance from Tykha Street public, and not only for business needs.

At the central entrance, the flowerbed will be expanded and the *Juniperus sabina* lawn will be replaced to produce a 'Moorish' lawn. In this way, we will reach the feeling that the palace is in the park.

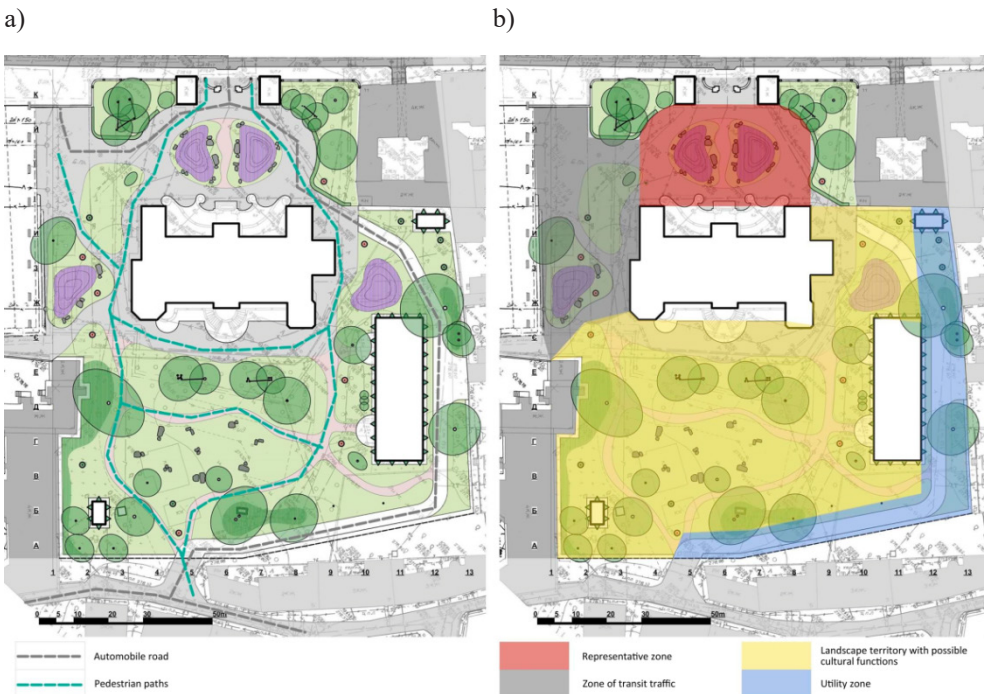


Fig. 11. Complex of the Potocki Family Palace: a) proposal of the master plan; b) scheme of functional zoning of the complex of the Potocki Family Palace (drawing by A. Kryvoruchko and V. Kryvoruchko, 2017)



Fig. 12. A general view of the proposed revalorization of the complex of the Potocki Family Palace (by A. Kryvoruchko and V. Kryvoruchko, 2017)

The main idea behind the composition is the scenic landscape park, which is achieved by a combination tall greenery groupings along the perimeter, curved paths and lawns (Tab. 2).

Table 2. Assortment list of proposed tree and shrub species

No.	Species name (Lat.)	Function in the composition	Total number of plants
1.	<i>Acer palmatum</i> ‘Atropurpureum’	Single plants to achieve contrast in the overall composition	9
2.	<i>Fraxinus exelsior</i> ‘Jaspidea’	Single plants and accents composition	7
3.	<i>Parthenocissus quinquefolia</i> (L.) Planch	Vertical landscaping	30
4.	<i>Hedera helix</i> L.	Vertical landscaping	10

4. CONCLUSIONS

The city of Lviv is an important cultural centre of Europe, and a careful attitude to the monuments of architecture and art is an integral part of preserving the historical heritage. The historical monument is, in its essence, not only a building, but also its environment, territory, landscape and the surrounding environment, which forms a whole architectural complex for man to perceive in a holistic manner. In a period of the active development of modern inno-

vative architecture in the city and beyond, one should not forget about the preservation and restoration of historical heritage, which is the most powerful visual conveyor of historical information. One of the most important architectural monuments of the city of Lviv is the Potocki Family Palace, at Copernicus Street (Kopernik Str. 15), which has prospects of development in the city cultural cluster.

REFERENCES

- [1] Petryshyn H.P., Ivanochko U.I. Poshuky novykh form rozvytku mista. In: Isayevych Y.D., Lytvyn M.R., Stebliy F.I., editors. *Istoriya L'vova*, vol. 2. Tsentr Yevropy, L'viv 2007, pp. 171–181.
- [2] Hauptstadt Lemberg, 1777. Scale: 1:1 440. Publisher: Author Josepho Daniele de Huber. Source: Courtesy of the Austrian War Archive, GIh 371 [on-line]. 2018. Available from: <http://www.lvivcenter.org/en/umd/mapdetails/hauptstadt-lemborg-1777> [accessed: 2018.07.07].
- [3] Koval'chuk K.I. *Osoblyvosti arkhitektury L'vova naprykintsi XVIII – pershoiy polovyny XIX st. Liha-Pres*, L'viv 2005.
- [4] Urban Media Archive. *City Maps: Lviv* [on-line]. 2018. Available from: <http://www.lvivcenter.org/en/umd/location/lviv> [accessed: 2018.07.07].
- [5] Magda F.A. *Reklama po lwowsku* [on-line]. 2018. Available from: <https://www.facebook.com/photo.php?fbid=941926535831909&set=a.566123300078903.1073741825.100000437146446&type=3&theater> [accessed: 2018.07.07].
- [6] *Plan Pałacu, ul. Kopernika 15*. In: Central State Historical Archive in Lviv (manuscript).
- [7] Zhuk I. *Vul. Kopernyka, 15 – kolyshniy palats Potots'kykh* [on-line]. 2018. Available from: <https://lia.lvivcenter.org/uk/objects/kopernyka-15/> [accessed: 2018.11.07].
- [8] Grankin P. *Lwowski architekt Julian Cybulski (1859–1924)*. In: *Statti (1996–2007)*. Tsentr Yevropy, Lviv 2010.
- [9] *Arkhitektura L'vova. Chas i styli XIII–XXI st.*, Biryulov Y., editor. Tsentr Yevropy, L'viv 2008.
- [10] Lviv Art Gallery [on-line]. Available from: <http://lvivgallery.org.ua> 2018 [accessed: 2018.07.07].
- [11] *Potocki Palace* [on-line]. 2018. Available from: <https://www.lvivcenter.org/uk/uid/picture/?pictureid=977/> [accessed: 2018.11.07].
- [12] *Palats Pototskoho* [on-line]. 2018. Available from: <https://twitter.com/PrytSLU/status/1016422685474246656> [accessed: 2018.11.07].
- [13] Petryshyn H.P., Sosnova N.S. *Prospekt Wolności punktem kulminacyjnym w poszukiwaniu samoidentyfikacji Lwowa*. In: Januchta-Szostak A., Banach M., editors. *Zrównoważone miasto – idee i realia*. Wydawnictwo Politechniki Poznańskiej, Poznań 2016, vol. 1, pp. 111–124.
- [14] Petryshyn H.P., Kryvoruchko O.Y., Lukashchuk H.B., Tupis' S.P. *The park in St. Yuri (St. George) square – the jewel in the emerald necklace of the city of L'viv*. *Czasopismo Techniczne. Architektura*, 2015, 112, 10-A (16), pp. 3–20.
- [15] *Istorychni architekturno-mistobudivni kompleksy: naukovi metody doslidzennia*. Petryshyn H.P., editor. L'viv politehnic, L'viv 2006.

- [16] Mistobudivne proektuvannya. Petryshyn H.P., Posatskyy B.S., Idak Y.V., editors. L'viv politehnic, L'viv 2016.
- [17] Pro zatverzhennya instruktsiyi z inventaryzatsiyi zelenykh nasadzhen' u naselenykh punktakh Ukrainy. Derzhbud Ukrainy; Nakaz, Instruktsiya vid 24.12.2001 № 226 [on-line]. Available from: <http://zakon2.rada.gov.ua/laws/show/z0182-02/2014> [accessed: 2018.11.07].
- [18] Takhtadzhyan A.L. Sistema mahnoliofitov. Nauka, Leningrad 1987.
- [19] Opredelitel' vysshikh rasteniy Ukrainy. Prokudin Y.N., editor. Naukova dumka, Kyiv 1987.
- [20] DBN 360-92** Planuvannya i zabudova terytoriy. Kyiv 1992.

Justyna Durak*, **Anna Miernik***, **Agnieszka Jaworska***, **Alicja Skiba****,
Przemysław Furman**, **Katarzyna Styszko***

REMOVAL OF PHARMACEUTICALS RESIDUES AND PERSONAL CARE PRODUCTS BY ADVANCED OXIDATION TECHNIQUES

Abstract

The dynamically developing pharmaceutical market and increased consumption of medicines cause the increase of the pollution of the aquatic environment with pharmaceuticals and products of their partial decomposition. Many other compounds are also emitted into the aqueous environment from the wide use of personal care, cleaners and disinfectants. These include triclosan, a bactericidal compound or bisphenol, a popular antioxidant. These compounds are released into the environment mainly along with municipal wastewater and as biologically active substances can be an ecotoxic threat to aquatic organisms and humans. As much as 34% of the pharmacy drug markets in Poland are over-the-counter medicines and they are detected in the environment most frequently and in the largest concentrations.

The aim of the study was the evaluation of the removal efficiency of selected emerging contaminants such as pharmaceutical residues using ozonation and catalytic processes. The aim of the study was also to determine the time of the photocatalysis and ozonation process on the degree of degradation of pharmaceutical compounds. The analysis of the content of the tested compounds was carried out using liquid chromatography with UV-Vis detector.

Keywords

emerging contaminants, photolysis, oxidation, wastewater, treatment

1. INTRODUCTION

In the last decades, pollution of the aquatic environment has become a very important issue. The attention of research community focused mainly on the so-called priority pollutants included in the European Union Water Framework Directive, that include,

* AGH University of Science and Technology, Faculty of Energy and Fuels, Krakow, Poland;

** AGH University of Science and Technology, Faculty of Physics and Applied Computer Science, Krakow, Poland;
corresponding author: styszko@agh.edu.pl

among others compounds from the group of polycyclic aromatic hydrocarbons, heavy metals and their compounds [1, 2]. In addition to these pollutants, huge quantities of other chemicals are released into surface and underground waters, the impact of which on the environment and humans is not fully investigated yet. These substances are called the term emerging contaminants (EC's) [3]. The precise specification of this term still gives scientists many difficulties, however, one can distinguish several characteristics of EC's. These are compounds permanently introduced into the environment and their main source is human anthropogenic activity. The exact determination of their presence and the risks they pose for the aquatic ecosystem is still ongoing, but there are no effective methods for detecting compounds belonging to this group [4]. The representatives of emerging contaminants are pharmaceuticals and their metabolites. The increase in production and consumption of medicines generates the problem of their presence in the natural environment. Figure 1 presents the main sources of pharmaceuticals and their fate in the environment.

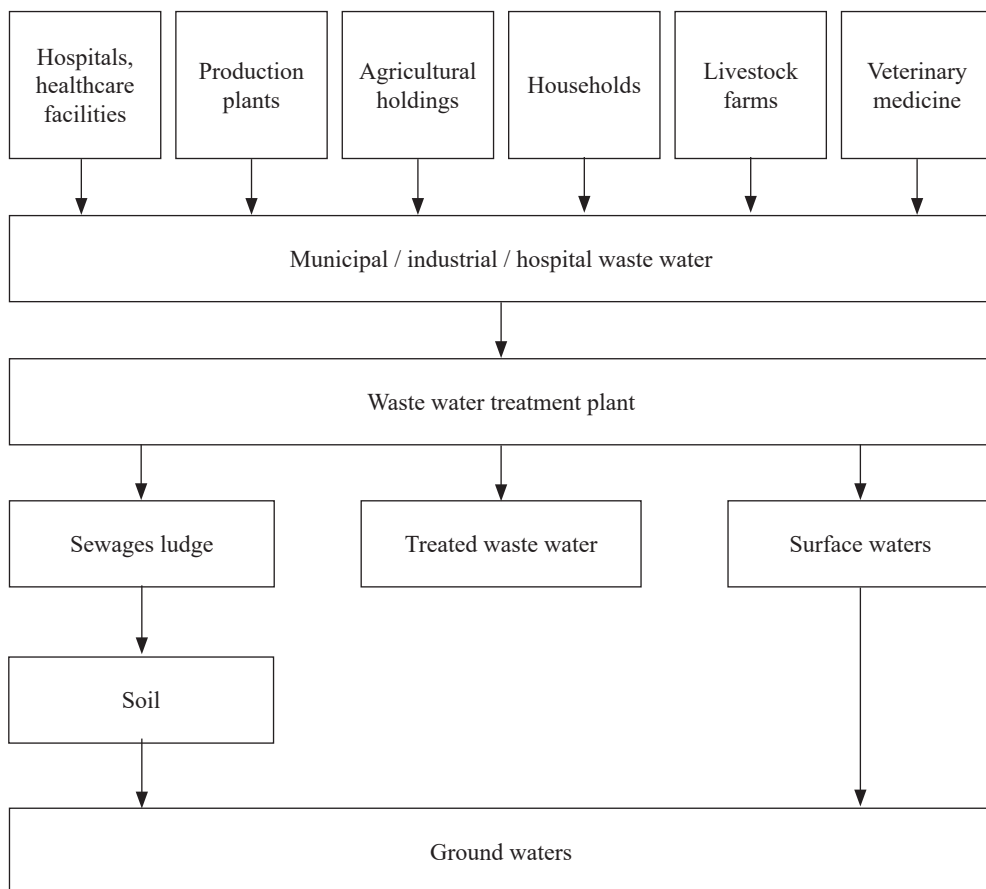


Fig. 1. The main sources of pharmaceuticals and their fate in the environment [4]

Their prevailing source are the places where huge amounts of drugs are consumed every day, that is hospitals and healthcare facilities. Also, farm and breeding farms, veterinary medicine, as well as households, where the consumption of drugs is increasing from year to year, provide a large amount of pharmaceuticals. Another source that generates a huge amount of sewage containing pharmaceuticals is the pharmaceutical industry [4]. Pharmaceuticals are excreted into the environment unchanged or in the form of metabolites together with urine and feces. EC's in the body undergo chemical and structural changes, and the most important biotransformations occur in the liver. This takes place in two phases. In the first phase, products are more toxic and active than the starting products. Phase II usually causes the deactivation of the drug [5]. The transformation products of pharmaceuticals that arise in an aqueous environment may show a higher activity and a stronger toxicological effect than the parent substance, and as consequently a mutagenic effect [6, 7].

Pharmaceuticals that get into the soil and water environment affect all living organisms. Due to the fact that they are chemically stable and have a slow decomposition process, they can accumulate in ecosystems [8]. Ibuprofen, ketoprofen, diclofenac, naproxen belong to the group of non-steroidal anti-inflammatory drugs. They are one of the most frequently used group of therapeutics, which results from the fact that they provide benefits in the case of many diseases, and are additionally available without a prescription [9]. In the case of a long exposure of the body to these drugs, there is a risk of pathological changes in the tissues of organs, especially those that are responsible for the metabolism of medicines. For aquatic organisms such as phytoplankton and zooplankton, diclofenac is considered the most toxic of these drugs. However, the most toxic is mixing pharmaceuticals, because the resulting mixture causes reproductive disorders of many species of aquatic organisms [10].

Conventional waste water treatment based mainly on activated sludge technology is not directed to removing this type of pollution, which means that they are continuously released into the aquatic environment at concentration levels of the order of $\text{ng}\cdot\text{L}^{-1} - \mu\text{g}\cdot\text{mL}^{-1}$ [5]. This is due to the fact that pharmaceuticals are not very susceptible to biodegradation and sorption on sediments, but some are photodegradable to a large extent [11]. In connection with the above an alternative to these methods or their supplementation are Advanced Oxidation Processes (AOP) [12]. AOP techniques mainly shall use free radicals, in particular hydroxyl radicals ($\text{OH}\cdot$) as an oxidizing agent. The generation of hydroxyl radicals occurs, among others, under the influence of hydrogen peroxide, UV radiation, ozone and the addition of catalysts such as titanium oxide (IV) or manganese oxide (IV). AOP is related to the high oxidation potential of hydroxyl radicals, which amounts to 2.8 V, and their ability to very quickly entering into chemical reactions with organic compounds [13]. AOP can be divided into two main groups: photochemical processes, where photolysis is classified and chemical processes among which ozonation is distinguished [12]. The efficiency of advanced oxidation processes depends on several factors. First of all, the concentration and type of organic pollutants as well as the presence and concentration of other compounds, both organic and inorganic, that may cause an increase or decrease in the rate of production of hydroxyl radicals (these include, for example, iron (II) ions, copper (I), carbonates, chlorides, bicarbonates, isopropanol). AOP processes depend on the properties

of the environment in which contamination occurs: pH, turbidity. Another factor is the impact of oxidant-pollution resulting from: the type and concentration of oxidants, the ratio of concentrations of pollutants and oxidants, reaction time, wavelength in the case of photochemical processes. Efficiency depends also on the location of the AOP method in the technological scheme of a sewage treatment plant or a water treatment plant [14, 15].

2. MATERIALS AND METHODS

Table 1 provides the physical and chemical properties and structures of the compounds investigated in the current study. In order to eliminate selected pharmaceutical contaminants from model aqueous solutions used advanced purification techniques, i.e. UV photolysis and ozonation. In the photolysis process as the oxidizing agent is used ultraviolet radiation. The system to evaluate the effectiveness of UV photolysis in removing pharmaceutical contaminants consisted of three main component: a high-pressure mercury vapour lamp (125 W, POLAMP), a magnetic stirrer and a reaction vessel made of quartz glass. In the ozonation process, the source of ozone was the N_2O_2C ozone generator from Eltom, which generated ozone based on the corona discharge process. Ozone was produced from atmospheric oxygen in the air by providing enough energy to break the bonds between oxygen atoms [16].

The compounds targeted in the experiments were pharmaceuticals belonging to three different therapeutic groups.

1) Nonsteroidal anti-inflammatory drug (NSAIDs):

- ibuprofen (IBF) ($\geq 99.0\%$, Dr. Ehrenstorfer GmbH, Germany),
- ketoprofen (KTP) ($\geq 99.9\%$, Sigma-Aldrich, USA),
- diclofenac (DCF) ($\geq 98.0\%$, Sigma-Aldrich, USA),
- naproxen (NPX) ($\geq 99.0\%$, Sigma-Aldrich, USA),

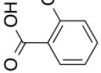
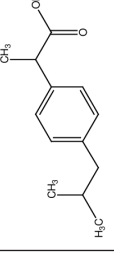
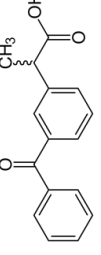
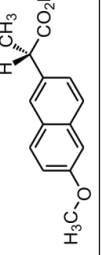
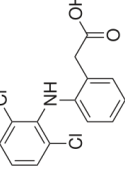
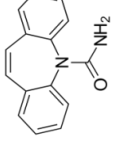
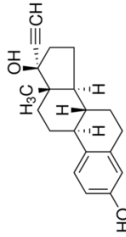
they are the most commonly used medicines.

2) Carbamazepine (CBZ) ($\geq 99.0\%$, Sigma-Aldrich, USA) is currently one of the most commonly used medicines in management of epilepsy. In addition, it is also used in the treatment of manic-depressive illness.

3) 17- α -ethinylestradiol (EE2) ($\geq 98.0\%$, Sigma-Aldrich, USA) is a synthetic estradiol derivative and the main component of oral contraceptives. Salicylic acid (SAL) ($\geq 99.5\%$, Dr. Ehrenstorfer GmbH, Germany) is a metabolite of acetylsalicylic acid.

Methanol was used to prepare solutions of the compounds both singly and as a mixtures. Acetonitrile (HPLC super gradient grade) and methanol (HPLC super gradient grade) were purchased from Avantor Performance Materials Poland S.A. (Gliwice, Poland). Deionized water ($< 0.07 \mu S \cdot cm^{-1}$), used for a standard solution, sample solvents and HPLC system eluent preparation, was obtained from the HLP5 pure water system (Hydrolab, Gdańsk, Poland).

Table 1. Physicochemical characteristics of pharmaceuticals and metabolites studied [4]

Compounds	Therapeutic group	Molecular structure	Molecular weight [g·mol ⁻¹]	pK _a	logK _{ow}	Half-life [h]	Water solubility (25°C) [mg·L ⁻¹]
Salicylic acid (SAL)			138.12	2.97	2.24	2–3	2240
Ibuprofen (IBF)			206.29	4.91	3.79	1.5–2.5	21
Ketoprofen (KTP)	Anti-inflammatory and analgesic drugs		254.29	4.45	3	1.5–2.5	51
Naproxen (NPX)			230.27	4.15	3.1	13–15	15.9
Diclofenac (DCF)			318.14	4.15	4.02	1–2	2.37
Carbamazepine (CBZ)	Psychotropic drug		236.27	13.9	2.45	16–24	112
17 α-ethinyl estradiol (EE2)	Hormones or steroids		296.41	10.5	4.12	13	11.29

3. ANALYTICAL PROCEDURES

A stock standard solutions of the analyzed compounds at a concentration of $1000 \mu\text{g} \cdot \text{mL}^{-1}$ for each compound was used to spike water samples. Both in the process of ozonation and photolysis, the volume of the tested solutions was 50 mL. The concentrations of tested compounds in aqueous solutions were determined by HPLC-UV/Vis – Varian Star liquid chromatograph equipped with 9012 pump, 9050 UV-Vis detector, 9100 autosampler and Kinetex, XB-C18 column (75 mm long, 4.6 mm diameter, $2.6 \mu\text{m}$ filling in core-shell technology, Phenomenex, USA). The mobile phase was acetonitrile in isocratic elution and flow rate $1 \text{ mL} \cdot \text{min}^{-1}$. Wavelength was established at 210 nm. The injection volume was $25 \mu\text{L}$.

The process of UV photolysis was carried out at the initial concentrations of the analyzed substances $10 \mu\text{g} \cdot \text{mL}^{-1}$ and $20 \mu\text{g} \cdot \text{mL}^{-1}$, to assess the effect of the initial concentration of analytes on the efficiency of their removal in the process of UV photolysis. The UV photolysis process was carried out for 60 minutes. Samples with a volume of $100 \mu\text{L}$ from irradiated solutions were taken sequentially at 15 minutes, to determine the changes in concentration of the analytes in solution.

The ozonation process was carried out at the initial concentration of the analyzed substances $10 \mu\text{g} \cdot \text{mL}^{-1}$. In order to determine removal efficiency of analyte over time, samples of $100 \mu\text{L}$ volume, were taken every 3 minutes. O_3 was generated by an ozone generator and injected continuously into the reactor at a flow rate of 0.2 or 0.5 or $0.8 \text{ L} \cdot \text{min}^{-1}$, and dose of ozone after 12 minute, 2.5 mg, 7.4 mg and 9.7 mg, respectively. Ozone concentration of O_3 , was quantified using iodometric method (PN-Z-04007-2) with using UV-Visible Spectrophotometer Cintra 10 (GBC Scientific Equipment) at 580 nm.

4. RESULTS AND DISCUSSION

To evaluate removal efficiencies for individual pharmaceuticals in the experiments of UV photolysis / ozonation, the concentrations of compounds were determined in the solutions by samples taken at successive time intervals. The degree of the elimination of pharmaceutical contaminants was defined as their percentage loss calculated on the basis of concentration changes, according to the formula:

$$\text{Removal efficiency} = \frac{(c_0 - c)}{c_0} \cdot 100 [\%] \quad (1)$$

where:

- c_0 – concentration of initial solution,
- c – concentration at time interval.

Table 2 presents the results of the comparative analysis and the selection of the most optimal conditions of the studied processes. To each of the analyzed compounds, an optimal parameters of the method was selected that allowed the highest degree of elimination in these conditions and so the economic aspect was also taken into account in the considerations.

Generally, the removal of the compounds increases with increasing ozone dose. It was also indicated that extending the duration of the process increases the level of removal of pharmaceuticals. It depends on different molecular structures of the investigated compounds. Some compounds react fast with ozone, while others react slower and then the reaction with hydroxyl radicals will be important for the degradation of the compound [17].

The process of UV photolysis did not allow the complete removal of any of the tested compounds. The pharmaceuticals most susceptible to the process of UV photolysis were three nonsteroidal anti-inflammatory drugs: ibuprofen, ketoprofen and diclofenac. For these compounds, the elimination level of over 95% to 99% was achieved. Unfortunately for carbamazepine this process proved to be the least effective for. It was only removed in 7%. Analysis of the effectiveness of the removal of salicylic acid and 17- α -ethinylestradiol in the ozonation process showed their complete elimination from the solution. A high result was also obtained, over 99% for ozonation of carbamazepine. Naproxen is the only compound for which the removal efficiency in the processes of UV photolysis and ozonation was at a very similar level – over 80%.

Table 2. Removal efficiencies of pharmaceuticals analytes in UV photolysis and ozonation processes in relation to the optimal parameters

Compound	UV photolysis		Ozonation	
	time of photolysis [minutes]	removal efficiency [%]	dose of ozone [mg]	removal efficiency [%]
IBF	45	99	9.3	89
NPX	60	83	7.4	88
KTP	30	>99	9.3	37
DCF	30	95	7.4	89
CBZ	30	7	2.5	> 99
SAL	60	68	5.6	100
EE2	60	84	0.6	100
extending the time to improve efficiency			greater removal efficiency	

In the case of UV photolysis, the prolongation of the exposure time of the solutions positively influenced the degree of degradation of the tested substances. Similar relations were observed in work by M. Dudziak and E. Burdzik-Niemiec [18] Studies conducted out in this work show that the use of ozone significantly reduces the concentration of pharmaceutical contaminants, and according to A. Węgrzyn et al. [19] also reduces the pharmacological and toxicological activity of these compounds. The authors explained this effect by modifying functional groups responsible for their biochemical action. However, it should be noted that not all pharmaceuticals exhibit the same reactivity to molecular ozone, hence some of them are relatively resistant to the ozonation process, such as ketoprofen.

The use of UV photolysis and ozonation on a technical scale requires consideration of many factors that are crucial in achieving the high efficiency of degradation of pharmaceutical contaminants. The most important of them is the complex matrix of real wastewater. In this work, the effectiveness of UV photolysis and ozonation processes for the removal of pharmaceutical contaminants from model aqueous solutions was investigated. Wastewater, on the other hand, is a mixture of a large number of pharmaceutical compounds (and others) that can cause antagonistic or synergistic effects [19].

5. CONCLUSION

Analysis of the obtained results allows to conclude that both UV photolysis and ozonation can be successfully used to remove the tested pharmaceuticals and metabolite. It was proven that ozone treatment at a dose between 7.4 and 9.3 mg was highly efficient. However, the use of UV photolysis has been shown as less effective. Most of the tested pharmaceuticals were completely eliminated or their concentration was drastically reduced after ozone oxidation. This was the case of EE2, salicylic acid, ibuprofen, diclofenac, naproxen and carbamazepine. The only exception was ketoprofen, which seems more persistent and difficult to degrade.

The highest removal efficiency of the majority of tested drugs from the NSAIDs group was obtained for the process of UV photolysis. Only naproxen was degraded at a similar level by both AOT removal techniques used. The process of photolysis for carbamazepine, which is a hardly degradable drug, has proved to be ineffective (removal efficiency <7%).

Different durations of both processes and different ozone dose were used. Removal of pharmaceuticals is a process that needs an individual approach to each of them. Some of EC's are susceptible to both the AOT techniques, others only to one of these processes and the rate of degradation of these compounds is also different.

ACKNOWLEDGEMENTS

This work partially financed by AGH UST Rector Grant No. 68/2018 and by the AGH UST statutory tasks No. 16.16.210.476 within subsidy of the Ministry of Science and Higher Education.

REFERENCES

- [1] Ricci M., Kourtchev I., Emons H. Chemical water monitoring under the Water Framework Directive with Certified Reference Materials, *TrAC Trends in Analytical Chemistry*, 2012, 36, pp. 47–57. DOI: 10.1016/j.trac.2012.03.006.
- [2] Directive 2000/60/EC of the European Parliament and of the Council of 23 October 2000 establishing a framework for Community action in the field of water (Official Journal L 327, 22/12/2000 P. 0001–0073).
- [3] Yarsan E., Yipel M. The Important Terms of Marine Pollution “Biomarkers and Biomonitoring, Bioaccumulation, Bioconcentration, Biomagnification”. *Molecular Biomarkers & Diagnosis*, 2013, 4, pp. 1–4. DOI: 10.4172/2155-9929.S1-003.

- [4] Daughton C.G. Non-regulated water contaminants: emerging research. *Environmental Impact Assessment Review*, 2004, 24, 7–8, pp. 711–732. DOI: 10.1016/j.eiar.2004.06.003.
- [5] Aubertheau E., Stalder T., Mondamert L., Ploy M.-C., Dagot C., Labanowski L. Impact of wastewater treatment plant discharge on the contamination of river biofilms by pharmaceuticals and antibiotic resistance. *Science of the Total Environment*, 2017, 579, pp. 1387–1398. DOI: 10.1016/j.scitotenv.2016.11.136.
- [6] Koszowska A., Ebisz M., Krzyśko-Łupicka T. Obecność farmaceutyków i środków kosmetycznych w środowisku wodnym jako nowy problem zdrowia środowiskowego. *Medycyna Środowiska – Environmental Medicine*, 2018, 18, 1, pp. 62–69.
- [7] Rashed M.N. Biomarkers as indicator for water pollution with heavy metals in rivers. *Seas and Oceans*, South Valley University, Egypt 2001.
- [8] Stepnowski P., Synak E., Szafranek B., Kaczyński Z. Monitoring i analityka zanieczyszczeń w środowisku. Wydawnictwo Uniwersytetu Gdańskiego, Gdańsk 2010.
- [9] Sosnowska K., Styszko-Grochowiak K., Gołaś J. Leki w środowisku – źródła, przemiany, zagrożenia. *Krakowska Konferencja Młodych Uczonych 2009*, pp. 395–404.
- [10] Szymonik A., Lach J. Zagrożenie środowiska wodnego obecnością środków farmaceutycznych. *Inżynieria i Ochrona Środowiska, Politechnika Częstochowska, Instytut Inżynierii Środowiska 2012*, 15, 3, pp. 249–263.
- [11] Ellis J.B. Pharmaceutical and personal care products (PPCPs) in urban receiving waters. *Environmental Pollution*, 2006, 144, 1, pp. 184–189. DOI: 10.1016/j.envpol.2005.12.018.
- [12] Domagała M., Wano B. Wpływ niesteroidowych leków przeciwzapalnych (NLPZ) na środowisko wodne oraz metody ich usuwania z wód. *Technologia Wody*, 2019, 1, 63, pp. 46–49.
- [13] Sosnowska K., Styszko K., Gołaś J. Wstępne ozonowanie wybranych farmaceutyków w ściekach komunalnych z oczyszczalni Kraków-Płaszów. *Proceedings of EC Opole*, 2011, vol. 5, No. 2, pp. 601–607.
- [14] Wileńska D. Zaawansowane metody utleniania zanieczyszczeń organicznych. *Katedra Technologii Środowiska Instytutu Ochrony Środowiska i Zdrowia Człowieka Wydziału Chemii Uniwersytetu Gdańskiego*, Gdańsk 2012.
- [15] Czerwiński J., Kłonica A., Ozonek J. Pozostałości farmaceutyków w środowisku wodnym i metody ich usuwania. *Czasopismo Inżynierii Łądowej, Środowiska i Architektury*, 2015, 62, pp. 27–42.
- [16] Kanakaraju D., Glass B.D., Oelgemöller M. Advanced oxidation process-mediated removal of pharmaceuticals from water: A review. *Journal of Environmental Management*, 2018, 219, pp. 189–207. DOI: 10.1016/j.jenvman.2018.04.103.
- [17] Hansen K.M.S., Spiliotopoulou A., Chhetri R.K., Escola M., Bester K., Andersen H.R. Ozonation for source treatment of pharmaceuticals in hospital wastewater – Ozone lifetime and required ozone dose. *Chemical Engineering Journal*, 2016, 290, pp. 507–514.
- [18] Dudziak M., Burdzik-Niemiec E. Badania porównawcze rozkładu wybranych estrogenów i ksenoestrogenów w procesie UV i UV/O₃. *Proceedings of EC Opole*, 2015, 9, pp. 589–595.
- [19] Węgrzyn A., Machura M., Żabczyński S. Możliwości usuwania środków cieniujących ze ścieków. *Ochrona Środowiska*, 2015, 37, pp. 55–63.

Alicja Skiba^{*}, Przemysław Furman^{*}, Justyna Durak^{}, Natasza Dobrowolska^{**},
Natalia Guzik^{**}, Damian Zięba^{***}, Magdalena Kistler^{****}, Anne Kasper-Giebl^{****},
Katarzyna Styszko^{**}**

CHEMICAL COMPOSITION OF ATMOSPHERIC AEROSOLS COLLECTED IN KRAKOW AGGLOMERATION

Abstract

Atmospheric aerosols constitute a complex mixture of organic and inorganic compounds and biological materials. Over the last few decades a concern over the health effects associated with air pollution was growing. Long and frequent exposure of organism to polluted air and inhalation of ambient particles may lead to the loss of the ability for the removal of heavy metals and other toxic substances from the respiratory tract what the antioxidants are responsible for. This may lead to the various diseases and other organism handicaps development. Particulate matter are emitted during numerous combustion processes, mostly forced by anthropogenic activities like various transportations using gasoline and diesel engines or fossil fuels combustion processes. Residential heating systems as wood-like biomass, coal utilizing and incineration of solid waste were researched as well. The aim of the study was determination of chemical composition of atmospheric aerosols collected in Krakow agglomeration. Samples were collected from February 2017 to October 2017 in Wadowice. All samples were collected on quartz fibre filters and represent PM10 fraction collected with 24 h resolution. The analytical work comprised thermo-optical carbon analysis, determination of major inorganic ions by means of ion chromatography and determinations of PAHs by means of GCMS.

Keywords

particulate matter, sources apportionment, combustion, carbonaceous fraction, secondary pollution

^{*} AGH University of Science and Technology, Faculty of Physics and Applied Computer Science, Krakow, Poland;

^{**} AGH University of Science and Technology, Faculty of Energy and Fuels, Krakow, Poland;

^{***} Krakow Smog Alert, Krakow, Poland;

^{****} TU Wien, Institute of Chemical Technologies and Analytics, Vienna, Austria;
corresponding author: styszko@agh.edu.pl

1. INTRODUCTION

The condition of atmospheric air in Krakow depends on many natural and artificial factors. Krakow and the majority of agglomerations located in the neighboring area are located in the valley which disturbs the city's ventilation. Furthermore, in Krakow we can often notice windless days (30%) and for the next 30–40% of the time the wind does not exceed 2 m/s. Furthermore, Krakow and nearest agglomerations (e.g. Wadowice) are located in an unfavorable position due to the landform – it is surrounded by hills which inhibit natural processes of wind circulation. However, not only geographical location is the reason for the appearance of low air quality. The other reasons to mention are meteorological factors, compact and low housing and service development, combustion of solid fuels in the municipal, housing sector and in the industrial sector [1].

The significant influence on the quality of air pollution is emission to the environment during coal combustion in outdated boilers and domestic furnaces. Quality of the fuel plays here the important role – it has often low calorific value. Better quality of fuel enforces higher prices of these goods. The citizens who want to avoid additional expenses decide to use various types of dry waste (bottles, papers, etc.) as fuel. These processes contribute to the pollution of atmospheric air with harmful compounds that have a negative impact on the natural environment and the human health. The most frequently occurring compounds include oxides of carbon, sulfur and nitrogen, dioxins, furans, polycyclic aromatic hydrocarbons (PAHs) and carbonaceous fractions [2].

The group of the most widespread and particularly dangerous atmospheric pollutants in the present times includes particulate matter (e.g. PM₁, PM_{2.5}, PM₁₀). They have sorptive properties, and thus, other harmful compounds may be deposited on their surface [2].

Carbonaceous aerosols are divided into two main categories: organic carbon (OC) and elemental carbon (EC). The summary concentration of these two carbonaceous groups is referred as total carbon (TC). Elemental carbon is primary pollutant released into the atmosphere as remnants of incomplete combustion of petrol and oil from transport, as well as other anthropological sources like woodburning, agricultural burning or just domestic heating using coal combustion. Sometimes EC is formed naturally for example during forest fires. In the literature, the popular terms for elemental carbon are also “soot”, “black carbon”, “light absorbing carbon”. EC can be transported hundreds of kilometers from the place of its formation.

Organic carbon can originate as primary organic aerosol (POA) from primary anthropogenic emission sources directly emitted to the atmosphere as well as natural biogenic sources (for example bacteria, pollens, dungal spores). The other type of OC is referred as secondary organic aerosol (SOA) and it is formed through atmospheric reactions including oxidation of gaseous organic precursors and further gas-to-particle conversion processes.

For living organisms, particulate matter containing polynuclear aromatic hydrocarbons are the most dangerous because of their carcinogenic and mutagenic properties. The strongest carcinogens are benzo[a]pyrene and dibenzo[a,h]anthracene. They contribute to the formation of various types of diseases like allergies, asthma, cancer and, in the worst case, inhalation of this type of pollution can even lead to death. They got the ability to form covalent bonds with DNA and RNA molecules. This causes cancerous changes in the cells of the body. Polycyclic aromatic

hydrocarbons constitute a large group of organic compounds (about 10,000) that have always existed in the environment, but the development of civilization and technology has increased exposure to these compounds, and thus has a negative impact on the environment and harmful health effects as well as affects the acquired food in which harmful compounds accumulate [3]. PAHs are a group of chemical compounds that arise naturally or as a result of human activity in the course of pyrolysis processes or incomplete combustion of organic substances, including wood, coal, oil and its products as well as during the process of petrochemical processes, food processing, smoking, etc. These compounds are widely distributed in the environment, found in air, soil and water. Depending on the conditions, they can be absorbed through the airways in the form of solid aerosols, through the skin or the digestive tract after being taken up with drinking water and food. It should be mentioned that many of these pollutants do not have clearly defined concentration standards in the air and there is no information on their interaction with the environment, and above all with the human body [1, 4].

These consequences forced people to find a new methods of air protection, which are mainly based on preventing exceeding the permissible concentrations of pollutants and limiting or eliminating emissions of these compounds to the atmosphere.

2. METHODS

The analysis of the composition of PM₁₀ dust samples taken from the area of Wadowice (January–October 2017) was performed. According to a report by the World Health Organization (WHO), in 2016 Wadowice was classified as the twentieth most polluted city in the European Union. The city is located about 50 km from Krakow. The population of Wadowice is about 19,000 inhabitants with population density about 1,800/km².

Quartz-fiber filters (Whatman QM-A) with a diameter of 47 mm were used for the research. All samples of the PM₁₀ fraction were taken using a low-volume sampler Atmoservice PNS-15 and represent PM₁₀ fraction collected with 24 h resolution. The first stage of the conducted tests was conditioning quartz fiber filters consisting of a thermal purification process at a temperature of 550°C for 5 hours. After thorough cleaning, the filters were cooled to a constant temperature and each of them was weighed three times. The mass of PM₁₀ was calculated as a difference of mean masses of filters after and before sampling, respectively.

2.1. ANALYSIS OF THE INORGANIC IONS

The concentration of the inorganic cations and anions were analysed with isocratic ion chromatography on an ICS-1100 instrument (Thermo Scientific). The circular filter aliquots (ø 8 mm) per sample were extracted in either 1.5 mL of extra pure water or in 1.5 mL of the 12 mM methanesulfonic acid (MSA) in order to determine the anions and cations concentration, respectively. ICS-1100 was equipped with an autosampler AS-DV and ion-exchange columns: Ion Pac AS22 (4 × 250 mm) for anions, mobile phase: 4.5 mM Na₂CO₃ + 1.4 mM NaHCO₃; CS16 (5 × 250 mm) for cations, mobile phase: 12 mM MSA. After electrochemical suppression (AERS 500 (4 mm) and CERS500 (4 mm) suppressors), quantification was performed with a conductivity detector. The injection volume was 25 µL and the flow rate was 1.2 mL/min [5].

2.2. ANALYSIS OF CARBONACEOUS FRACTION

The punches of 1 cm diameter were used (without pre-treatment) to analyze the concentration of organic and elemental carbon by the thermo-optical method for OC/EC analysis (OC/EC analyzer by Sunset Laboratory OCEC Aerosol Analyzer) followed by the EUSAAR2 (European Supersites for Atmospheric Aerosol Research) [1].

The EUSAAR2 temperature program has the first stage with four steps (200°C for 120 seconds; 300°C for 150 seconds; 450°C for 180 seconds; 650°C for 180 seconds) in pure helium atmosphere and the second stage with four steps (500°C for 120 seconds; 550°C for 120 seconds; 700°C for 70 seconds; 850°C for 80 seconds) in an oxidizing atmosphere (final concentrations of oxygen / helium are 2% / 98% in the sample oven). In the initial phase organic compounds are vaporized and oxidized to CO₂ but some percent of the organics may be pyrolytically converted to elemental carbon. During the second phase both the original elemental carbon and that produced by pyrolysis during the first phase are oxidized to CO₂. The CO₂ produced during both phases is detected by a non-dispersive infrared detector. At the end of each analysis period the instrument is automatically calibrated by injecting calibration gas (5% methane in He). The optical properties of the sample are monitored before and during the analysis with a laser which makes it possible to correct the result of pyrolysis. While the laser beam returns to pre-pyrolysis value after decreasing during organic carbon charring in helium stage the split point between OC and EC can be obtained. However, sometimes samples need manual correction of the split point due to unexpected fluctuation on the laser graph.

Accuracy and repeatability of results were regularly controlled on the basis of the determination of sucrose containing 50 µg of carbon in 10 µL of solution or by using reference filters.

2.3. ANALYSIS OF PAHS

The circular filter aliquots with a diameter of 22 mm were cut from the filters and then spiked with 10 µL (10 ng/µL) BaP D12 (benzo[a]pyrene D12) solution, after that extracted twice with 3 mL dichloromethane and 2 mL cyclohexane, for 40 min. The volume of combined extracts were reduced to 250 µL, using gentle stream of argon at 35°C. The concentrate was finally transferred into chromatographic vial and analysed with GC/MS. To analyse Polycyclic Aromatic Hydrocarbons (PAHs) Thermo Scientific GC Trace 1310 gas chromatograph coupled with the ITQ 900 ion trap mass spectrometer and a TriPlus RSH autosampler was applied. The detection mode used for identification was selective ion monitoring with a specific mass and ion charge ratio m/z (SIM) and identification of all ions within a fixed range of molecular weights. A 30 m fused silica ZB-PAH capillary column (0.25 mm ID, 0.25 µm film thickness) was used for separation. The temperature program for the PAH compounds consisted of a 4 min hold at 70°C, a ramp of 20°C/min to 280°C, and then ramp of 20°C/min to 300°C. Helium was used as a carrier gas with flow 1 mL/min. The 1 µL concentrates are injected into the splitless mode. The injector temperature was maintained at 280°C. Concentrations were determined for a total number of 16 PAHs (acenaphthene, acenaphthylene, anthracene, benz[a]anthracene, benzo[a]pyrene, benzo[b]fluoranthene, benzo[k]fluoranthene, benzo[ghi]perylene, chrysene, dibenz[a,h]anthracene, fluoranthene, fluorene, indeno[1,2,3-c,d]pyrene, naphthalene, phenanthrene, pyrene).

3. RESULTS AND DISCUSSION

The average, minimum and maximum values of PM10 and main chemical components concentration are given in Table 1. The results are divided into heating and non-heating periods.

The gravimetrically measured PM10 concentration during the study period equalled $34.39 \mu\text{g}/\text{m}^3$ on average, varying from 10.80 – $116.77 \mu\text{g}/\text{m}^3$. The daily maximum value for PM10 in ambient air, set up within the European Commission directive 2008/50/CE ($50 \mu\text{g}/\text{m}^3$), was exceeded 33 times during the measurement period. The highest concentrations of PM10 were reported on between March 8th and March 28th with the maximum reported concentration of $116.77 \mu\text{g}/\text{m}^3$ on March 14th. In this period the diurnal mean ambient temperature varied between 6 and 16°C . The lowest concentration of PM10 was noted at the August 20th and equalled $10.8 \mu\text{g}/\text{m}^3$ (temperature: 15°C).

Table 1. Concentrations of PM10 constituents during the study period

				Heating season			Non-heating season		
	Min	Max	Average	Min	Max	Average	Min	Max	Average
PM10 [$\mu\text{g}/\text{m}^3$]	10.80	116.77	34.39	21.15	116.77	59.26	10.80	91.30	29.15
Cations									
Na ⁺ [$\mu\text{g}/\text{m}^3$]	1.15	4.45	1.90	1.79	3.52	2.37	1.15	4.45	1.80
NH ₄ ⁺ [$\mu\text{g}/\text{m}^3$]	0.25	5.01	1.18	0.31	5.01	2.01	0.25	4.76	1.00
Mg ²⁺ [$\mu\text{g}/\text{m}^3$]	0.017	1.602	0.289	0.018	1.068	0.488	0.017	1.602	0.242
K ⁺ [$\mu\text{g}/\text{m}^3$]	0.32	1.01	0.49	0.40	0.78	0.52	0.32	1.01	0.49
Ca ²⁺ [$\mu\text{g}/\text{m}^3$]	0.022	3.196	0.779	0.023	1.863	0.802	0.022	3.196	0.778
Anions									
NO ₃ ⁻ [$\mu\text{g}/\text{m}^3$]	0.40	12.03	1.91	1.15	12.03	3.35	0.40	9.39	1.64
F ⁻ [$\mu\text{g}/\text{m}^3$]	0.049	0.069	0.058	0.049	0.069	0.058	<LOQ	<LOQ	<LOQ
SO ₄ ²⁻ [$\mu\text{g}/\text{m}^3$]	2.19	13.26	5.42	3.11	12.61	6.23	2.24	13.26	5.28
PO ₄ ³⁻ [$\mu\text{g}/\text{m}^3$]	1.06	4.05	2.30	1.29	3.20	2.15	1.06	4.05	2.33
Cl ⁻ [$\mu\text{g}/\text{m}^3$]	0.14	11.92	1.14	0.94	9.91	3.28	0.14	11.92	0.72
Carbonaceous compounds									
OC [$\mu\text{g}/\text{m}^3$]	3.6	39.3	11.3	6.4	39.3	18.7	3.6	16.4	7.5
EC [$\mu\text{g}/\text{m}^3$]	1.2	6.9	2.9	2.0	6.9	4.2	1.2	4.2	2.2
TC [$\mu\text{g}/\text{m}^3$]	4.8	46.2	14.2	8.4	46.2	22.9	4.7	20.7	9.7
OC/TC [%]	74.9	85.1	79.6	76.2	85.1	81.7	75.5	79.5	77.2
EC/PM10 [%]	11.1	5.9	8.4	9.5	5.9	7.1	10.8	4.6	7.6
OC/PM10 [%]	33.1	33.7	32.9	30.3	33.7	31.6	33.1	18.0	25.6

Comparing the data to the district of Krakow-Kurdwanow placed 44 km from Wadowice, the average concentration of PM10 between January and October was equalled $32.52 \mu\text{g}/\text{m}^3$. The highest concentration of PM10 in March was also measured there on March 14th and it was equalled $113 \mu\text{g}/\text{m}^3$ while the lowest concentration in August was noted on August 20th ($9 \mu\text{g}/\text{m}^3$) [6].

The highest concentrations of OC and EC ($39.3 \mu\text{g}/\text{m}^3$ and $6.9 \mu\text{g}/\text{m}^3$) were observed in Wadowice on March 13th and March 27th, respectively. For the warmer months in Wadowice (example June 2017) observed concentrations of OC and EC are much lower (OC does not exceed $8.1 \mu\text{g}/\text{m}^3$ whereas EC does not exceed and $2.8 \mu\text{g}/\text{m}^3$). The average concentration of

organic carbon in PM10 was three times higher than the concentration of elemental carbon corresponding to 79.6% in average to the total carbon mass.

Sulphate, nitrate and ammonium are typical secondary ions (secondary inorganic aerosols, SIA). They are made, for example, as a product of aerosol reactions in favorable conditions (e.g. air temperature and humidity) [7]. The concentrations of SIA ranged between: a) SO_4^{2-} 2.19–13.26 $\mu\text{g}/\text{m}^3$, b) NO_3^- 0.40–12.03 $\mu\text{g}/\text{m}^3$ and, c) NH_4^+ 0.25–5.00 $\mu\text{g}/\text{m}^3$. The rest of cations achieved lower results: Mg^{2+} 0.02–1.60 $\mu\text{g}/\text{m}^3$, K^+ 0.33–1.01 $\mu\text{g}/\text{m}^3$, Ca^{2+} 0.02–3.20 $\mu\text{g}/\text{m}^3$, except for Na^+ 1.15 $\mu\text{g}/\text{m}^3$ on September 27th to 4.45 $\mu\text{g}/\text{m}^3$ on April 7th.

Polycyclic aromatic hydrocarbons exhibited similar tendency to PM10. The highest concentrations of examined PAHs were reported on March 9th, 13th and 26th when the sum of analytes concentrations was equal to 146.45 ng/m^3 , 156.72 ng/m^3 , 150.11 ng/m^3 , respectively. In the warmer month much lower concentrations of PAH was detected in the atmosphere. In March it was 84.14 ng/m^3 while in August 10.62 ng/m^3 . The analyses showed 7 times higher concentration of carcinogenic PAHs in March (70.10 ng/m^3) than in August (9.42 ng/m^3). It is worth to notice that although the concentration of PM10 and the PAHs was much lower in the warmer months, the higher amount of carcinogenic PAHs was detected in that mixture.

One of the analyzed PAHs was benzo(a)pyrene. Once more, in March there were significantly higher concentrations of BaP than in August thus in Figure 1 everyday concentrations in March are included while Figure 2 average of several days in August. For instance, the highest concentrations of BaP were detected at March 9th (19.53 ng/m^3), March 13th (19.32 ng/m^3) and March 27th (20.76 ng/m^3) (Fig. 1), while in August, the highest average concentration was recorded in the last week of the month (3.17 ng/m^3) (Fig. 2).

The average concentration of benzo(a)pyrene on March was equal to 11.09 ng/m^3 , whereas on September to 1.45 ng/m^3 (more than 7 times lower than the average on March).

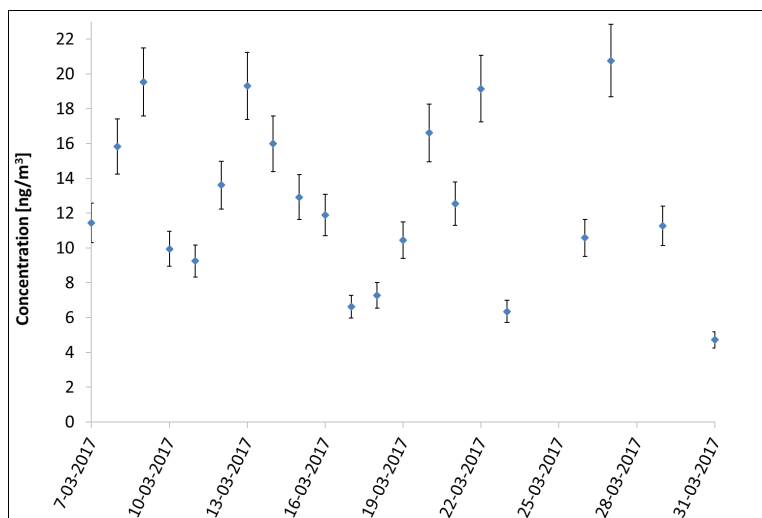


Fig. 1. Concentration of BaP (March)

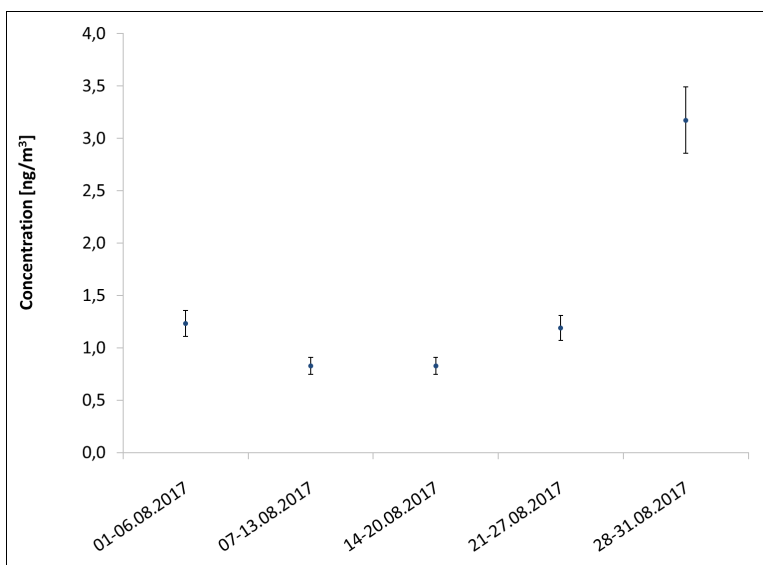


Fig. 2. Concentration of BaP (August)

The relative impact of the PAH mixture on human health can be determined by different types of indicators such as the carcinogenic equivalent (CEQ), mutagenic equivalent (MEQ), and toxic equivalent (TEQ). In this work the results for the sample months – March and August are presented in Table 2. The data from Krakow was also compared to the different cities. To determine the risk coefficients (CEQ, MEQ, TEQ) the authors used the Equations (1)–(3) [8].

Table 2. Mean values of the three risk equivalents: mutagenic (MEQ), carcinogenic (CEQ) and toxic (TEQ) determined from a mixture of PAHs

City and country		MEQ	CEQ	TEQ
		[ng/m ³]		
Wadowice, Poland	March 2017	22.08	72.23	0.09
	August 2017	3.05	11.27	0.01
Delhi, India [9]	Winter 2007	20.07	59.75	0.11
	Summer 2007/2008	7.87	23.09	0.04
Zagreb, Croatia [9]	Winter 2008	4.91	3.64	0.02
	Summer 2007	0.14	0.10	0.00
Florence, Italy [9]	Winter 2009/2010	2.17	5.43	0.01
	Summer 2009/2010	0.54	1.54	0.00
Katowice, Poland [9]	March–June 2012	2.87	4.22	0.51
	June–September 2012	1.91	2.24	0.12

$$\begin{aligned} \text{CEQ} = & 0.001 \times ([\text{Na}] + [\text{Ace}] + [\text{Acy}] + [\text{Flu}] + [\text{Fen}] + [\text{Fl}] + [\text{Pir}]) + \\ & + 0.01 \times ([\text{An}] + [\text{Ch}] + [\text{BghiP}]) + 0.1 \times ([\text{BaA}] + [\text{BbF}] + [\text{BkF}] + [\text{IP}]) + \\ & + 1 \times [\text{BaP}] + 5 \times [\text{DBA}] \end{aligned} \quad (1)$$

$$\begin{aligned} \text{MEQ} = & 0.00056 \times [\text{Acy}] + 0.082 \times [\text{Ch}] + 0.017 \times [\text{Ch}] + 0.25 \times [\text{BbF}] + 0.11 \times [\text{BkF}] + \\ & + 1 \times [\text{BaP}] + 0.31 \times [\text{IP}] + 0.29 \times [\text{DBA}] + 0.19 \times [\text{BghiP}] \end{aligned} \quad (2)$$

$$\begin{aligned} \text{TEQ} = & 0.000025 \times [\text{BaA}] + 0.00020 \times [\text{Ch}] + 0.000354 \times [\text{BaP}] + \\ & + 0.00110 \times [\text{IP}] + 0.00203 \times [\text{DBA}] + 0.00253 \times [\text{BbF}] + 0.00487 \times [\text{BkF}] \end{aligned} \quad (3)$$

4. CONCLUSIONS

The aim of the study was determination of chemical composition of atmospheric aerosols collected in Krakow agglomeration (Wadowice) from January 2017 to October 2017. During that period the increased occurrence of harmful organic compounds (PAHs) especially in colder months (e.g. benzo[a]pyrene) was observed. From the data we can also draw conclusions about presence of the compounds received as a result of coal, fuel and biomass combustion in the winter season. It is important to urgently expand the environmental monitoring strategy. This will allow to get more accurate information on the threat to human health from the presence of air pollutants.

ACKNOWLEDGEMENTS

This work partially financed by AGH UST Rector Grant No. 95/2017 and by the AGH UST statutory tasks No. 16.16.210.476 within subsidy of the Ministry of Science and Higher Education.

REFERENCES

- [1] Szramowiat K., Styszko K., Kistler M., Kasper-Giebl A., Gołas J. Carbonaceous species in atmospheric aerosols from the Krakow area (Malopolska District): Carbonaceous species dry deposition analysis. E3S Web Conf., 2016, vol. 10, pp. 4–11.
- [2] Samek L., Stegowski Z., Styszko K., Furman L., Fiedor J. Seasonal contribution of assessed sources to submicron and fine particulate matter in a Central European urban area. Environmental Pollution, 2018, 241, pp. 406–411.
- [3] Kim K.H., Jahan S.A., Kabir E., Brown R.J.C. A review of airborne polycyclic aromatic hydrocarbons (PAHs) and their human health effects. Environment International, 2013, 60, pp. 71–80.
- [4] Moley S. 'A Network of Trust': Measuring and Monitoring Air Pollution in British Cities, 1912–1960. Environment and History, 2009, 15, pp. 273–302.
- [5] Samek L., Stegowski Z., Furman L., Styszko K., Szramowiat K., Fiedor J. Quantitative Assessment of PM2.5 Sources and Their Seasonal Variation in Krakow. Water, Air and Soil Pollution, 2017, 228, 290, pp. 1–11.
- [6] Dane pomiarowe dla parametru pył zawieszony PM10 2017 r. Wojewódzki Inspektorat Ochrony Środowiska Kraków [online]. Available from: <http://monitoring.krakow.pios.gov.pl/> [accessed: 2018.08.10].

- [7] Styszko K., Samek L., Szramowiat K., Korzeniewska A., Kubisty K., Rakoczy-Lelek R., Kistler M., Kasper-Giebl A. Oxidative potential of PM10 and PM2.5 collected at high air pollution site related to chemical composition: Krakow case study. *Air Quality Atmosphere and Health*, 2017, 10, 9, pp. 1123–1137.
- [8] Kozielska B., Rogula-Kozłowska W., Rogula-Kopiec P., Jureczko I. Wielopierścieniowe węglowodory aromatyczne w różnych frakcjach pyłu zawieszonego w powietrzu obszarów zdominowanych emisją komunikacyjną. *Inżynieria Ekologiczna*, 2016, 49, pp. 25–32.
- [9] Rogula-Kozłowska W., Kozielska B., Rogula-Kopiec P. Road traffic effects in size-segregated ambient particle-bound PAHs. *International Journal of Environmental Research*, 2016, 10, 4, pp. 531–542.

Justyna Sokółowska*, Jarosław Zubrzycki*, Magdalena Marchewka*

THE NUMERICAL METHODS FOR IDENTIFICATION AND ANALYSIS OF ELECTROENCEPHALOGRAPHIC SIGNALS

Abstract

Human body is a living generator of bioelectric signals. One of the most commonly recorded and processed signal is electrical activity of brain. Electroencephalogram is a record of changes in the electromagnetic field. The main field which is dealing with the application of encephalography is the diagnosis of epilepsy. Analysis of the raw EEG signal is difficult for an untrained neurologist so the numerical analysis comes to rescue. The paper presents possibility of using some of the digital signal processing methods. Thanks to them comparison of EEG signal of the healthy person and of the person suffering from epilepsy becomes easier. The research was conducted in Lublin University of Technology. The main tools used are Fourier transformations, wavelet transform and Hilbert–Huang transform. Matlab FFT spectral analysis was used, separately for between-seizure and seizure waveform. Then using Svarog program we obtained time-frequency spectrum. When analyzing wavelet spectrograms, we can obtain information which frequency is dominant, its amplitude and the distribution over time, which allows us to accurately determine when the epileptic attack starts and how long it will last. The methods mentioned can be helpful in creating mathematical algorithms for detecting and identifying irregularities and then to alert medical staff.

Keywords

electroencephalography, numerical methods, wavelet transform, bioelectric signals, medicine

1. INTRODUCTION

Every human is a living generator of various bioelectric signals. Their intensities and mileage vary with activities that are performed each day. Generally speaking, it is electrical energy, which is produced in tissues of living organisms.

* Lublin University of Technology, Mechanical Engineering Faculty, Lublin, Poland;
corresponding author: justyna.sokolowska1@pollub.edu.pl

Through the development of science, people are able to record and process these signals using some methods:

- electrocardiogram (ECG) – heart electrical activity,
- electromyogram (EMG) – record of muscle electrical activity,
- electrooculogram (EOG) – electrical activity of the eye,
- galvanic skin response (GSR),
- electroencephalogram (EEG) – record of brain electrical activity.

One of the most commonly used methods of medical diagnostics is the diagnosis of brain waves with EEG. Measurements of EEG signals consist in recording changes in the electromagnetic field generated by the human brain. In order to perform medical diagnostics of registered EEG signals, detailed analysis of these signals is made using various mathematical methods and using various programs for their processing. Only after obtaining the processed data doctor is able to analyze the state of health of the patient and put the appropriate diagnosis.

Nowadays, electroencephalography is a very important part of brain activity research. Because of its non-invasiveness and lack of contraindications to its implementation in the diagnosis of e.g. epilepsy, vascular cerebral diseases, sleep disorders, as well as those who enter into coma. With the advancement of technology in electronics and computer science, EEG devices are becoming ever better and more accurate. Increasingly, the caps with 64 and even 256 leads. More and more advanced, real-time EEGs are being developed and further analyzed.

Neuro-electrophysiological research, including EEG, plays an important role in the diagnosis of the nervous system diseases. They allow non-invasive assessment of the nervous system by collecting and analyzing bioelectric phenomena. At the same time they are much cheaper and more accessible than imaging. Electrophysiological tests can be repeated, and, therefore, they are used not only in diagnosis, but also in monitoring the course of disease and assessing the efficacy of treatment. The existing analog methods of recording of EEG signals are the basis for making a diagnosis concerning the working of a patient's brain [1, 2]. Unfortunately, it is extremely difficult to analyze and requires a lot of time and vast knowledge and experience of a specialist in the field of EEG. The solution to this problem is changing the form of recording from analog to digital.

Digital EEG is in many ways superior to the traditional form of recording. It allows us to filter and amplify signals after testing – not only during tests. Furthermore, there are computer techniques allowing much better signal analysis from the conventional visual analysis. For this purpose mainly spectral analysis methods are used. They allow the isolation of certain characteristic parameters, which in the case of EEG are the brain waves.

The main field that deals with the application of electroencephalography is the diagnosis of epilepsy. During epileptic seizures characteristic EEG signal components distinguishing pathological signals from signals of a healthy person can be captured [3].

2. DIGITAL IMAGE PROCESSING

One of the most famous computer tools for EEG signal analysis is the Fourier transform. It presents the analyzed signal in the frequency domain. Its main disadvantage is the lack of time-domain information, which is very important for the EEG signal, which is a non-stationary signal. A “rescue” was developed in 1946 by Dennis Gabor, a short-time Fourier transform (STFT). It allows analysis in the time-frequency domain, however, limits the width of the time window. With a narrow window, we get a good time resolution at the low frequency resolution, whereas in the case of a wide window the situation is reversed.

Biomedical signals such as EEG, ECG, EMG or speech are referred to as continuous in, both, time and values [4], and so they are analog signals. To convert them to digital, that is suitable for computer processing, we need A/C processing. The two most important A/C processes are sampling and quantization.

Proper selection of the sampling frequency allows to avoid aliasing. It is about the appearance of incorrect low-frequency components (i.e. aliases) in the spectrum of the processed signal. In practice, in biomedical signal processing oversampling with a frequency of five to ten times is used, as determining the upper limit of the waveform frequency unambiguously is not possible. In EEG recording sampling frequency greater than 200 Hz [5] is recommended.

Another operation leading to the conversion of the analog signal into a digital signal is quantization of a sampled signal. Quantization is conversion of a discrete (formerly sampled) analog signal into a discrete number of digital values (with a finite number of levels) [6, 7]. The process of quantization leads to an inevitable loss of part of the information. The inaccuracy of this process results in an error characterized with random noise. The basic operations that process analog signals to digital ones are shown in Figure 1.

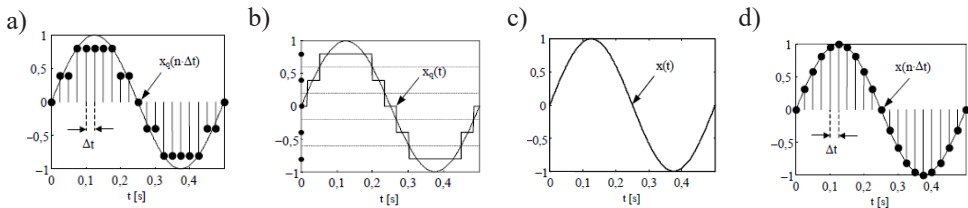


Fig. 1. Graphic example of discretization of signals: a) continuous signal, b) sampled signal, c) quantized signal (discrete in values), d) sampled and quantized signal (digital) [6, 8, 9]

3. TYPES OF BRAIN WAVES

Brain waves are specific electrical impulses generated by the brain. They were discovered in 1929. A German psychiatrist, Hans Berger, is acknowledged as their discoverer. Depending on the state of consciousness and a person’s age, the frequency of these waves changes. 5 basic types of waves can be enumerated in terms of the frequency: alpha, beta, theta, delta and gamma [10]. Each of them is responsible for different brain activity. The alpha rhythm is the

main basic rhythm of the proper EEG of an adult. The alpha rhythm is a rhythmic frequency between 8 and 13 Hz, which usually takes the largest amplitude in the vicinity of the occipital areas which are part of the cortex responsible for processing visual information. The beta waves have a frequency of 12 to 30 Hz. They are purely rhythmic and give background in the recording of the majority of people.

If they are completely absent, there may be pathology depending on other features of EEG. They are split into: Low Beta Waves (12–15 Hz), Beta Waves – the average frequency (15–18 Hz) and High Beta Waves (above 19 Hz). Theta waves are in the 3–7 Hz frequency. Their range is a few tens of microvolts. They are most prominent for the lead of the center line and temporal leads. They occur during light sleep, meditation, hypnosis, trance, intense dreams, as well as intense emotions. Another type of theta activity is associated with cognitive activity, associating and memory processes [10, 11]. Delta waves have a frequency of 0–4 Hz. They are very slow – lasting at least 0.25 s, while also having high voltage amplitude. During deep sleep they take the form of slow waves, then their amplitude does not exceed 75 μ V. Delta waves also occur during being awake in the elderly or children. They are also determinant of some pathological changes in the brain [10, 11]. Basic gamma waves have frequencies from 30 to 80 Hz. In contrast, the waves of the frequency of 80–200 Hz are referred to as high-frequency gamma. This rhythm is associated with physical activity, motor functions and higher cognitive processes. High-gamma activity occurs during activation of the cortex by external and internal stimuli [1, 3, 10, 11].

4. RESEARCH STAND

The research was conducted in the laboratory of the Center of Innovation and Advanced Technology of the Lublin University of Technology. The study used an EEG Electrical Geodesics Company, Inc. with Net Station 5 EEG software. EEG tests were made using a HydroCel Geodesics Sensor Net grid with 32 active electrodes distributed according to the 10–20 system.

5. TESTING GROUP

In order to analyze the detection of changes occurring in the states of illness, the author decided to present the EEG signal of the person suffering from epilepsy and compare it with the EEG signal of the healthy person. The course of patients with epilepsy was obtained from outpatient clinical trials. Five EEG records of female patients aged 7–15 years with clinically epilepsy were used.

A very serious disease in epileptic patients is the so-called Status epileptic. According to the definition of Epilepsy Foundation of America, epilepsy is a syndrome of continuous seizure activity that persists for about 30 minutes. Or where two or more seizures are observed between which the patient is unconscious [9].

The consequence of epilepsy is a significant systemic disorder. Frequent bioelectric discharges lead to changes in the nervous system but also in the respiratory, cardiovascular and endocrine systems [9].

Not every seizure is spontaneous and repetitive, so it is assumed that at least two unprovoked attacks within 24 hours are the basis for the diagnosis of epilepsy.

Essential in the proper diagnosis of epilepsy is to gather intelligence from the patient himself, but also from witnesses to the event.

In the diagnosis of epilepsy, it is very useful to study EEG. Through it we can in a non-invasive way to track the bioelectric activity of the brain. With the EEG we can not only recognize epilepsy, but also locate epileptic seizures, evaluate epileptic seizures, and recognize epilepsy. It is worth remembering that the incidence of epilepsy in EEG does not always indicate epilepsy. The result should be interpreted with medical history.

6. NUMERICAL TOOLS USED FOR THE IDENTIFICATION AND ANALYSIS OF EEG SIGNALS

The main analytical tools used in the numerical analysis of EEG are the following transformations: Fourier transform, discrete Fourier transform DFT, FFT fast Fourier transform, short-time Fourier transform STFT, wavelet transform, and Hilbert–Huang transform. These tools have been implemented in MATLAB software. They can be found in the Signal Processing module and dedicated toolbox for EEGLAB signal analysis [12, 13].

In this paper the EEGLAB package was used to analyze the EEG of a person suffering from epilepsy [12, 13]. Data for the analysis came from an EEG digital camera recorded in the medical data exchange format. After importing the measurement data to the program, the following record of individual rhythms was obtained (Figs. 2–4).

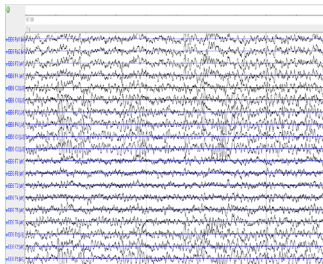


Fig. 2. EEG signal of a healthy person (21 years old woman)

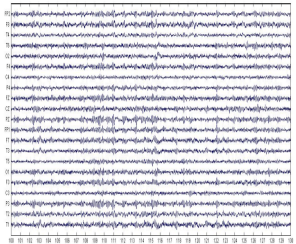


Fig. 3. EEG test result: 30 s between-seizure waveform

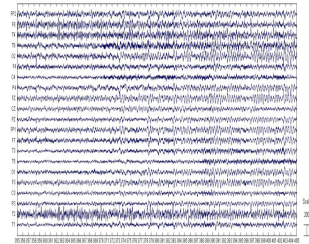


Fig. 4. EEG test result: 50 s during epileptic seizures

Analyzing the above waveforms, it can be seen high activity of alpha waves, and thus the basis for the correct rhythm EEG. This is related to the state of relaxation and closing of eyes, alpha rhythm is, because then the most noticeable. The greatest activity of this rhythm can be seen in the vicinity of leads C3, C4, P3, P4, O1, O2, i.e. at the frontal and parietal frontal and in the occipital lobe. These waveforms are characterized by the absence of any discharging units' characteristic for e.g. the epileptic attack. It is worth noting that the raw EEG record

very often does not give a clear answer about the occurrence of lesions. EEG recording should be interpreted in combination in the presence of symptoms or in combination with imaging. The Figure 5 shows the EEG course during the epileptic attack.

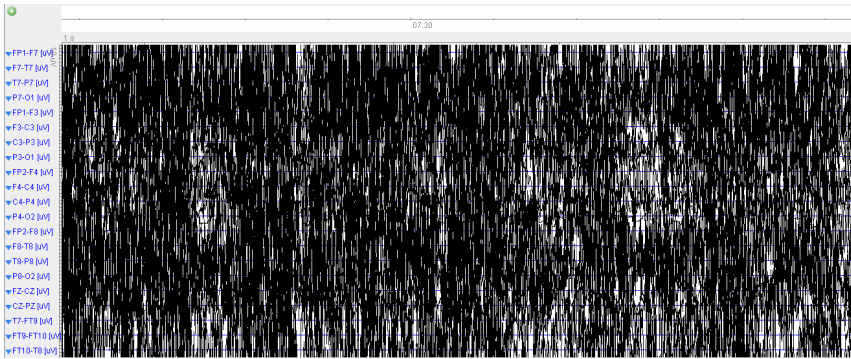


Fig. 5. Record of EEG signal during epileptic seizure in 11 years old female

As the EEG signal is a non-stationary signal, a time-frequency transform is a helpful tool for analyzing it.

Next, numerical integration of signals from individual electrodes was carried out (Fig. 6).

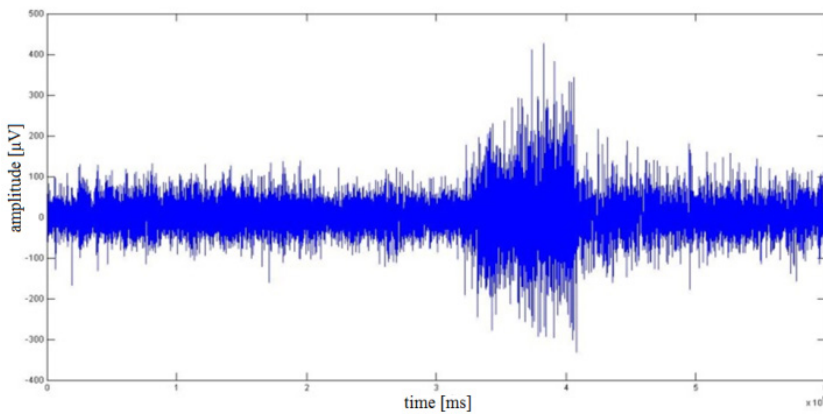


Fig. 6. The summary signal from all the electrodes

The next step was to perform signal analysis using FFT spectral analysis. This method has shown the contribution of individual frequencies in the waveform during a seizure. By analyzing the power spectrum (Fig. 7), it was observed that in the waveform delta waves and alpha waves constitute a large share, which indicates that the study was conducted with closed eyes. What is more, there is a big chance that it was during sleep. A considerable decrease in theta can be seen.

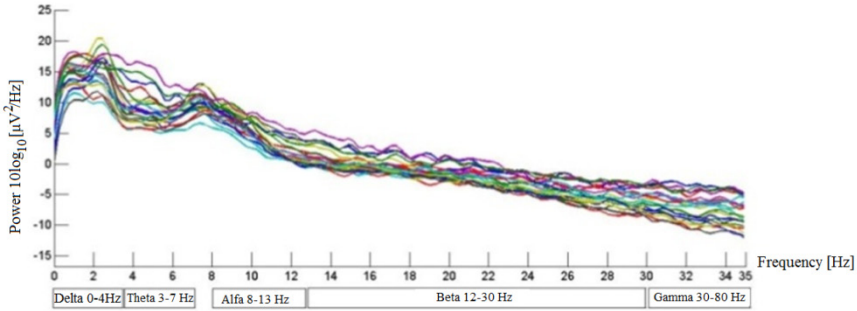


Fig. 7. The power spectrum of the EEG signal

Classic FFT analysis was performed separately for the between-seizure waveform (Fig. 8a), and separately for the waveform during epileptic seizure (Fig. 8b). In between-seizure waveform the frequency distribution is similar to previously analyzed power spectrum of the whole signal – typical frequencies for delta and alpha rhythms are dominant. In the epileptic seizure waveform a clear increase in the amplitude in the range of 2–5 Hz can be seen, which probably is the result of the occurrence of epileptiform discharges.

The fragment selected for analysis included 600 seconds portion of the EEG recording. After about 300 seconds a seizure lasting a few tens of seconds begins, which is reflected in the changes in the EEG signal. Clinical manifestations of the seizure were found in the 232 second, while changes in the EEG signal started in the 341 second of the record and finished in the 416 second.

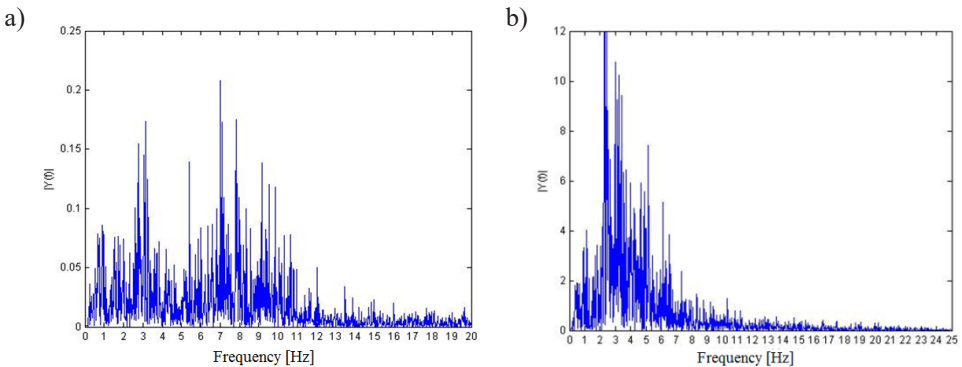


Fig. 8. FFT analysis of the signal from the T4 electrode: a) an analysis of the first 50s of signal, b) signal analysis in a time window of 355–405 s – during seizures

In Figures 3 and 4 the selected fragments of the signal generated using the eegplot function of EEGLAB program. Based on visual analysis differences between the between-seizure waveform and during the seizure waveform can be given. The greatest amplitude of the signal was recorded from about 320 to 410 seconds of the test. The total amplitude of all channels

is several times higher than during the remaining period of time. It is a characteristic feature of a seizure waveform. In the waveform sharp waves characteristic of epileptic seizure with a maximum amplitude of about 250 μV can be distinguished.

The record of Figure 5 depicting epileptic seizures completely makes it impossible to analyze. This is probably due to the occurrence of very high frequency bands and the amplitude of the discharges. Information about both frequencies and amplitudes can be obtained by analyzing spectrograms obtained using the time-frequency method. For the analysis of these studies used wavelet transform.

For wavelet analysis was used Svarog program with the finished module Wavelet Transform. Both the group of healthy people and groups of people with epilepsy used Morlet Wave. The choice of the wavelet was mainly due to the limitations of the program, which in its package allows the use of three waves: Haara, Shannon and Morlet. Falka Haara Wavelet is mainly used to construct the Daubechies, while Shannon's Wavelet is often used for theoretical considerations, so it is decided to use the Morlet Wavelet. To correctly analyze time-frequency spectrum, you need to know what the individual axes and colours and brightness are. The vertical axis corresponds to the frequency values, while the horizontal axis determines the time. Colours (orange) and brightness (bright blue) indicate the level of activity in a given frequency range. The wavelet spectrogram of a healthy female at the age of 22 is shown in the Figure 9. Light blue peaks in the range of 8 to 12 Hz, as seen in the figure, indicate the resting activity of the brain. The signal amplitude was about 20 μV . The orange colour on the spectrogram may mean the appearance of artefacts associated with, for example, the movements of the tongue, whose amplitude is similar to that in the graph of about 100 μV .

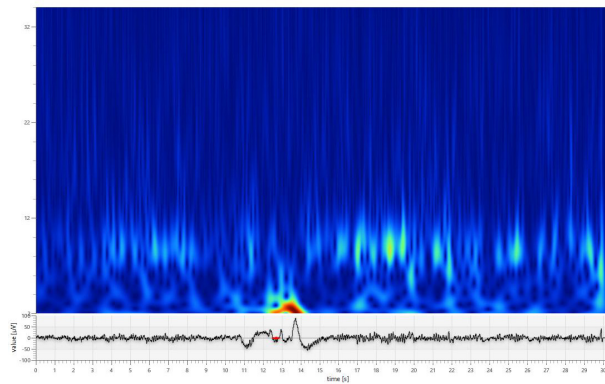


Fig. 9. Wavelet spectrogram of healthy woman (age 22 years old)

Wavelet analysis for the studies in Figure 5 is presented below. The test person was clinically diagnosed epilepsy, and the study shows the same seizure.

On the spectrogram (Fig. 10), the first 44 seconds of the epileptic attack were shown. We can see an increased brain activity in the time interval of 26 to 37 seconds (orange) and a frequency of 2–4 Hz. The amplitude of these peaks is slightly above 250 μV . The light blue colour is marked by a weaker brain activity of 8 Hz.

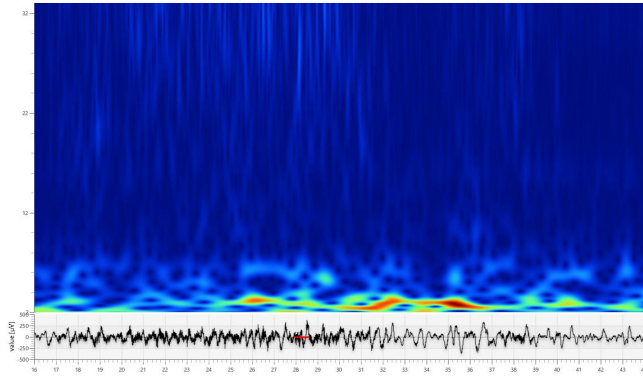


Fig. 10. Wavelet spectrogram of 11 years old girl with epilepsy

Further analysis gives further results with even more intense epileptic discharges (Fig. 11).

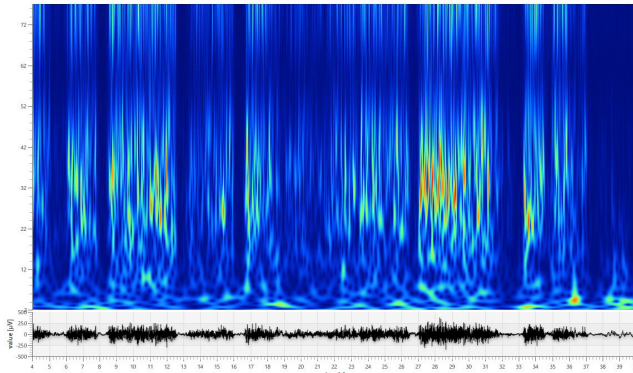


Fig. 11. Wavelet spectrogram of 11 years old girl with epilepsy (further research)

Peaks marked in orange and light blue in full frequency range are clearly visible. The greatest activity is observed in the range of 22–42 Hz. By analyzing the horizontal axis, it can be seen that the duration of individual epileptic seizures was approximately 2–4 seconds and their amplitude was 250 μV .

7. CONCLUSIONS

EEG examination is a very common test due to its wide application in neurology and a relatively low price. Its process of conversion is also much easier and faster than in the case of data from imaging studies. With the digital signal processing methods mathematical algorithms for detecting and identifying irregularities can be created. The program can be programmed to alert medical staff. This allows to speed up the analysis of long-term EEG. 24-hour recording registrations and videometria – simultaneous EEG recording and video

recording of the patient using a video camera [14] – are becoming increasingly popular. With the 24-hour recording the detection of seizures increased to 1.5–3 times compared to the routine, short EEG [15].

Identification and unambiguous identification of specific patterns of brain bioelectrical activity as phenomena indicating seizures is one of the main problems in assessing the results of EEG, and, therefore, attempts to facilitate this identification should be made. The other methods listed in the paper – wavelet transform, Wigner–Ville transform, Hilbert–Huang transform – are also noteworthy. They are characterized by better results in the localization of signals in the domain of time and frequency than the before mentioned Fourier transform. The Hilbert–Huang transform, is particularly noteworthy, being a relatively new discovery, and it is still developing in the field of non-stationary and non-linear signal analysis, which is precisely what the EEG signal is.

Both the EEG waveform plot and the waveform generated after waveform transformation were generated in Svarog. With the built-in Wavelet Transform module, it is a very powerful and fast wavelet analysis tool. By observing the EEG course of people with epilepsy, it is easy to see that during epileptic seizures the electroencephalogram is very distorted and can be said to be unreadable. When analyzing wavelet spectrograms, we can obtain information not only on the frequency of each frequency and the amplitude but also on its distribution over time. In patients with epilepsy, this allows you to accurately determine when the epileptic attack starts and how long it will last.

REFERENCES

- [1] Abou-Khalil B., Misulis K.E. Atlas EEG i semiologii napadów padaczkowych. Elsevier Urban & Partner, Wrocław 2010.
- [2] Augustyniak P. Przetwarzanie sygnałów elektrodiagnostycznych. AGH Uczelniane Wydawnictwa Naukowo-Dydaktyczne, Kraków 2001.
- [3] Bajaj V., Pachori R.B. Separation of Rhythms of EEG Signals Based on Hilbert–Huang Transformation with Application to Seizure Detection. School of Engineering, Indian Institute of Technology Indore, Indore, India 2012.
- [4] Kuniszyk-Józkowiak W. Przetwarzanie sygnałów biomedycznych. Uniwersytet Marii Curie-Skłodowskiej, Wydział Matematyki, Fizyki i Informatyki, Lublin 2011.
- [5] Huang N.E., Shen S. The Hilbert–Huang transform and its applications. World Scientific Publishing Co Pte Ltd Singapore 2014.
- [6] Kołodziej M. Przetwarzanie, analiza i klasyfikacja sygnału EEG na użytek interfejsu mózg-komputer [PhD thesis]. Politechnika Warszawska, Warszawa 2011.
- [7] Vergult A., De Clercq Q., Palmi A., Vanrumste B., Dupont P., Van Huffel S., Van Paesschen W. Improving the Interpretation of Ictal Scalp EEG: BSS-CCA Algorithm for Muscle Artifact Removal. *Epilepsia*, 2007, 48, 5, pp. 950–958.
- [8] Oppenheim A.V., Schaffer R.W. Cyfrowe przetwarzanie sygnałów. Wydawnictwa Komunikacji i Łączności, Warszawa 1979.
- [9] Zieliński T. Cyfrowe przetwarzanie sygnałów. Od teorii do zastosowań. Wydawnictwa Komunikacji i Łączności, Warszawa 2005.

- [10] Durka P., Duszyk A., Kamiński M., Kuś R., Malinowska U., Mikuła I., Suffczyński P., Żygierewicz J. Elektryczny ślad myśli [on-line]. Available from: <http://brain.fuw.edu.pl/edu/EEG> [accessed: 16.08.2018].
- [11] Rowan A.J., Tolunsky E. Podstawy EEG z miniatlasem. Elsevier Urban & Partner, Wrocław 2004.
- [12] Delorme A., Serby H., Makeig S. The EEGLAB Tutorial [on-line]. Available from: <http://sccn.ucsd.edu/eeglab/eeglabtut.html> [accessed: 20.06.2018].
- [13] Sanei S., Chambers J.A. EEG Signal Processing. John Wiley & Sons Ltd, 2007.
- [14] Koszewicz M. Znaczenie badań elektrofizjologicznych w diagnostyce schorzeń ośrodkowego i obwodowego układu nerwowego. Polski Przegląd Neurologiczny, 2008, 4, 4, pp. 174–180.
- [15] Mazur R., Kozubski W., Prusiński A. Podstawy kliniczne neurologii dla studentów medycyny. Wydawnictwo Lekarskie PZWL, Warszawa 1999.

Magdalena Kopernik*, Paweł Tokarczyk*

DEVELOPMENT OF MESOSCALE MODEL OF BLOOD THROMBOSIS

Abstract

Blood coagulation at the place of complete severing of a vessel or puncturing of a vessel sidewall is usually a beneficial reaction, by protecting the body from bleeding and maintaining hemostasis, while the formation of a blood clot inside the blood vessel is a pathological phenomenon, highly dangerous, sometimes leading to serious complications. In this work an attempt will be made to develop a model that in the future will predict the formation of blood clots in the mesoscale in small blood vessels. The following tasks were performed due to reach the goal of the paper: 1. Simulations were carried out using the blood vessel model with different degrees of stenosis in 2D and 3D to determine: the optimal densities of FVM (finite volume method) grid and the effect of stenosis on blood flow velocity and shear stress. 2. Numerical tests were carried out for two types of flow: laminar and turbulent to show the differences in flow in blood vessel models with stenosis. Stenosis is considered as a result of thrombosis and degrees of stenosis are based on literature research. Concluding, the goal of the present paper is to develop the model with stenosis to simulate flow in blood vessels.

Keywords

non-newtonian blood rheology model, blood thrombosis, stenosis, computational fluid dynamics, mesoscale model, laminar flow, turbulent flow

1. INTRODUCTION

Blood coagulation at the place of complete severing of a vessel or puncturing of a vessel sidewall is usually a beneficial reaction, by protecting the body from bleeding and maintaining hemostasis, while the formation of a blood clot inside the vessel is a pathological phenomenon, highly dangerous, sometimes leading to serious complications. The difference in the composition of the clot can be seen in the veins and arteries. In the veins, where blood

* AGH University of Science and Technology, Faculty of Metals Engineering and Industrial Computer Science, Krakow, Poland;
corresponding author: kopernik@agh.edu.pl

flow is slow, the clot consists of fibrin gel (and red blood cells). With fast flow in the arteries it consists mainly of platelets. In the present paper will be analysed the scenario with flow caused by stenosis which is a result of blood thrombosis.

In literature [1] is shown the basic physiological behaviour of stenosis. The pressure loss across a stenosis not only depends on the severity of narrowing, but to a large extent on the magnitude of flow that goes through the artery. This pressure loss is due to viscous friction losses across the throat of the lesion, and separation losses that occur through acceleration of flow through the stenosis and the formation of eddies at the stenosis exit. Due to the combination of these effects, the pressure loss incurred by a stenosis increases quadratically with an increase in flow. The clot formed in the wall of the vessel leads to stenosis [2], which changes the characteristics of blood flow. In the present paper stenosis is considered as a result of thrombosis.

The coagulation mechanism is very complex, it contains about 30 different substances that are subjected to many reactions [3]. Thrombus formation is the result of two mutually linked processes – platelet interaction and activation of the coagulation pathway. Immediately after damage to the vessels, the platelets adhere to the vascular lesion, forming a single cellular layer. Then, the shallows stick together and form cell aggregates. Thus, modelling of blood coagulation in literature is carried out in three scales: a) a mesoscale – haemodynamics and kinetics of chemical reactions of blood coagulation, b) a micro scale – interaction of platelets with the vessel wall, leucocytes and other cellular blood components, and c) a nanoscale – precipitation of fibrin [4]. In the present paper the first part of the mesoscale approach will be studied.

Many works in the literature concern the modeling of various cases of stenosis, while there are only a few works in the field of experimental measurements, and even fewer works that include model and experimental parts. The authors of the article are trying to simulate micro-fluidic systems, hence they chose medium-diameter vessels with the most common stenosis as an object of interest, to test the possibilities of modeling such systems, and then go to a lower scale to take into account the phenomena that appear there.

The one of approaches presented in literature to modelling the blood thrombosis in meso scale considers blood as a two-component fibrous medium [5] in which the radius of fibrin fibers is much smaller than the size of single platelet. These works are used to model the thrombus-flow interaction applying the permeability of a porous medium calculated from Darcy's law and the media is described using the higher-order Brinkman equation in the Navier–Stokes equations [6, 7].

In this work an attempt will be made to develop a blood flow model that in the future will be also applied to predict the formation of blood clots in the mesoscale in blood vessels. The following tasks were performed due to reach the goal of the paper: 1. Simulations were carried out using the blood vessel model with different degrees of stenosis in 2D and 3D to determine: the optimal densities of FVM grid and the effect of stenosis on blood flow velocity and shear stress in blood vessel model 2. Numerical tests were carried out for two types of flow: laminar and turbulent to show the differences in flow in blood vessel models with stenosis. The different degrees of stenosis and shapes of blood vessels were based on literature research [8, 9].

2. BLOOD VESSEL MODEL WITH STENOSIS UNDER LAMINAR AND TURBULENT FLOW

In order to build a model of a blood vessel with stenosis, 2D and 3D solid models were made, to which the shapes of blood vessels and the degrees of their stenoses were prepared on the basis of publications [8, 9]. The non-newtonian power law blood model was used to carry out the simulations under laminar flow. For stenotic arteries velocity fields are influenced by blood rheology [10]. Thus, the non-newtonian behaviour of blood should be considered in the blood vessel model. The general power law has the form presented in [11]:

$$\eta = k\bar{\dot{\gamma}}^{n-1} \quad (1)$$

where:

- k – consistency coefficient ($\text{Pa}\cdot\text{s}^n$) [12],
- n – power term, flow behaviour index,
- $\bar{\dot{\gamma}}$ – shear rate.

The coefficient k represents consistency of a fluid. The larger the consistency is, the more viscous is a fluid. The coefficient n is a measure of a non-newtonian behaviour, $n = 0$ represents Newtonian fluid. The closer to one this coefficient is, the more non-newtonian are the properties of a blood. Liquids with $n > 0$ show hardening by shearing. A blood with $n < 0$ represents softening by shearing. Typical values of the coefficient in Equation (1) for the healthy human blood and for the body temperature of 37°C are [11]: $k = 0.134 \text{ Pa}\cdot\text{s}^{-1}$ and $n = 0.785$. Several extended modifications of the power law can be found in the literature.

Shear stress plays crucial role in platelets activation. According to the paper [13] exposure to shear stresses above 20 Pa caused significant changes in all three of the platelet markers. Thus, shear stress values are important parameters of thrombosis process and will be analysed in the present paper.

The turbulence intensity TI is used for computational fluid dynamics simulations in the present paper as a boundary condition and it is a function of the Reynolds number Re . The scaling on the axis of a pipe provides to power law expression as [14]:

$$TI = \frac{v_{RMS, pipeaxis}}{v_{pipeaxis}} = a \cdot Re^b = 0.16 \cdot Re^{-\frac{1}{8}} \quad (2)$$

where:

- $v_{RMS, pipeaxis}$ – local RMS (root mean square) of the turbulent stream wise velocity fluctuations,
- $v_{pipeaxis}$ – local mean stream wise flow velocity,
- a and b – fit parameters.

The k - ε model [15] is an example of one of the most popular turbulence models and will be used in the present paper. In the turbulence model k - ε , k stands for the turbulence kinetic energy:

$$k = \frac{1}{2} \overline{u_i u_i} \quad (3)$$

where:

u_i – a fluctuating component of velocity in the direction x_i ,
 ε – a rate of dissipation of turbulence energy.

ε is defined by:

$$\varepsilon = \nu \overline{\frac{\partial u_i}{\partial x_k} \frac{\partial u_i}{\partial x_k}} \quad (4)$$

where: ν is the kinematic viscosity of the fluid.

Using this turbulence model other parameters can be determined: W which represents the time-average square of the vorticity fluctuations and l which represents length of macroscale turbulence. This model is valid only for turbulent flows. Close to walls there are regions where the local Reynolds number of turbulence is so small that viscous effects predominate over turbulent ones. There are two methods of accounting for these regions in numerical methods for computing turbulent flow: the wall-function-method and the low-Reynolds number-modelling method. In the present paper the first method has been applied.

2.1. 2D BLOOD VESSEL MODEL WITH STENOSES 0–70% UNDER LAMINAR FLOW

2D blood flow tests for a blood vessel were performed for stenoses: 0, 30, 50, 60 and 70% under laminar flow. The model of blood vessel had a length of 90 mm and a section diameter of inlet is 3.5 mm [8]. Solid models were made in the Solid Works program. Simulations were carried out in the Ansys program – the Fluent module. The simulations were carried out on FVM grids with the number of elements equal to 49,000 and the number of nodes equal to 50,000. The densities of the FVM grid at the location of stenosis are shown in Figure 1. The regions of local grid densities were marked using circles which are visible at the location of stenosis.

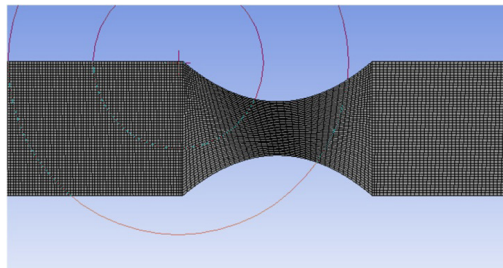


Fig. 1. The density of FVM grid in stenosis zone of the 2D blood vessel model

The parameters of the power law applied in the present paper are: $n = 0.785$ and $k = 0.134 \text{ Pa}\cdot\text{s}^{-1}$ [11]. The other parameters used in simulations are: flow rate $- 1 \text{ mL}\cdot\text{s}^{-1}$, blood density $1065 \text{ kg}\cdot\text{m}^{-3}$ [8] and blood viscosity $0.004 \text{ kg}\cdot\text{m}^{-1}\cdot\text{s}^{-1}$ [8]. For blood flow velocity, the range of values on the scale in Figure 2 is set to the maximum value of blood velocity obtained for the 3D model with a 60% stenosis under the laminar flow, so the differences in distributions of blood flow velocity for individual models can be easily visible.

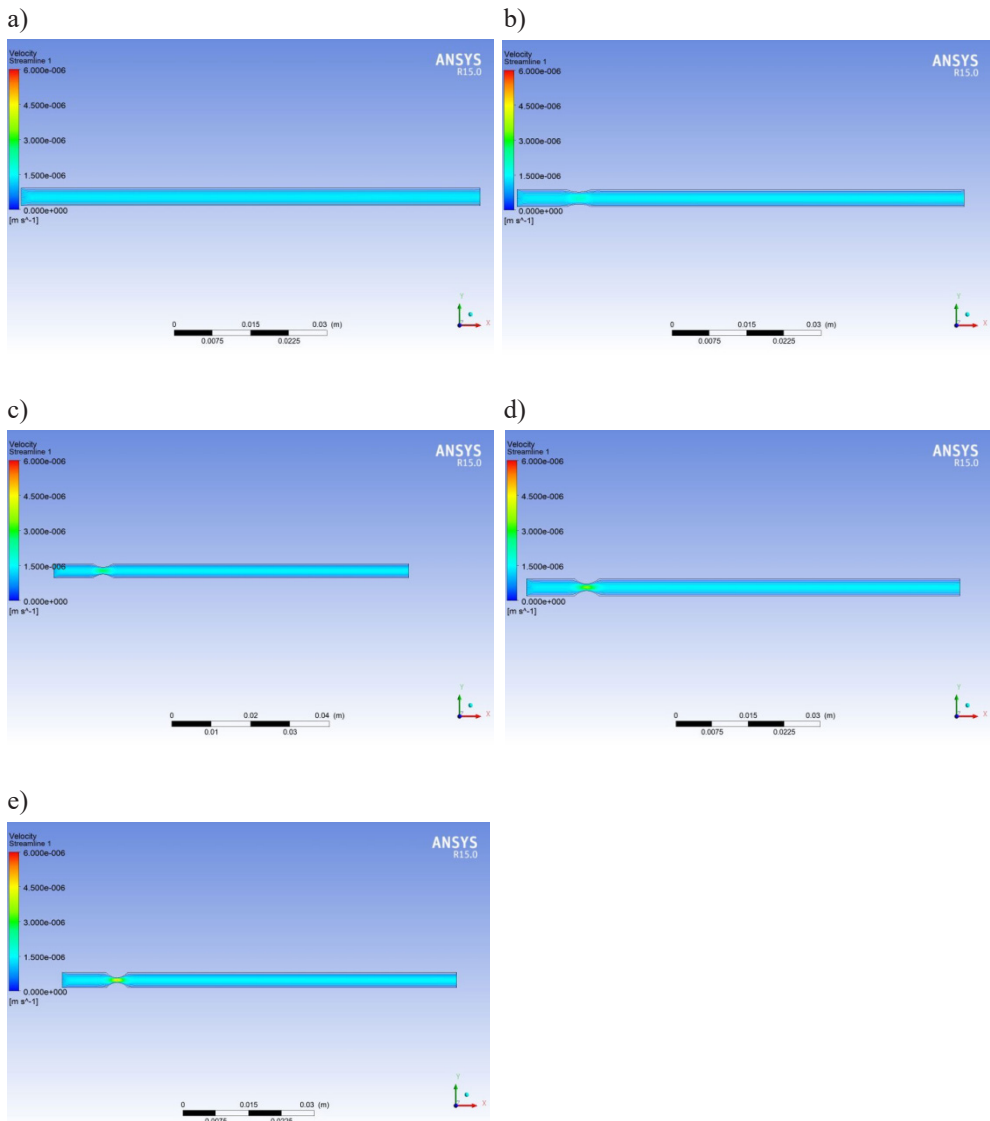


Fig. 2. Distribution of flow velocities in the 2D model of blood vessel with stenoses of: a) 0%, b) 30%, c) 50%, d) 60% and e) 70% under laminar flow

On the basis of results reach in simulations, the maximum values of flow velocities can be determined in a model of a blood vessel which is $1.4 \mu\text{m}\cdot\text{s}^{-1}$ for a vessel without stenosis, $1.9 \mu\text{m}\cdot\text{s}^{-1}$ for stenosis 30%, $2.8 \mu\text{m}\cdot\text{s}^{-1}$ for stenosis 50%, $3.6 \mu\text{m}\cdot\text{s}^{-1}$ for 60% stenosis and $4.9 \mu\text{m}\cdot\text{s}^{-1}$ for 70% stenosis. The greater the degree of stenosis, the greater the biggest value of blood flow velocity in the stenosis region in Figure 2. The distribution of flow velocity for the blood vessel model without stenosis shows a uniform character, the values of flow velocities near the wall are the smallest. The distribution of flow velocity for vessel model with stenosis 30, 50, 60 and 70% shows increasing values of flow velocities in the region of stenosis, and gradients of velocity are the biggest for the biggest degree of stenosis. The distribution of velocity in the area outside the stenosis remains homogeneous.

2.2. 3D BLOOD VESSEL MODEL WITH STENOSIS 60% UNDER LAMINAR FLOW

3D blood flow tests were performed for a blood vessel model with stenosis 60%. The 3D solid model was prepared in the Solid Works program by rotating the 2D model presented in Section 2.1. Simulations were carried out in the Ansys program – the Fluent module. The simulations were carried out on FVM grids with the number of elements equal to 8700 and the number of nodes equal to 10,000. The density of the FVM grid of the 3D blood vessel model with stenosis 60% is shown in Figure 3. The parameters set for the 3D blood vessel model with stenosis 60% and boundary conditions applied in simulations are the same as in the Section 2.1.

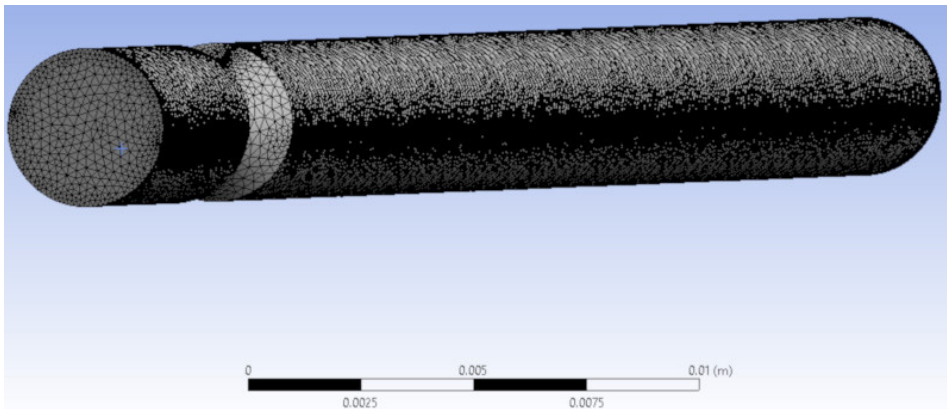


Fig. 3. The density of FVM grid of the 3D blood vessel model

The distribution of velocity in the cross-section of the 3D blood vessel model with stenosis 60% is shown in Figure 4. The maximum velocity calculated for the 3D model is $5.8 \mu\text{m}\cdot\text{s}^{-1}$ which is about 1.5 times bigger value than the maximum velocity computed for the 2D model. The distribution of flow velocity for the 2D and 3D model is similar, the maximum velocities occur in the stenosis zone and the gradients of velocity are also the biggest in this region. Outside the stenosis region the distribution of velocity is homogeneous.

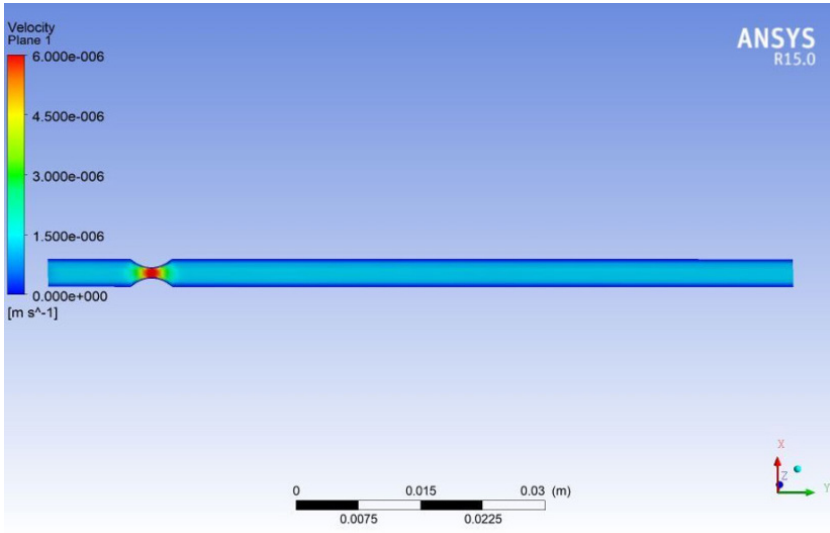


Fig. 4. Distribution of flow velocity in the blood vessel with stenosis 60% for cross-section of 3D model

2.3. 2D BLOOD VESSEL MODEL WITH STENOSIS 60% UNDER TURBULENT FLOW

Simulations for the 2D blood vessel model with stenosis 60% were carried out on FVM grids with the number of elements equal to 49,000 and the number of nodes equal to 50,000. The $k-\epsilon$ turbulent model was used in simulations with the following parameters: $Re = 25.6$, turbulent intensity = 10.6682%; and flow rates $1 \text{ mL}\cdot\text{s}^{-1}$ and $1 \text{ m}\cdot\text{s}^{-1}$. The results showing the distributions of velocities for two flow rates are presented in Figure 5.

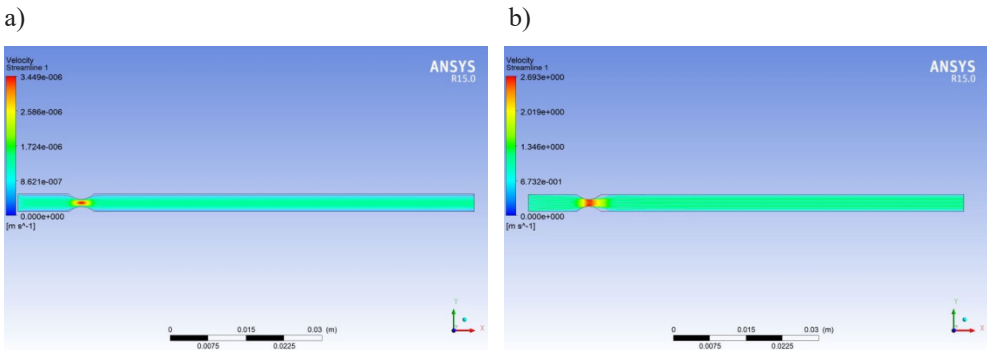


Fig. 5. Distributions of flow velocities in the 2D blood vessel model with stenosis 60% under turbulent flow for: a) $1 \text{ mL}\cdot\text{s}^{-1}$ and b) $1 \text{ m}\cdot\text{s}^{-1}$

Analysis of flow velocity distributions shows significant differences between models with small and big values of flow rates. In the zone after the stenosis, the blood does not reach

the vessel wall in the model for which the biggest flow velocity was applied. The same character of fluid flow after stenosis was observed in the experiment in paper [16] for similar Re .

The results of maximum shear stresses reached for all blood vessel models under laminar and turbulent flow are shown in Figure 6, and these maximum values are smaller than critical values of shear stress which are dangerous for platelets [13]. The increase in the degree of stenosis increases the shear stress in the 2D models of blood vessels under laminar flow. For the 2D blood vessel model with stenosis 60%, the maximum shear stress is smaller than for the 3D model with the same stenosis. The maximum shear stress for the 2D model under turbulent flow for stenosis 60% is similar to the maximum shear stress for the 2D model with stenosis 50% under laminar flow. However, the maximum shear stress for the 2D model with stenosis 60% is bigger than the maximum shear stress for the 2D model with stenosis 60% under turbulent flow.

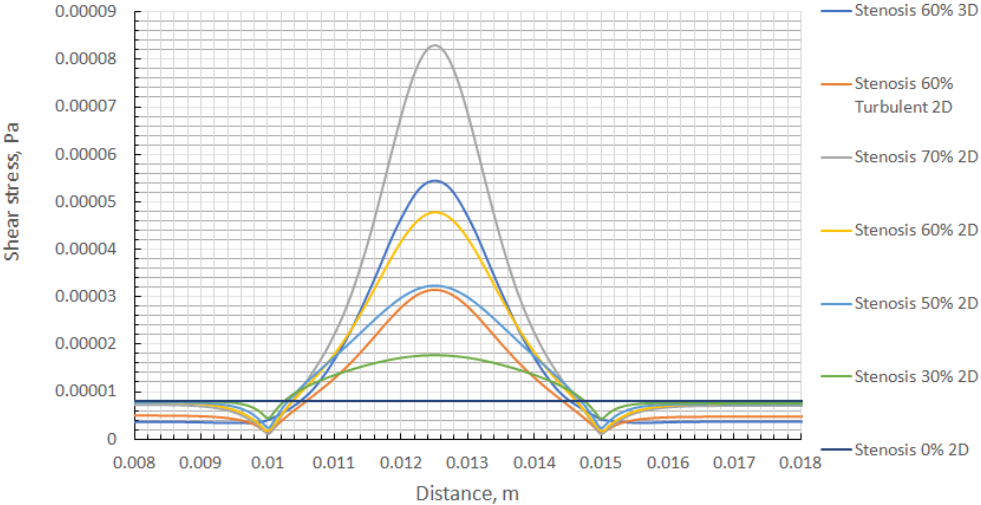


Fig. 6. Summary chart of shear stress in the 2D blood vessel models with stenoses 0–70% under laminar flow, in the 2D blood vessel model with stenosis 60% under turbulent flow and in the 3D blood vessel model with stenosis 60% under laminar flow

The results of maximum velocity reached for all blood vessel models under laminar and turbulent flow are shown in Figure 7 as blood velocity profiles. Velocity profiles are made for measuring points located on the entire width of the blood vessel model in the stenosis zone. The bigger the degree of stenosis, the bigger the flow velocity is observed. Almost all values of blood velocities have been commented in the previous sections. The maximum blood velocity for the 2D model with stenosis 60% under laminar flow is bigger than the maximum blood velocity for the 2D model with stenosis 60% under turbulent flow, what has been investigated in the present section.

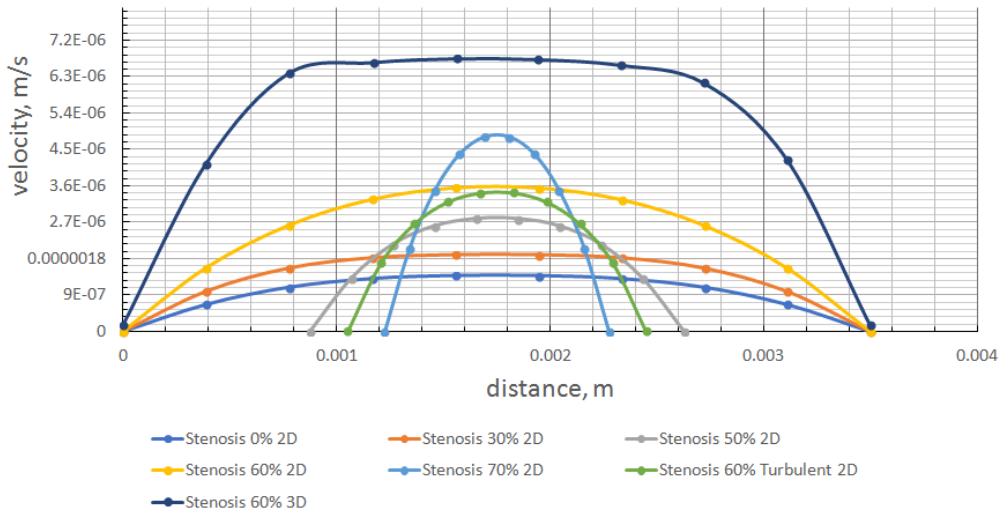


Fig. 7. Summary chart of blood velocity in the 2D blood vessel models with stenoses 0–70% under laminar flow, in the 2D blood vessel model with stenosis 60% under turbulent flow and in the 3D blood vessel model with stenosis 60% under laminar flow

3. CONCLUSIONS

Stenosis resulting from the formation of a blood clot in small vessels affects on:

- an increase in the flow velocity and shear stress within the stenosis of blood vessel model, the bigger the degree of stenosis, the bigger the flow velocity and shear stress in this zone;
- differences in the 2D and 3D blood vessel models, especially affects on the maximum values of shear stress and velocities; in the 2D model are observed smaller values of flow velocities and shear stresses in the stenosis zone in comparison with the 3D model.

Other observations made for the 2D blood vessel models with stenosis 60% under two types of flow are presented below:

- the 2D blood vessel model with 60% stenosis under turbulent flow for big blood flow velocity shows different character of velocity distributions in comparison with the 2D blood vessel model with the same degree of stenosis for which the blood flow velocity is small;
- the maximum shear stress for the 2D blood vessel model with stenosis 60% under laminar flow is bigger than the maximum shear stress for the 2D blood vessel model with stenosis 60% under turbulent flow.

ACKNOWLEDGEMENTS

The work was realized as a part of fundamental research no. 16.16.110.663 financed by the AGH University of Science and Technology.

REFERENCES

- [1] Stegehuis V.E., Wijntjens G.W.M., Murai T., Piek J.J., van de Hoef T.P. Assessing the haemodynamic impact of coronary artery stenoses: intracoronary flow versus pressure measurements. *European Cardiology Review*, 2018, 13, pp. 46–53.
- [2] Maussumbekova S., Beketaeva A. Application of immersed boundary method in modelling of thrombosis in the blood flow. In: *Proceedings of the 8th International Conference on Computational and Information Technologies in Science, Engineering and Education*, 24–27 September 2015, Almaty, Kazakhstan, Springer, 2015, pp. 108–116.
- [3] Bodnar T., Sequeira A. Numerical simulation of the coagulation dynamics of blood. *Computational and Mathematical Methods in Medicine*, 2008, 9, pp. 83–104. DOI: 10.1080/17486700701852784.
- [4] Xu Z., Chen N., Kamocka M., Rosen E., Alber M. A multiscale model of thrombus development. *Journal of the Royal Society Interface*, 2008, 5, pp. 705–722. DOI: 10.1098/rsif.2007.1202.
- [5] Wufsus A.R., Macera N.E., Neeves K.B. The hydraulic permeability of blood clots as a function of fibrin and platelet density. *Biophysical Journal*, 2013, 104, pp. 1812–1823. DOI: 10.1016/j.bpj.2013.02.055.
- [6] Govindarajan V., Rakesh V., Reifman J., Mitrophanov A.Y. Computational study of thrombus formation and clotting factor effects under venous flow conditions. *Biophysical Journal*, 2016, 108, pp. 1869–1885. DOI: 10.1016/j.bpj.2016.03.010.
- [7] Bouchnita A., Galochkina T., Kurbatova P., Nony P., Volpert V. Conditions of microvessel occlusion for blood coagulation in flow. *International Journal for Numerical Methods in Biomedical Engineering*, 2017, 33, pp. 1–15. DOI: 10.1002/cnm.2850.
- [8] Lin K.-Y., Shih T.-C., Chou S.-H., Chen Z.-Y., Hsu C.-H., Ho C.-Y. Computational fluid dynamics with application of different theoretical flow models for the evaluation of coronary artery stenosis on CT angiography: comparison with invasive fractional flow reserve. *Biomedical Physics and Engineering Express*, 2016, 2, 065011. DOI: 10.1088/2057-1976/2/6/065011.
- [9] Feng R., Xenos M., Girdhar M., Kang W., Davenport J.W., Deng Y., Bluestein D. Viscous flow simulation in a stenosis model using discrete particle dynamics: a comparison between DPD and CFD. *Biomechanics and Modeling in Mechanobiology*, 2012, 11, pp. 119–129. DOI: 10.1007/s10237-011-0297-z.
- [10] Guerciotti B., Vergara C. Computational comparison between newtonian and non-newtonian blood rheologies in stenotic vessels. In: *Wriggers P., Lenarz T., editors. Biomedical Technology*. Springer, 2018, pp. 169–183. DOI: 10.1007/978-3-319-59548-1.
- [11] Walburn F.J., Schneck D.J. A constitutive equation for whole human blood. *Biorheology*, 1976, 13, pp. 201–210.

- [12] Rosentrater K.A., Flores R.A. Physical and rheological properties of slaughterhouse swine blood and blood components. *Transactions of the American Society Agricultural Engineers*, 1997, 40, pp. 683–689.
- [13] Lu Q., Bryan V.H., Koo G., Malinauskas R.A. In vitro shear stress-induced platelet activation: sensitivity of human and bovine blood. *Artificial Organs*, 2013, 37, pp. 894–903. DOI: 10.1111/aor.12099.
- [14] Russo F., Basse N.T. Scaling of turbulence intensity for low-speed flow in smooth pipes. *Flow Measurement and Instrumentation*, 2016, 52, pp. 101–114. DOI: 10.1016/j.flowmeasinst.2016.09.012.
- [15] Launder B.E., Spalding D.B. The numerical computation of turbulent flows. *Computer Methods in Applied Mechanics and Engineering*, 1974, 3, pp. 269–289.
- [16] Solzbach U., Wollschlager H., Zeiher A., Just H. Effect of stenotic geometry on flow behaviour across stenotic models. *Medical and Biological Engineering and Computing*, 1987, 25, pp. 543–550.

Henryk Wachta*, Michał Wroński*, Katarzyna Józwiak*, Gracjan Kudra*

FLOODLIGHT SIMULATION OF REAL ARCHITECTONIC OBJECT USING 3D MODEL

Abstract

Presented materials discuss simulating light distribution using geometric model and open source 3D graphics package – Blender 3D. Research was based on floodlighting of Lubomirski Palace located in Rzeszów – an interesting object due to a lot of details and ornaments on the elevation. 3D model comprising all those distinctive features was created first, including all the reflective and absorptive materials and textures found on the outside walls of the palace. Research concluded on site allowed for precise location of floodlights in the model, based on existing handles prepared for lighting installation around the palace. Using blueprints for the real lighting installation and floodlights models in IES standard realistic lighting conditions were created. From many possible placement and intensity configurations most aesthetically pleasing was chosen for in-depth explanation and analysis. Different lighting phenomena was also modeled and analyzed during research, such as mirror reflections, Lambert reflections, inverse-square law and methods of digital recording of photometric solids. Presented work describes in detail such elements of the simulation as 3D mesh structure, texture parameters and numeric calculations of luminance distributions on lighted surfaces. Additional research result is a suggestion of lighting for the palace which aims to emphasize architectural values of the object at night time. Whether this suggestion will match features of real installation planned for the palace remains to be seen after its assembly.

Keywords

3D modeling, floodlight, light distribution, IES format

1. INTRODUCTION

Illumination is an effect of efforts, that exhibit an object and its details using artificial lighting to make it look more attractive at nighttime [1, 2]. Its main purpose is to strengthen the perception of spatial characteristics of the geometry, to accent particularly interesting

* Rzeszów University of Technology, Faculty of Electrical and Computer Engineering, Rzeszów, Poland;
corresponding author: kasiaj963@wp.pl

architectonic details, and to emphasize individual characteristics of the object in question, arising from its style and history [3]. The art of illumination focuses less on photometric parameters of materials used. None the less it's worth noting that the luminance distribution over the elevation of an object is important parameter, almost always taken into account [4]. Analysis of this parameters helps to avoid two opposing, negative situations: too bright illumination in contrast to dark night sky and too faint lighting over the elevation, especially in highly urbanized areas with many road lights [5].

Modern polygonal methods of illumination design, based on tests on the site are used only where floodlighting using few light sources is planned. More complex illumination installations, utilizing zone or mixed scenarios are designed using computer aided methods [6, 7].



Fig. 1. Modern illumination of Rzeszów City Hall (photograph taken as a part of the activity of the Scientific Society of the Electrical Power Engineering. Available from: <https://drive.google.com/drive/folders/1DkAxv0kzckVqUd2ZnpN5FlpmRcGEO3xo?usp=sharing> [accessed: 2018.07.04])

Computer design of illuminations creates many challenges. Firstly, detailed and accurate geometric model of elevations is required. Parts of the objects, which are excluded from illumination, can be projected with fewer details. Some parts may fall into that category, and thus fainter lighted because of dense vegetation coverage or poor visibility [6, 7].

In the next step, all external lighting phenomena influencing the object in question should be taken into account, i.e. immission impact of road or park lights. Also reflection parameters of materials used in computer design should be selected carefully. Lastly, light ray distribution of the lighting fixtures used in illumination should be modeled as accurately as possible. Procedure of digitalization of partial light rays of analyzed light-optical system with the help of goniometer proves to be very useful here. As a result illumination designer can work with

files describing exact way of light distribution by the lighting fixtures that have standardized structure described in IES standard [6].

Classic example of illumination usage to highlight attractiveness of a city center is Town Hall in Rzeszów (Fig. 1) The building is situated in central zone of a town square, in a historic center of Rzeszów. It was built in late XVI century. First renovation and modification was performed at the beginning of XVII century, and its present state is a result of XIX century modernization. It composes elements of Neo-Gothic and Neo-Renaissance styles. Rzeszów City Office functions in the building at present [8].

2. HISTORICAL AND ARCHITECTONICAL QUALITIES OF LUBOMIRSKI PALACE IN RZESZÓW

Lubomirski Palace in Rzeszów was chosen to perform research presented in the paper. It is one of most valuable monuments in Rzeszów. Baroque building was constructed in late XVII century close to Lubomirski Castle. The Palace was a summer residence hidden in vast gardens with Chinese arbors, ponds and a vineyard. After a fire in the first decades of XX century the whole building was rebuilt [9].

At present the Palace undergoes thorough renovation and revitalization of its exterior, which makes great opportunity for creating illumination proposal for this object. It has really simple illumination system, which unfortunately is out of order for some time. In addition, the Palace is located in close proximity to multimedia fountain, which is very popular spot for tourists [9].

The Palace itself is a storey building with few symmetry planes: windows, decorations, cornices, that made the modeling process quite easy (Fig. 2). During the modeling phase the details projection scale was constantly verified to avoid overextension of geometric mesh. This approach was justified, because some elevation details are not clearly visible given the viewing distance.



Fig. 2. Modern exterior of Lubomirski Palace (photograph taken as a part of the activity of the Scientific Society of the Electrical Power Engineering. Available from: <https://drive.google.com/drive/folders/1DkAxv0kzckVqUd2ZnpN5FipmRcGEO3xo?usp=sharing> [accessed: 2018.07.04])

Main entrance to the Palace is situated in the central part of the eastern elevation. Upper part of the doorway is shaped as an arc, with additional small window above it. Whole area is complemented with detailed ornamentation. Similar entrance is situated at the opposing side of the building – facing the garden, also complemented with a lot of ornaments. The Palace viewed from above forms the shape of letter H, which makes the corner elevations stand out the most. The corner elevations contain double windows and Lubomirski family members' sculptures. All the dark, decorative frames were made of oak wood. First level windows are rectangular, and the ones above are square. Side walls are divided with pillars into three areas, with decorative carvings in central areas. Roof foundation resides on attractive cornice. Just preliminary evaluation of the building and its decorations classifies it as an attractive site for illumination.

3. GEOMETRIC PROJECTION OF THE REAL OBJECT

3D modeling is a process of creating or modifying objects to project real geometric parameters of real object into appropriate software. Creating complete 3D mesh can be long and complicated, and often require deep knowledge of specialized tools, especially when it comes to objects' details.

Geometric model size and proportions should correspond to real object. To accomplish such feat accurate photographic documentation should be prepared beforehand. Photos should be taken from different angles and distances, especially parallel and perpendicular to outline of the object. To accurately document objects' proportions, photos taken from far away are required, as far as it is possible. In turn close-ups can help when modeling ornaments and details.

Common practice is to use prepared documentation as a background during modeling process. It shortens the time required to build the model, allowing to keep track of measurements and main proportions at the same time. Both levels of the building were created using this technique – one level at a time, including roof. The last stage was creation of the details and ornaments.

As mentioned before, it is very important to assume how detailed should the final mesh be before creating it. It will help to achieve required visual accuracy with least possible effort.

Because of the shadow play on the elevation it is important to project more precisely all the parts of the elevation that will be actively lighted and thus will cast shadows.

Making the models too simple in those cases could lead to big differences between lighting simulation in virtual environment and real objects. Considering all the problems and techniques described above, geometric model of the Palace was created. Example projections of the elevations are presented on Figures 3 and 4. Unfortunately, those virtual walls exhibit infinitely flat surfaces, which is not the case in real scenarios.

In real world cases, due to flaws in plastering, the walls are not perfectly even. This fact can result in non-attractive illumination, especially when the lights are close to elevation. Only way to determine if this problem will occur is to perform field test with a light source on site, to evaluate how well the plastering was done. If this is the case where the plastering is not even, the assumptions shift may be required – the lighting equipment should be positioned further away from the walls.

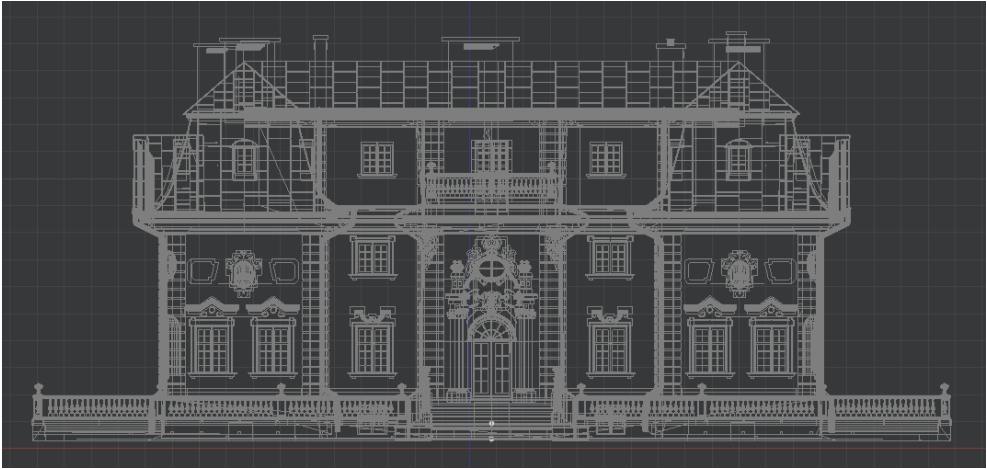


Fig. 3. Wireframe view of the mesh – west elevation

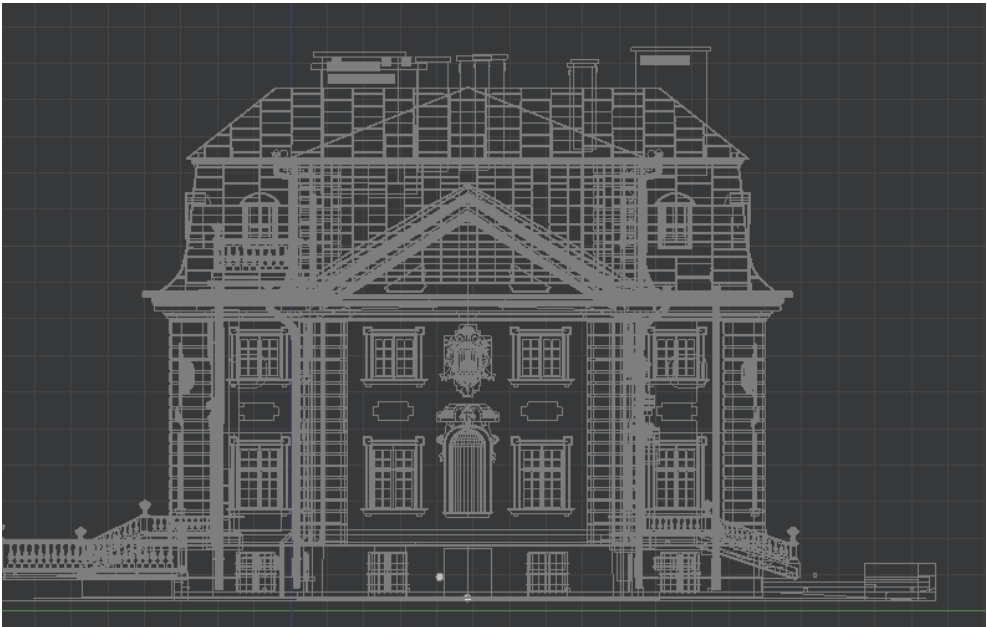


Fig. 4. Geometric mesh of the side elevation

Projections from Figures 3 and 4 don't allow viewing the level of details of the model created. It can be evaluated with the detailed illustrations of ornaments and small architectonic elements in greater zoom. They often use basic geometric forms, i.e. cylinders, cones, cups etc. This type of objects must be modeled by approximating arcs with short straight lines. Given typical viewing distances, this technique can be used without negative visual effects, resulting in simpler 3D mesh (Fig. 5).

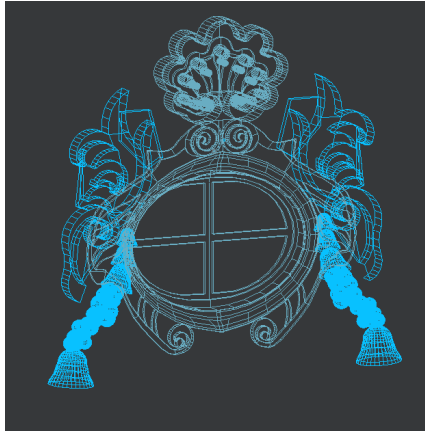


Fig. 5. Part of a window model with decorations

Oval heraldic plaque of the Lubomirski family (Fig. 6), situated below the window depicted in Figure 5 was modeled with many details – L shaped initial is clearly visible, as well as many spiral ornamentations.

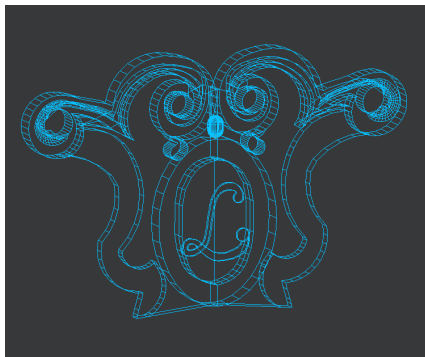


Fig. 6. Geometric mesh of the heraldic plaque

4. MODELING OF THE BASIC ELEVATION MATERIALS

Applying textures to 3D mesh is a process, which allows to project number of properties associated with lighting, i.e.: roughness, color, absorption and reflection of light rays [6]. Those parameters are closely related to luminance of illuminated surfaces. Detailed photographs of all main materials covering the Palace were taken during the research: plasters, metal plates covered in patina, wooden ornaments. After required modifications those photographs were used to prepare appropriate textures that were then applied to the model. Using only material built in the modeling software was not sufficient, so external images from the photographs were needed. This step was important to reduce sterile impression of initial, basic renders.

Care was also taken to reduce negative texturing effects associated with emergence of repeating patterns from materials used.

Along with esthetic quality of textures, photometric parameters are equally important. To precisely determine the values of reflection parameters for each material, series of measurements using luminance meter LS-110 [10]. Reflection parameters were computed from comparison of incoming and reflected light levels over every material analyzed (Fig. 7).



Fig. 7. Light reflection parameter measurement points and its results

Table 1 contains detailed information about all the results obtained.

Table 1. Material comparison in regards to incoming and reflected light levels

Material	Incoming light level [lx]	Reflected light level [lx]
Railings	669	436
Walls	553	262
Columns	633	471
Railing foundations	600	263
Rooftop	1037	395

Additional work was required to prepare those materials, that were covered in dirt or stains in non-uniform way, i.e.: rooftop or parts of the elevation close to the ground. To create accurate visual representation of those areas photos of elements in question were altered using computer graphic tools. Resulting images were base to procedurally re-create appropriate materials inside modeling software. Using carefully picked parameters for the scales and amplitudes of noise mixed into those textures effects of randomly placed stains, rust and patina

were achieved. Those, combined with color data from real elevation materials of the Palace, allowed for high degree of realism in renders, as depicted on Figure 8.



Fig. 8. Rooftop with stains and patina

Beside reflection parameters of the elevation and rooftop materials, qualitative parameters of reflections were also analyzed. Rough materials (plasters) exhibit Lambert's reflections. It is the most wanted scenario from illumination standpoint – regardless of viewer or light position, the material in the light will be seen as illuminated. Those materials account for majority of cases with the Palace. Second group of materials are those, that are less rough i.e.: painted elements of decorations. Light bouncing off such material will create scattered rays with scattering scale arising from a parametric curve, different for every case (Fig. 9) [1, 2].

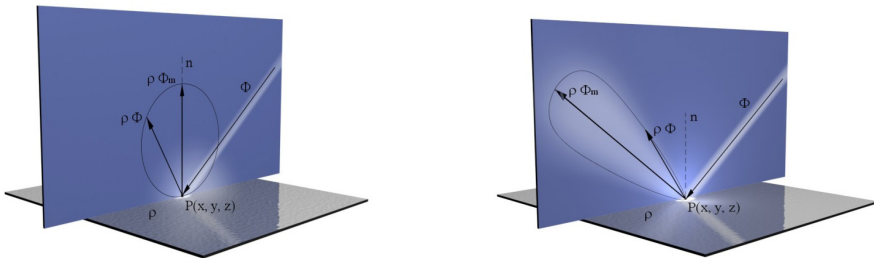


Fig. 9. Illustration of Lambert's reflection and directionally scattered one

Materials that reflect light in directionally scattered way are only a few when it comes to the Palace. Third and final group are the materials used to simulate window glass. Those simulate mostly mirror-like reflections, so they do not account into creating illuminations. Final model of the Palace consists of the geometric mesh and material coverage, as depicted on Figures 10 and 11.



Fig. 10. Day time visualization of the Palace – eastern elevation.

Precise computer models of those two elements were vitally important in the third, final phase of the whole process: designing the illumination. In addition to both elements of the Palace itself, some parts of the environment around the object were modeled as well, i.e.: railings, stairs, fences, etc.



Fig. 11. Day time visualization of the Palace – western elevation

Modeling those environmental features of the ground surrounding the Palace allowed evaluating possible positioning of lighting equipment. Rendering images presented in Figures 10 and 11

allowed to decide that the model is accurate enough for simulating illumination, due to high level of detail and visual similarities to the real object. The model itself could be also used for other design projects associated with the Palace.

5. PALACE ILLUMINATION PROPOSAL

Before the proposal could be created, measurements of the night sky luminance were concluded on site. Recommendations of the International Lighting Committee tie average luminance level of illuminated elevation to average sky luminance during the night [11]. In addition to measurements of sky luminance, the impact of nearby road and city lights was measured and evaluated as an unintended light source for illumination purposes [5].

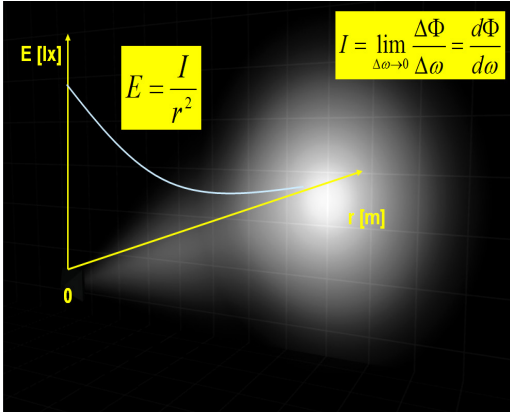


Fig. 12. Illustration of the inverse squared distance law

Light spots generated by external lights were taken into account when designing the illumination proposal. Measurements of those spots were concluded using LS-110 [10] luminance meter. Also positions of external lights were measured. Using this data and the law of inverse squared distance (Fig. 12), mechanisms for realistic external light impact simulations were introduced into modeling software. It is worth mentioning that many programs used in 3D modeling don't provide computational methods of ray tracing that would take into account how light is absorbed with distance or provides only linear methods. If this is the case, resulting simulation can lead to false results, making quantitative evaluation of the illumination highly biased.

Most important phase of illumination design is obtaining accurate shapes of photometric curves for each lighting fixture used. Many applications aren't suited well for reading and using files that describe precise way of distributing light from a given fixture (as described in IES standard files). Using such data allows using only those fixtures that will meet all the designers' requirements. The IES standard ties all basic directional properties of a given fixture with dimensional angles of light radiation in standardized C-gamma reference system (Fig. 13).

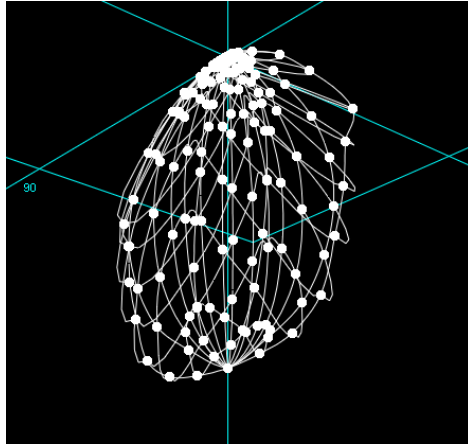


Fig. 13. Visualization of an example lighting fixture using IES description and reference system

During design phase, appropriate lighting fixtures were chosen from all the hardware available at present and the corresponding IES files for each fixture were loaded to the modeling software. During many simulations and computations different illumination scenarios were evaluated [12]. Finally, most beneficial configuration of the fixtures positioning and aiming was chosen. The proposal project contains a reverse type of illumination to the sun shining during the day, where the shadows are opposite to the arrangement of natural shadows. Therefore selected architectural details are expressed. Figures 14 and 15 depict positions and targets of the fixtures used in the proposal.



Fig. 14. Authors' proposal of positioning and targeting of the lighting fixtures on the western elevation of Lubomirski Palace

Each arrow marks single fixture – with its positioning at the beginning of the arrow and target at the end. It’s easier this way to evaluate the whole project on site. In addition it allows evaluating all the fixtures locations by appropriate custodian services as well as in regard to other systems locations on site (plumbing, electrical and gas systems).

Western elevation was lighted using seventeen fixtures to achieve possibly similar luminance over the entire side. Those light sources have light temperature of 3500 K, which matches the plaster coloring over the wall. Rooftop, covered in patina, was lighted using 5000 K light sources. High contrasts between elements of the elevation (i.e.: light plastering and dark window decorations) forced to use light sources with very good color transfer properties.

Different light source parameters available in the modeling software with usage of the IES standard files and the “down to up” type of illumination allowed for accent lighting of the columns (which in turn strengthened the overall impression of illumination). It also allowed for concentration of light rays on the actual object surface, eliminating negative immissive effects. Using precise light emission curves from IES files for the given fixtures allowed to create attractive night time view of the Palace, with regard to all recommendations from the literature of the subject (intensifying objects coherence, ordering principle and others) [5, 13].



Fig. 15. Authors’ proposal of positioning and targeting of the lighting fixtures on the northern elevation of Lubomirski Palace

6. COMPUTER SIMULATION RESULTS

The final phase of design was to create two views of the Palace – one aiming to maximal realism, the other depicting distribution of luminance over the elevation. Figure 16 was created using light tracing computations in modeling software and should be used as a visual guideline to evaluate the overall illumination effect.

Such visualization can be used as a base for extended discussion over the illumination method used (floodlighting, zonal or mixed), fixtures conservation in the future, shadow casting over the elevation by elements of the environment (mostly vegetation) and sometimes the effect of light radiation inside the object.



Fig. 16. Computer simulated view of Lubomirski Palace

Along with realistic render, design phase should be concluded with luminance distribution image over the elevation [4]. Without such results it would be impossible to evaluate the quality of illumination application over the real object. Figure 17 depicts the luminance distribution in false color render.

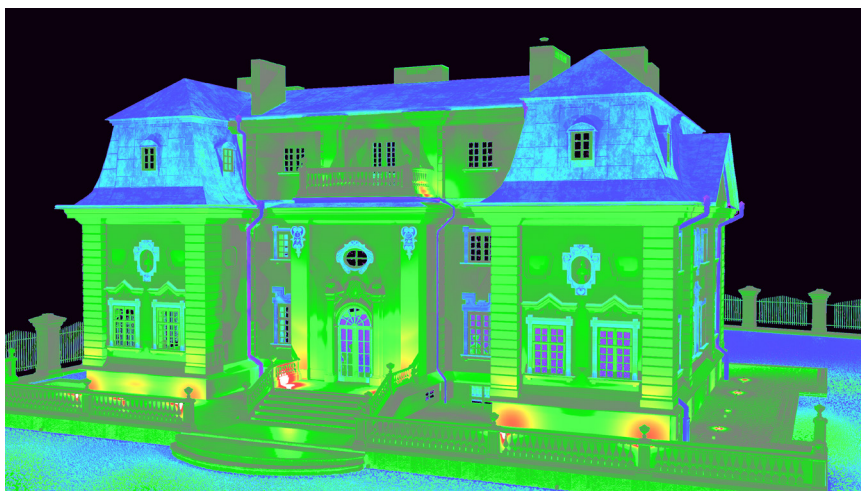


Fig. 17. Luminance distribution over the elevation

False color luminance distribution allows for quantitative evaluation of illumination properties: the relationship between elevation and sky luminance, zones of over burning (local light spots of increased intensity, especially close to ground fixtures' positions), realization of depth and height perception strengthening principles and others. These quantitative properties allow evaluating how well the proposal could perform on the site, opening the possibility of project realization.

7. CONCLUSION

Lubomirski Palace illumination, proposed in the paper confirms how valuable the IES standard is and its associated photometric curves when it comes to modeling decorative lighting. Fixtures with different distribution characteristics were used – from narrow (used as accenting ones) to wide. Design was performed for real architectonic object, using highly accurate 3D model created for the study. Work methodology involved using advanced graphical software that allowed modeling all physical phenomena important from illumination standpoint. Using the right hardware setup and software applications allows creating advanced illumination scenarios that can be then utilized to create lighting projects in practice.

REFERENCES

- [1] Żagan W., Krupiński R. Teoria i praktyka iluminacji obiektów. Oficyna Wydawnicza Politechniki Warszawskiej, Warszawa 2016.
- [2] Żagan W. Iluminacja obiektów. Oficyna Wydawnicza Politechniki Warszawskiej, Warszawa 2003.
- [3] Malska W., Wachta H., Panek A. Iluminacja Pałacu Tyszkiewiczów w Weryni. Zeszyty Naukowe Politechniki Rzeszowskiej, 2013, z. 33, pp. 171–180.
- [4] Słomiński S. Prawidłowa rejestracja obrazu obiektu iluminowanego – problemy wynikające z możliwości oprogramowania i ograniczeń sprzętu. Przegląd Elektrotechniczny, 2013, 89, pp. 259–261.
- [5] Pollard N.E. Guide on the limitation of effects of obtrusive light from outdoor installations. CIE International Commission on Illumination. Vienna 2003.
- [6] Krupiński R. Modelowanie 3D dla potrzeb iluminacji obiektów. Oficyna Wydawnicza Politechniki Warszawskiej, Warszawa 2011.
- [7] Krupiński R. Visualization as Alternative to Tests on Lighting under Real Conditions. Light and Engineering, 2015, 23, 4, pp. 22–29.
- [8] Description of Town Hall [on-line]. Available from: <http://www.rzeszow.pl/miasto-rzeszow/historia/zabytki-rzeszowa/ratusz> [accessed: 2018.07.04].
- [9] Description of Lubomirski Palace [on-line]. Available from: <http://www.rzeszow.pl/miasto-rzeszow/historia/zabytki-rzeszowa/palac-letni-lubomirskich> [accessed: 2018.07.04].
- [10] Description of Luminance Meter [on-line]. Available from: <https://www.konicaminolta.eu/pl/urzedzenia-pomiarowe/produkty/pomiary-swiatla-i-ekranow/produkty-wycofane/ls-100-ls-110.html> [accessed: 2018.07.04].
- [11] CIE Technical Report No 94 – Guide for Floodlighting.

- [12] Leśko M., Baran K., Wachta H. Wielowariantowa iluminacja Pałacu Lubomirskich w Rzeszowie. *Czasopismo Inżynierii Łądowej, Środowiska i Architektury*, 2017, z. 64, pp. 49–56.
- [13] Wachta H. Wskazania potrzeby aktualizacji zaleceń obejmujących zagadnienia oświetlenia iluminacyjnego. *Przegląd Elektrotechniczny*, 2007, 2, pp. 75–81.

Łukasz Magda*, Katarzyna Wilkosz*, Władysław W. Kubiak*

APPLICATION OF GLASSY CARBON ELECTRODE MODIFIED BY PEDOT-TiO₂ COMPOSITE IN METOL DETECTION

Abstract

Titanium dioxide due to its good electrical properties and high photocatalytic activity is commonly used in many branches of knowledge. In this work application of titanium oxide nanoparticles has shown in modification of glassy carbon (GC) electrodes often used as a working electrode in voltammetry. This analytical technique is based on the measurement depending on the current – electric potential in a working and reference electrode immersed in supporting electrolyte with determined analyte. The GC electrode was modified by conductive layer composed of conducting polymer (PEDOT) and titanium dioxide nanoparticles using electropolymerization method. Before electropolymerization process GC electrode was polished on the polishing cloth with alumina nanopowder and washed by deionized water and the solution of PEDOT and TiO₂ nanoparticles was mixed by magnetic stirrer. Preliminary measurements suggest that modification based on PEDOT-TiO₂ composite affects the quality of the analytical signal of determined substance. This modification increased the sensitivity of the GC electrode due to metol.

Keywords

voltammetry, metol, electrode, nanopowder

1. INTRODUCTION

Choosing the right working electrode is a key step in voltammetric studies. For many years, the most frequently used electrodes due to their high sensitivity and very good reproducibility were a mercury droplet electrode (CHMDE, SMDE, CGMDE) and a mercury film electrode (MFE). However, due to the toxicity of mercury, alternative electrode materials are now being sought with equally good metrological parameters that could replace the traditional mercury electrodes [1]. One of the many possible solutions is the use of glassy carbon electrodes (GCE)

* AGH University of Science and Technology, Faculty of Materials Science and Ceramics, Krakow, Poland;
corresponding author: katwilkosz@gmail.com

or carbon-paste electrodes (CPE) that were initially used only in the positive potential range, because mercury electrodes were not the best solution in this area [2]. However, solid electrodes require a very thorough surface polishing, because this operation significantly affects the repeatability and reproducibility of measurements. In addition, solid electrodes are characterized by slightly worse metrological parameters in relation to mercury electrodes. Hence there is need to modify solid electrodes in order to improve the analytical parameters of the method in which these electrodes are used [3]. Therefore, the purpose of this study was to modify glassy carbon electrodes with composite PEDOT-TiO₂. This composite contains a conducting polymer called poly(3,4-ethylene-1,4-dioxythiophene) – PEDOT and nanometric titanium(IV) oxide with different grain sizes (P90 – 14 nm, P25 – 21 nm, rutile – 1–3 nm, anatase 4–8 nm). These modified glassy carbon electrodes were applied in p-methylaminophenol sulphate detection.

P-methylaminophenol sulphate (metol) is a compound largely used in photographic industry as a reducing agent. Unfortunately, metol also has been shown to be toxic and cause health problems [4]. Therefore, the development of sensitive methods for the detection of metol is very necessary. Until now, various method such as spectrophotometry, oscillopolarographic titration, liquid chromatography–mass spectrometry, ceric oxidimetry, and electroanalysis have been developed for determine metol. Among them, the electrochemical methods offer simplicity, selectivity, and rapid response with a long linear dynamic range [5].

1.1. VOLTAMMETRY

Voltammetry is a method belonging to a group of electroanalytical methods whose operation is conditioned by the flow of current during the course of electrode reactions. Voltammetric measurements are based on the relationship between the current intensity and the potential of the working electrode [6]. In the field of voltammetry, the appropriate choice of measurement conditions is critical. The working electrode should be polarizable and should have a relatively small surface area. The use of small areas allows for obtaining low values of measured currents, as well as consuming minimal amounts of the analyte in the electrode reaction, so that even if several measurements are carried out, any noticeable changes in concentrations are observed. The reference electrode should be a non-polarized electrode and should be reversible. In contrast to the working electrode, the reference electrode should have a large surface area so that the flow of current in the measurement system does not affect its potential. In addition, a potentiostat and an auxiliary electrode are often used, most often a platinum wire, in order to prevent polarization of the reference electrode. In addition to the above-mentioned elements included in the three-electrode measurement system, it is very important to select the supporting electrolyte that provides sufficient conductivity and eliminates the migration current [7].

The most commonly used working electrodes are various types of mercury electrodes and fixed electrodes. Among electrode mercury electrodes are distinguished with controlled droplet increment (CGMDE), hanging drop electrodes (HDME) and electrodes made of gold, silver or glassy carbon with a thin layer of mercury not exceeding 100 μm (MFE). Mercury electrodes, despite having very good metrological parameters, also have several disadvantages. The main disadvantage of these electrodes is the use of mercury, which is toxic to both the environment and living organisms. In addition, mercury electrodes are not suitable for use

in the range of higher, positive potentials, because after exceeding the potential of 400 mV mercury dissolves. The possibilities of modifying mercury electrodes are also limited. For the above reasons, solid electrodes made of precious metals (Pt, Au, Ag) and carbon-based materials are used. The most popular coal material is glassy carbon (GC). All solid electrodes are relatively easy to modify allowing new functionality to be obtained or to improve their metrological and analytical parameters [8].

1.2. CONDUCTING POLYMERS

Conducting polymers were discovered accidentally by Hideki Shirakawa in the seventies of the twentieth century, during the development of a new method of polyacetylene synthesis. Shirakawa used by mistake a thousand times more catalyst, so in the reaction vessel instead of the black powder appeared a coating with a metallic gloss, showing conductive properties. Hideki Shirakawa, Alan G. MacDiarmida and Alan J. Heeger in 2000 received the Nobel Prize for working on polyacetylene and conducting polymers. The classification of conducting polymers is most often performed due to the conduction mechanism, which is why today stands out: electronically conducting (conjugated) polymers, ion-conducting polymers (polyelectrolytes) and conducting polymers with charge transfer. Conjugated polymers, otherwise referred to as “main chain” conducting polymers, are polymers that exhibit conductivity due to the occurring conjugate double bond systems or the overlap of empty d-orbitals along the main chain. The group of conjugated polymers includes, among others: polyaniline, polyacetylene, polythiophene, polypyrrole and their derivatives. The conductive mechanism of ion-conducting polymers consists in the stepwise movement of the cation between the electron-donor groups, which also causes the anion to move in the opposite direction. An example of polyelectrolyte is nafion. Conductive polymers through a complexing mechanism with load transfer they are polymers having side groups with the structure of complexes capable of carrying the load. An example of this kind of polymer is polyvinyl-ferrocene [9].

1.3. TITANIUM DIOXIDE

Currently, materials with nanometric dimensions are very popular in material and experimental sciences due to their interesting physical and chemical properties. Nanomaterials are characterized by a high surface to volume ratio, which makes them used for the production of highly ductile ceramics and for the production of membranes with high porosity and electrodes [10].

One of the most commonly used nanometric materials is titanium(IV) oxide. Titanium dioxide is an odorless, white and non-reactive powder. Due to its photocatalytic properties, it is most often used for the production of photocatalysts [11]. Nanometric titanium(IV) oxide is widely available, most often in commercial form designated as P25 (Evonik) and P90 (Evonik). These nanopowders differ from each other by grain size, surface area and ratio of rutile to anatase content (polymorphic forms of titanium(IV) oxide). TiO₂ nanoparticles (P25) have a specific surface area of 35–65 m²/g, a particle size of 21 nm and an anatase / rutile ratio content of 80:20. TiO₂ (P90) nanoparticles, in turn, have a specific surface area 20–90 m²/g, particle size of 14 nm and ratio of anatase to rutile content 88:12. Commercial forms of titanium(IV) oxide are obtained using high purity titanium(IV) chloride as a raw material. TiCl₄ is evaporated and

then mixed with air and hydrogen. The reaction of titanium(IV) chloride with gases is in the temperature at range 1000–2400°C [12]. Another commercially available titanium oxide(IV) is nanopowder with a grain size of 1–3 nm, its distributor on the Polish market is 3D Nano. Unlike P90 and P25, this type of titanium(IV) oxide consists of only one phase – rutile.

2. EXPERIMENTAL

Five different glassy carbon electrodes were tested. One electrode modified only by the conducting polymer – PEDOT and four electrodes modified by the composite PEDOT-TiO₂, where different kind of the titanium dioxide nanopowder were used (P90 – 14 nm, P25 – 21 nm, rutile – 1–3 nm, anatase 4–8 nm). Scanning electron microscopy (SEM) and energy-dispersive X-ray spectroscopy (EDS) research were done for the modifying layers of the GC electrodes modified by composite. Cyclic voltammetry measurement were carried out for the metal detection using all modified GC electrodes. Based on measurements of cyclic voltammetry, the calibration curve for metal and the curve of the current peak dependence on the polarization rate for all electrodes were determined.

All measurements were made using the M161 electrochemical analyzer (mtm anko, Poland). The tests used a three-electrode system with a silver-chloride electrode (filled with a 3M solution of potassium chloride) as a reference electrode and a platinum wire serving as an auxiliary electrode. As working electrodes, modified disk electrodes made of glassy carbon (Mineral, Poland) were used, using a composite consisting of conducting polymer Poly (3,4-ethylene-1,4-dioxythiophene) (PEDOT) and nanometric titanium dioxide.

3,4-Ethylene-1,4-dioxythiophene monomer (Sigma-Aldrich, Switzerland), titanium dioxide nanopowder (P25, P90, Evonik, Germany), rutile (1–3 nm, 3D Nano), anatase (4–8 nm, 3D Nano). Phosphate buffer solution with a pH of 7.5 and a concentration of 0.1M prepared from components with a purity of (POCh), 0.1M metal solution of P. p.a. (POCh). All the solutions used were prepared using aquastilled water.

On electrodes made of glassy carbon, a layer of a conducting polymer composite – ceramic nanopowder – was applied by electropolymerization technique. Various types of nanopowders of the titanium dioxide were used for the modification. The electrodes before applying the layers were polished on a polishing cloth made of Al₂O₃ with a particle size of 0.3 μm, and then rinsed under a stream of bidistilled water. Electrode modification was done by preparing a PEDOT solution and a suspension containing PEDOT and TiO₂ nanopowders, which was mixed for 24 hours immediately prior to their application using a magnetic stirrer.

A basic electrolyte solution consisting of 0.2 mL 0.1 M phosphate buffer and a pH value of 7.5 and 9.8 mL of distilled water was prepared. To determine the calibration curve, the cyclic voltammetry technique and the 0.1 M metal solution were used. Voltammograms were recorded in the potential range –200 mV to +300 mV at a scanning speed of 50 mV/s. Additionally, in order to determine the mechanism of the electrode reaction occurring on the surface of the tested fixed electrodes, voltammograms in a metal solution at a concentration of 0.15 mM were recorded, with different values of the scanning speed: 10, 20, 25, 50, 100, 200 mV/s. Each measurement was repeated three times.

3. DISCUSSION AND RESULTS

Glassy carbon electrodes have been modified using a PEDOT conducting polymer and a PEDOT-TiO₂ composite. The titanium(IV) oxide introduced had different grain sizes of 1–3 nm (rutile), 14 nm (P90) and 21 nm (P25) and 4–8 nm (anatase). In order to check the efficiency of applying layers on glassy carbon electrodes, measurements were made using scanning electron microscopy and energy-dispersive X-ray spectroscopy. EDS measurements were performed at the point where the titanium oxide grains were visible on the SEM photomicrographs.

The SEM images presented on Figures 1–4 show single agglomerates of titanium(IV) oxide embedded in the PEDOT conducting polymer structure. The EDS spectrum shows peaks derived from oxygen and titanium, which confirms the efficiency of the incorporation of titanium(IV) oxide (P25, P90, rutile 1–3 nm and anatase 4–8 nm) into the conducting polymer structure.

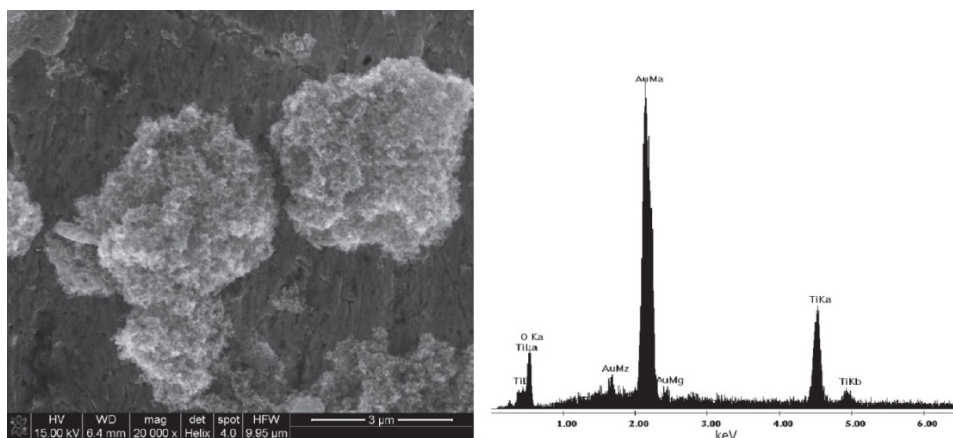


Fig. 1. SEM image and EDS spectrum for the PEDOT-TiO₂ composite (P25)

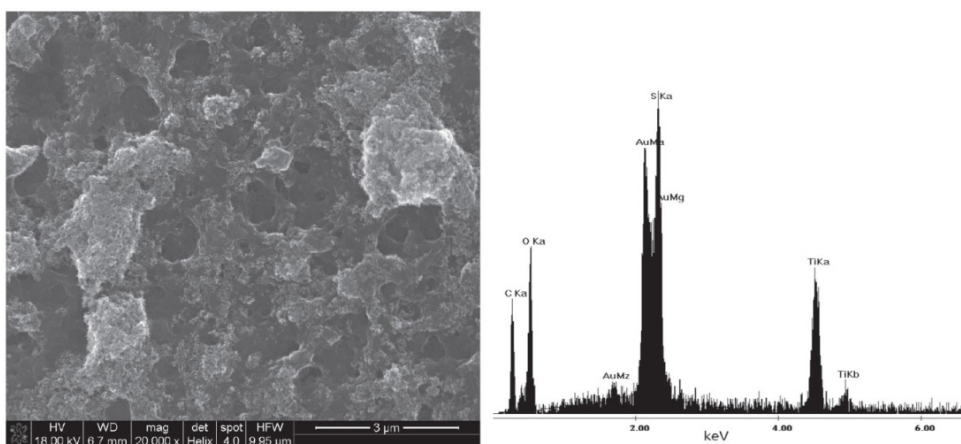


Fig. 2. SEM image and EDS spectrum for the PEDOT-TiO₂ composite (P90)

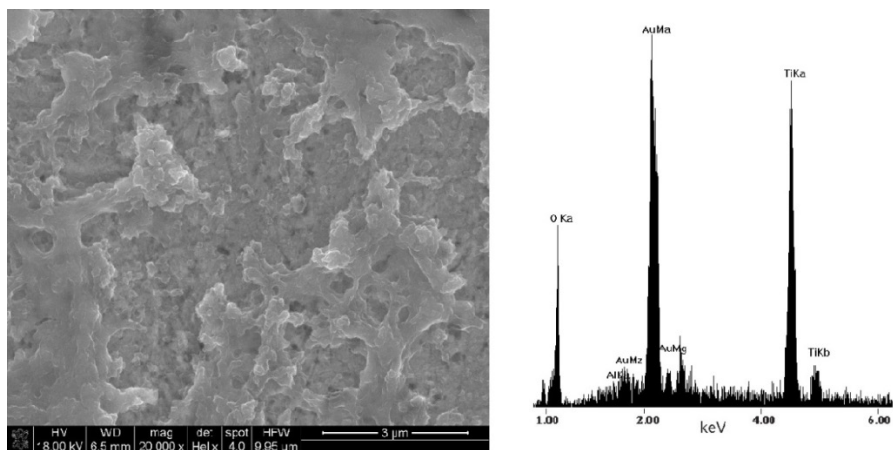


Fig. 3. SEM image and EDS spectrum for the PEDOT-TiO₂ composite (rutile 1–3 nm)

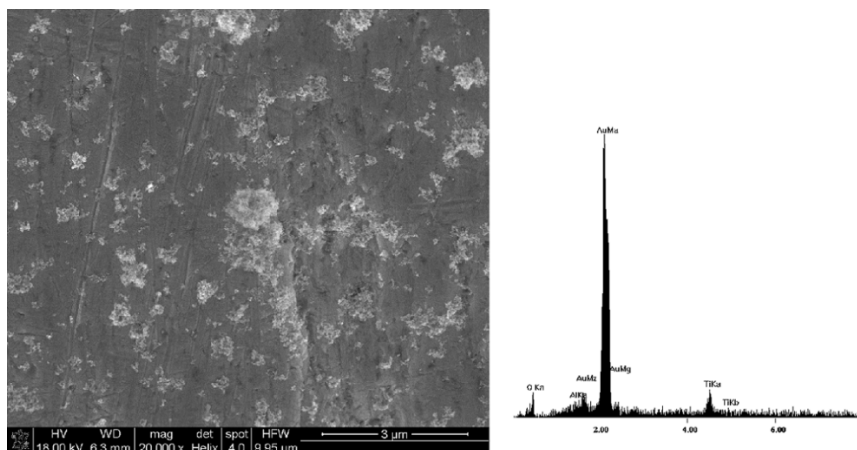


Fig. 4. SEM image and EDS spectrum for the PEDOT-TiO₂ composite (anatase 4–8 nm)

Analyzing the above images, it can be seen that, the smaller size of the titanium dioxide grains, the more difficult it is to separate single grains in the polymer structure. Due to the increase in the surface development of nanopowders, they begin to be incorporated into the structure of the conducting polymer in the form of associates.

In addition, on the spectrum of EDS originating from pure anatase, we can see a less intense peak coming from titanium. We can therefore infer that not only the size of the titanium dioxide grains but also the polymorphic form affects on the applied modifications. This is also confirmed by the EDS spectra for P25 and P90. Both of these nanopowders contain rutile and anatase phase, and the peak from titanium has a higher intensity than for nanopowder which contains only anatase phase.

The basis for the quantification is the calibration function, so it is possible to determine whether the modification has brought the intended effect. Two parameters are particularly

important: the slope defining the sensitivity of the method and the limit of quantification (LOQ). While the limit of detection (LOD) can be estimated based on the standard deviation of the blank, the limit of quantification should take into account the uncertainty of determining the parameters of the calibration function. Therefore, the error propagation method was used to determine it. Figure 5 shows the calibration relationships for the modifications used.

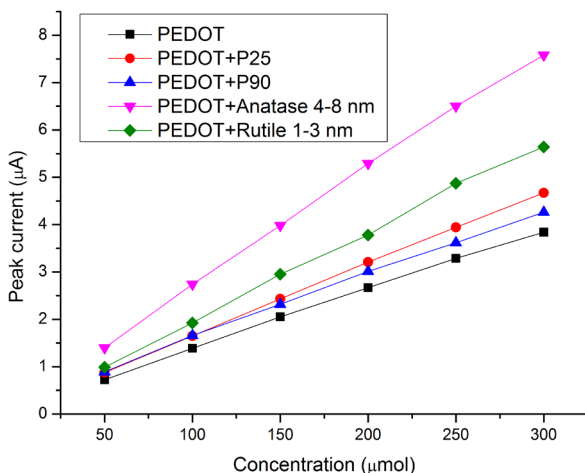


Fig. 5. Relationship between peak current values and analyte concentration (calibration curves) for the applied modifications

From the obtained graphs we can infer a linear dependence of the peak current gain along with the increase of analyte concentration. It is worth noting that all applied modifications with titanium dioxide are characterized by a higher slope of the obtained curve, which in proportion increases the sensitivity and metal determination. Table 1 summarizes the values of the limit of quantification and sensitivity for the applied modifications.

Table 1. Parameter summary for the applied modifications.

Applied modification	Sensitivity [$\mu\text{A}/\text{mM}$]	Detection limit [μM]
Pedot	12.5 ± 0.1	25.45
PEDOT + P25	13.4 ± 0.2	19.33
PEDOT + P90	15.2 ± 0.1	28.54
PEDOT + rutile (1–3 nm)	18.8 ± 0.2	32.04
PEDOT + anatase (4–8 nm)	24.9 ± 0.1	22.83

All the modifications applied have a better sensitivity and the quality of the analytical signal obtained on electrodes modified with titanium dioxide has significantly improved.

For the modifications obtained, a measurement of the dependence of the magnitude of the peak current on the element from the polarization rate was made as shown in Figure 6.

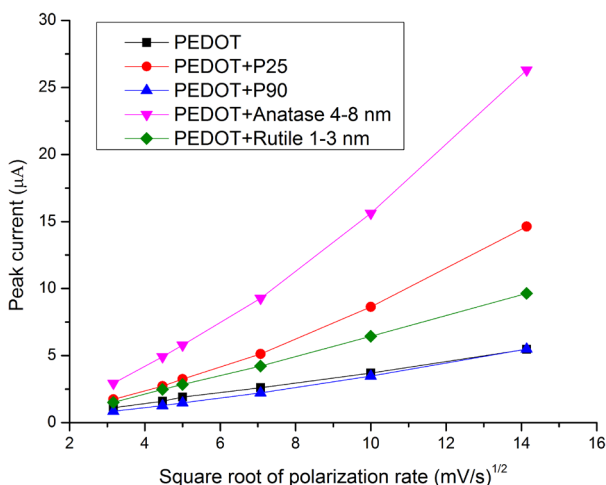


Fig. 6. The dependence of the peak current value on the element from the electrode polarization rate for the applied modifications

From the obtained graphs it can be seen that for electrodes modified using titanium dioxide we obtain exponential relations. This allows to conclude that the mechanism of electrode reaction for modified electrodes has a greater share of adsorption processes over diffusion processes. Additionally, we can conclude that the participation of various polymorphic titanium oxide variants will also have an effect on the mechanism of the electrode reaction.

4. SUMMARY

This paper presents the use of conductive polymer composite (PEDOT)-titanium(IV) oxide nanopowder (P25, P90, 1–3 nm rutile, 4–8 nm anatase) to improve performance parameters such as sensitivity or limit of quantification for a glassy carbon electrode modified with conductive polymer. It has been shown that the presence of titanium dioxide nanoparticles in the conductive polymer structure has a beneficial effect on the quality of the results obtained and improves the usable performance of the electrode compared to the modification using the conductive polymer alone. From the obtained results it can also be concluded that both the degree of fragmentation and the existing polymorphic forms of the nanomodifier will have an effect on the obtained results, which will undoubtedly be the subject of further considerations. The obtained results confirm a wide range of applications of ceramic powders, in this case also for modification of electrodes used in voltammetry. Characteristics of the surface of layers modifying the glassy carbon electrodes made by means of scanning electron microscopy SEM and EDS X-ray microanalysis confirmed the possibility of effective incorporation of titanium(IV) oxide into the structure of the PEDOT conducting polymer by electropolymerization.

ACKNOWLEDGEMENTS

This study was carried out within the AGH University of Science and Technology (Krakow) – grant no. 15.11.160.017

REFERENCES

- [1] Wang J., Lu J., Kirgöz U.A., Hocevar S.B., Ogorevc B. Insights into the anodic stripping voltammetric behavior of bismuth film electrodes. *Analytica Chimica Acta*, 2001, 434, pp. 29–34. DOI: 10.1016/S0003-2670(01)00818-2.
- [2] Galus Z. Mercury electrodes. In: Kissinger P.T., Heineman W.R., Dekker M., editors. *Laboratory Techniques in Electroanalytical Chemistry*. 2nd ed. Marcel Dekker Inc, New York 1996, pp. 443–466.
- [3] Dryhust G., McAlister D.L. Carbon Electrodes. In: Kissinger P.T., Heineman W.R., Dekker M., editors. *Laboratory Techniques in Electroanalytical Chemistry*. 1st ed. Marcel Dekker Inc, New York 1984, pp. 289–319.
- [4] Wei Sun, Ying Deng, Jun Liu, Weiming Liu, Yong Cheng, Lei Wang, Yuanxiang Gu. Electrochemical behavior and voltammetric determination of p-methylaminophenol sulfate using LiCoO₂ nanosphere modified electrode. *Thin Solid Films*, 2014, 564, pp. 379–383. DOI: 10.1016/j.tsf.2014.05.042.
- [5] Xueliang Niu, Lijun Yan, Zuorui Wen, Xiaobao Li, Yanyan Niu, Yaping Lu, Wei Sun. Voltammetric Determination of Metol on a Gold Nanoparticle Modified Carbon Molecular Wire Electrode. *Analytical Letters*, 2017, 50, 2, pp. 325–335. DOI: 10.1080/00032719.2016.1177536.
- [6] Galus Z. *Fundamentals of electrochemical analysis*. Ellis Horwood – PWN, Warszawa 1994.
- [7] Kubiak W.W., Gołaś J. *Instrumentalne metody analizy chemicznej*. Wydawnictwo Naukowe AKAPIT, Kraków 2005.
- [8] Wang J. *Electroanalytical technique in clinical chemistry and laboratory medicine*. VCH, New York 1998.
- [9] Inzelt G. *Conducting Polymers*. Springer Verlag, Heidelberg 2008.
- [10] Barbé Ch.J., Arendse F., Comte P., Jirousek M., Lenzmann F., Shklover V., Grätzel M. Nanocrystalline Titanium Oxide Electrodes for Photovoltaic Applications. *Journal of the American Ceramic Society*, 1997, 80, 12, pp. 3157–3171. DOI: 10.1111/j.1151-2916.1997.tb03245.x.
- [11] Wyrwa J., Rękas M. Fotokatalityczna degradacji błękitu metylenowego przy użyciu nanokrystalicznego TiO₂. *Materiały Ceramiczne/Ceramic Materials*, 2011, 63, 3, pp. 524–527.
- [12] AEROXIDE®, AERODISP® and AEROPERL® Titanium Dioxide as Photocatalyst, Technical Information 1234, EVONIK industries [on-line]. Available from: <https://www.aerosil.com/sites/lists/RE/DocumentsSI/TI-1243-Titanium-Dioxide-as-Photocatalyst-EN.pdf> [accessed: 2017.07.12].



ISBN 978-83-66364-10-3